Naval Research Laboratory
Washington, DC 20375-5320

NRL/7320/MR—2022/6

Velocity Assimilation with Improved Synthetic Ocean Profiles (ISOP2): Validation Test Report

ROBERT W. HELBER

SCOTT R. SMITH

GREGG A. JACOBS

CHARLIE N. BARRON

MATT CARRIER

MAX YAREMCHUK

CLARK ROWLEY

HANS NGODOCK

Ocean Dynamics and Prediction Branch
Ocean Sciences Division

BRENT BARTELS

Peraton, Inc.
Herndon, VA

IVO PASMANS

University of New Orleans
New Orleans, LA

CHRIS J. DEHAAN

Peraton, Inc.
Stennis Space Center, MS

October 4, 2022

REPORT DOCUMENTATION PAGE

Form Approved
OMB No. 0704-0188

1. REPORT DATE *(DD-MM-YYYY)*	**2. REPORT TYPE**	**3. DATES COVERED** *(From - To)*
04-10-2022	NRL Memorandum Report	

4. TITLE AND SUBTITLE

Velocity Assimilation with Improved Synthetic Ocean Profiles (ISOP2): Validation Test Report

5a. CONTRACT NUMBER

5b. GRANT NUMBER

5c. PROGRAM ELEMENT NUMBER

6. AUTHOR(S)

Robert W. Helber, Scott R. Smith, Gregg A. Jacobs, Charlie N. Barron, Matt J. Carrier, Max Yaremchuk, Brent P. Bartels, Clark D. Rowley, Hans E. Ngodock*, Ivo Pasmans**, and Chris J. DeHaan***

5d. PROJECT NUMBER

5e. TASK NUMBER

5f. WORK UNIT NUMBER
1M44

7. PERFORMING ORGANIZATION NAME(S) AND ADDRESS(ES)

Naval Research Laboratory
Ocean Sciences Division
Stennis Space Center, MS 39529

8. PERFORMING ORGANIZATION REPORT NUMBER

NRL/7320/MR--2022/6

9. SPONSORING / MONITORING AGENCY NAME(S) AND ADDRESS(ES)

DARPA Public Release Center (PRC)
675 N. Randolph Street, Room 03-182
Arlington, VA 22203-1714

10. SPONSOR / MONITOR'S ACRONYM(S)

DARPA

11. SPONSOR / MONITOR'S REPORT NUMBER(S)

12. DISTRIBUTION / AVAILABILITY STATEMENT

DISTRIBUTION STATEMENT A: Approved for public release; distribution is unlimited.

13. SUPPLEMENTARY NOTES

*Peraton, Inc., 12975 Worldgate Dr, Herndon, VA 20170; **University of New Orleans, 2000 Lakeshore Dr, New Orleans, LA 70148
***Peraton, Inc., 1103 Balch Blvd, Suite 218, Stennis Space Center, MS 39529

14. ABSTRACT

Numerical ocean circulation forecasts diverge from reality due to non-deterministic processes or chaos. Through the process of data assimilation, the Navy's operational ocean forecasting system routinely makes ocean forecast corrections utilizing temperature, salinity, and sea surface height anomaly observations. Velocity observations, however, are vector quantities that require different processing and are not presently used. To assimilate existing ocean velocity observations, which generally are depth limited in scope, vertical error covariances are needed to relate the velocity errors throughout the water column. In this report we show an approach that relies on an empirically derived vertical error covariance model to relate the errors between temperature and salinity. Geopotential height calculations transform temperature and salinity covariances of the Improved Synthetic Ocean Profile version 1 (ISOP1) system into corresponding geopotential covariances. Prior Navy vertical error covariances within the Navy Coupled Ocean Data Assimilation (NCODA) system provides information over only a short depth range. The new vertical error model allows for full depth error covariance required for assimilation of depth limited velocity observations, which are the bulk of available velocity data in the ocean. This report describes the methods and a prototype system for ocean velocity data assimilation incorporating the new geopotential covariances that upgrade the Improved Synthetic Ocean Profile system to version 2 (ISOP2). This new NOCDA/ISOP2 data assimilation methodology is employed in the Navy's Couple Ocean Atmosphere Modeling Prediction System (COAMPS) providing greater forecasting capability because the prior system is unable to utilize in situ ocean velocity observations. Here we show velocity data assimilation validation experiments for Gulf of Mexico simulations during extensive drifter deployments in the summer of 2012 and again in 2020. Results reveal substantial improvements in forecast accuracy due to velocity data assimilation. Eulerian velocities are more accurate in the forecasts and Lagrangian drifter separations, between simulated and actual drifters' trajectories, is reduced. A key advantage of the system is that velocity data are dynamically linked with ocean gradients of temperature, salinity, and sea surface height. Thus, vector velocities provide new information to the traditionally assimilated scalar data of temperature and salinity. Because near surface drifters are routinely deployed and available in near-real time for data assimilation, these methods are likely to substantially improve the Navy's operational regional and global ocean forecast systems. This technology also can be applied to other types of in situ ocean observations. While the full water column covariance model can handle depth limited velocity observations, velocity observation in profile form are also usable. Surface currents from satellite or high-frequency radar are also sources of data that can be used with these data assimilation methods.

15. SUBJECT TERMS

Velocity data assimilation
Vertical error covariances
Ocean forecasting
Geostrophic velocity

16. SECURITY CLASSIFICATION OF:			**17. LIMITATION OF ABSTRACT**	**18. NUMBER OF PAGES**	**19a. NAME OF RESPONSIBLE PERSON**
a. REPORT	**b. ABSTRACT**	**c. THIS PAGE**			Robert Helber
U	U	U	U	86	**19b. TELEPHONE NUMBER** *(include area code)* (985) 228-5430

Standard Form 298 (Rev. 8-98)
Prescribed by ANSI Std. Z39.18

This page intentionally left blank.

CONTENTS

This page intentionally left blank.

EXECUTIVE SUMMARY

Assimilation of real-time observations in operational forecasting systems is an essential component for creating skillful ocean forecasts. The assimilation of *in situ* and satellite derived observations are needed for correcting non-deterministic processes (or chaos) that regularly occur in the ocean. Presently, (circa 2022), sea surface temperature and sea surface height and depth profiles of temperature and salinity are routinely assimilated in Navy operational ocean forecasting systems. However, operational forecasting presently does not assimilate *in situ* velocity observations. This report fills this gap by describing an operational ready prototype system for velocity data assimilation and validation that it reduces the prediction error of prognostic variables.

The method for velocity data assimilation is performed in two three-dimensional variational (3DVAR) data assimilation steps. The first step assimilates using traditional methods and data streams of temperature, salinity, and sea surface height, while the second step assimilates the *in situ* observations of velocity using upgraded 3DVAR equations.

This report details both the present Navy operational (circa 2022) 3DVAR equations and methods used in the first analysis step and also the new 3DVAR equations required in the second velocity data assimilation step. Care was taken to explain the existing methods and the needed equation upgrades required for velocity data assimilation. Many appendixes are provided that expand on the equations and method details.

Two validation experiments were conducted using surface drifters deployed in the Gulf of Mexico. One experiment was in 2012 and the other was in 2020. Each experiment had a test case where drifter trajectory-derived surface currents were assimilated in a numerical ocean forecast model, using the two-step 3DVAR approach. Each experiment also had a control simulation of traditional data assimilative single-step forecasts using the same data as that used in the first step of the velocity data assimilation test cases. Therefore, the difference between the control cases and the velocity data assimilation test cases is only the velocity assimilation in the second step.

For the 2012 validation experiment, the 24-hour forecast skill is evaluated relative to the drifters, before they were assimilated. Results showed a substantial improvement of velocity forecast skill when assimilating velocity data. For the 2020 experiment, many diagnostic tests were performed and are presented to demonstrate the effectiveness of the data assimilation methods in both steps. Probability distribution scatter plots, for example, show the assimilation corrections agree with the ratio of errors associated with the observations and the forecast. The analysis increments for velocity also agree qualitatively with the geostrophic balance between temperature, salinity, and velocity.

Validation of forecast skill for the 2020 experiment also showed substantial improvement of velocity forecast skill when assimilating velocity data. Qualitatively, the temperature field at 100 m depth, for the velocity data assimilation case showed substantial improvement in position of a large anticyclonic eddy shed from the Loop Current. The control case, without velocity data assimilation, had this eddy in the wrong place. Validation relative to two glider deployment concurrent with the experiments indicated that the velocity data assimilation case also had greater accuracy in forecasting temperature and salinity.

This page intentionally left blank.

Velocity Assimilation with Improved Synthetic Ocean Profiles (ISOP2): Validation Test Report

1. INTRODUCTION

The Navy's operational ocean forecasting systems rely on data assimilation to constrain numerical solutions (e.g. Jacobs et al., 2014b) subject to non-deterministic processes (e.g. Metzger and Hurlburt, 2001). Traditionally, the observational data used for ocean assimilation are temperature, salinity, and sea surface height anomaly (Metzger et al., 2014). Present Navy operational (circa 2022) ocean forecasting with 3DVAR data assimilation, however, is not able to make use of observations of velocities of ocean currents. Suitable velocity observations are available in near real-time (e.g. Elipot et al., 2016) and thus could be utilized in operational forecasting systems. For this reason, the Naval Research Laboratory has been developing this capability, utilizing ocean velocity observations for constraining the ocean forecasts in data assimilation systems (e.g. Carrier et al., 2016). This report describes the three-dimensional variational (3DVAR) approach to velocity assimilation and provides baseline validation for this system.

This new 3DVAR velocity assimilation system builds on the existing capability of the Navy's Coupled Ocean Data Assimilation (NCODA; Cummings 2005; Smith et al 2012) and the Improved Synthetic Ocean Profile (ISOP; Helber et al. 2013) systems. The present operational implementation of NCODA (versions 3 and 4) employs the ISOP (version 1; ISOP1) system to create synthetic ocean profiles derived from surface observations of temperature and sea surface height anomaly (SSHA). The ISOP1 system uses empirically derived vertical error covariances of temperature and salinity to perform a one-dimensional variational analysis to estimate the subsurface temperature and salinity structure below the surface observations. The ISOP1 analysis is a separate solution independent from the 3DVAR analysis performed within NCODA. During each 3DVAR assimilation cycle, NCODA ingests the ISOP1 solution of synthetic observations. Thus, each assimilation cycle consists of a 1D and then a 3D variational analysis. This approach separates the application of sea surface height (in ISOP1) from the main 3DVAR analysis.

Modern operational forecast resolutions easily resolve mesoscale variability and also permit some submesoscale variability and represent conditional predictability (Jacobs et al. 2014b; Jacobs 2021b). Research has shown that accurate mesoscale forecasting requires smaller scale processes because of a two-way energy cascade that occurs in ocean circulation (e.g. Molemaker et al. 2010). Present observing systems, however, do not resolve below the mesoscales to constrain smaller scales (D'Addezio et al. 2019; Jacobs et al. 2021a). Traditionally, in present operational 3DVAR data assimilation systems (Daley et al. 2000; Jacobs et al 2014b; Rowley and Mask 2014), ocean state variables temperature (T) and salinity (S) are the only quantities constraining ocean circulation models (e.g. Barron et al. 2006; Bleck 2002). Uniquely, velocities are associated dynamically with gradients in geopotential through the geostrophic balance, thus also gradients in T and S. Therefore, we expect velocities be valuable in constraining the model T and S gradient structure. Velocities, however, are associated dynamically with gradients in temperature and salinity through the geostrophic balance. In the approach described in this paper, the velocity observations are filtered to represent mesoscale variability that matches the data assimilation variability scales. Velocity observations, representing the gradient of geopotential, thus will help shape the mesoscale in a way that operational ocean forecasts are traditionally not constrained.

A key issue with ocean velocity assimilation is that the best data sources for near real-time observations are near the surface. The largest source of observations is 15 m drogued drifters from the Global Drifter Program (GDP; Elipot et al. 2016; Lumpkin et al. 2017; Centurioni et al. 2019) and other

Manuscript approved September 30, 2022.

Lagrangian surface drifters (e.g. Berta et al. 2015). Eulerian surface velocity observations can also be inferred from high-frequency radar (e.g. Paduan and Washburn 2013). There are other sources of Eulerian observations at depth, such as drifting floats (RAFOS, Gates et al. 2018 and Argo, Gray and Riser 2014). Other observations may extend over depth such as ADCP (shipboard and moored) and from mooring data such as the Global Tropical Moored Buoy Array (https://www.pmel.noaa.gov/gtmba/). Additional observations may be inferred from depth-averages such as from ocean gliders (Rudnick 2016). All these are still depth-limited and do not provide velocity over the full water column in the deep ocean.

Attempts to assimilate high frequency radar have used, for example, statistical extrapolation (Wilkin et al. 2005) or sequential assimilation techniques using model ensemble derived correlations (Oke et al. 2002). Another approach is obtaining error covariance from the model solution not constrained by data assimilation (Kurapov et al. 2005). There have been efforts to apply velocities in four-dimensional variational (4DVAR) data assimilation with promising results forecasting circulation (Carrier et al. 2014; Muscarella et al. 2015) and sea surface height (Carrier et al. 2016) and using HF radar (Hoteit et al. 2009, Ngodock et al. 2015). See Isern-Fontanet et al. (2017) for a review of surface current data assimilation. Velocities are used for constraints in other types of products including global low-resolution climate models (Zhao et al. 2021) and reanalysis (Wunch et al. 2009). Other methods include assimilation of Lagrangian velocities using local ensemble transform Kalman filter (LETKF; Sun and Penny 2019). All methods have some form of projecting velocity observation through the water column (Wunch 1997). The present approach is that of 3DVAR installed within the Navy's well-documented (e.g. Rowley and Mask 2014) and utilized operational data assimilation system, NCODA (e.g. Smith et al. 2012).

The approach in the present paper is to derive vertical covariance information from historical in situ observations. This vertical covariance relates the variations, in the vertical, between temperature and salinity. The historical data also provides the cross covariance between depths of T and S. The linearized operator from T and S to geopotential height enables this cross covariance to relate T and S to geopotential. An assumption of geostrophy relates horizontal geopotential gradients to velocity. When expressed as a sequence of matrix operations, the transpose of these operators relates velocity at one depth back to T and S at any other depth in the water column. This new vertical covariance model thus enables velocity innovations to create increments of temperature, salinity, and velocity for data assimilation.

The velocity assimilation is performed in two steps. The first step utilizes NCODA, the well-documented 3DVAR data assimilation approach utilized in operational Navy ocean forecasting (e.g., Daley et al. (2000); Cummings (2005); and Cummings and Smedstad (2013); Jacobs et al 2014a,b; Rowley and Mask 1014). The first step utilizes traditional data streams of T, S, and sea surface height anomaly (SSHA) that results in three-dimensional increments of T, S, and u (eastward), and v (northward) velocity. The second step has a modified version of 3DVAR NCODA that ingests only Eulerian u and v velocity observations while utilizing the vertical error covariances of T and S, from ISOP, extended to geopotential. The results are another set of three-dimensional increments of T, S, and u, and v velocity that are added to those from the first step for assimilation.

As part of the upgrade to the NCODA 3DVAR methods, velocity assimilation requires new geopotential covariances to relate velocity errors back to temperature and salinity errors. This new approach, including a new set of covariances in the system, has been configured to work with 3DVAR analyses including velocity observations only. For this reason, the velocity data assimilation presently must be run in a separate analysis. We envision future 3DVAR velocity data assimilation systems can be performed in a single step. Given the present constraints to enable an existing data assimilation system to perform velocity data assimilation, a two-step system is most feasible. Obstacles to performing velocity, T, and S data assimilation together include issues of convergence when velocity observations occur near temperature observations. In addition, the new vertical covariances (described below) required to relate depth limited velocity observations over the water column are not yet compatible with the existing T and S data assimilation system. Future efforts will address these issues to allow for data assimilation of T, S, and velocity together.

The present report contains detailed information about the implementation of velocity data assimilation within the context of the Navy's operational ocean data assimilation systems. The presentation is geared towards DoD and DoD contractors interested in understanding the details of the methods for operational implementation and also research purposes. Some results and methods described in this report are also presented in two publicly released research articles submitted to the journal of Ocean Modelling. These articles are split up into a methods article titled "Ocean Drifter Velocity Data Assimilation, Part 1: Formulation and Diagnostic Results" (Helber et al. 2022) and a validation article titled "Ocean Drifter Velocity Data Assimilation Part 2: Forecast Validation" (Smith et al. 2022). The present report, however, has an additional validation experiment, many detailed appendixes, and Navy specific information not available in the research articles.

In this report, section 2 describes both 3DVAR analyses highlighting relevant details needed for velocity assimilation. Section 3 explains the two-step data assimilation cycle that enables the usage of velocity observations. This validation report contains two experiments both in the Gulf of Mexico with twin numerical simulations, one with velocity data assimilation and one without. Each twin experiment had substantial deployments of ocean drifter observations for data assimilation, one in 2012 (section 4) and another in 2020 (section 5). For the second experiment we performed extensive diagnostic analyses to ensure the system was working. In section 5.6, we present validation results showing that the velocity data assimilation system is superior to a twin experiment where velocity observations are not assimilated. Section 6 contains the conclusion for this report. Appendixes A through G, contain details of key parts of the system. The final section lists 54 references.

2. NCODA 3DVAR ANALYSIS APPROACH

2.1 Version 4.1 3DVAR Equations and Correlation Model

Given the innovations of multiple variable types, we need a Three-Dimensional Variational (3DVAR) Data Assimilation system. The basic 3DVAR equation given by

$$\underbrace{\mathbf{x}_a - \mathbf{x}_b}_{n\times 1} = \underbrace{\mathbf{B}\mathbf{H}^T}_{n\times k} \underbrace{\left(\mathbf{H}\mathbf{B}\mathbf{H}^T + \mathbf{R}\right)^{-1}}_{k\times k} \underbrace{\left(\mathbf{y} - \mathbf{H}\mathbf{x}_b\right)}_{k\times 1}. \tag{1}$$

is found in many books such as Daley (1991) and Kalnay (2003) and most relevantly the NRL report, NAVDAS Source Book (Daley and Barker, 2000). Equation (1) takes the innovations

$$\delta\mathbf{y} = \mathbf{y} - \mathbf{H}\mathbf{x}_b, \tag{2}$$

the difference between the observations $\mathbf{y}$ and the background $\mathbf{x}_b$ state vector and creates increments

$$\delta\mathbf{x} = \mathbf{x}_a - \mathbf{x}_b \tag{3}$$

for correcting the model. The $\mathbf{H}$ operator extracts the background at the locations of the observations and $\mathbf{x}_a$ is the 3DVAR analysis. The background and observation error covariances are given by $\mathbf{B}$ and $\mathbf{R}$, respectively. These state vectors, $\mathbf{x}_a$ and $\mathbf{x}_b$, contain the T (temperature), S (salinity), and velocity vector components u (eastward) and v (northward) of the three-dimensional analysis grid. Appendix A contains a Table that describes each of the variables in equation (1) and the reset of this report. The brackets under the equation indicate the shape of the variables above, where n is the number of analysis grid points times the number of variables and k is the number of observations. In general, in the ocean, k<<n.

The solution occurs by inverting the k by k matrix, which is in observation-space and thus smaller and computationally, since k<<n. As explained in the NAVDAS Source Book (2000), the background error covariance matrix can be written as

$$\underbrace{\mathbf{B}}_{n\times n}\underbrace{\mathbf{H}^T}_{n\times k}=\underbrace{\mathbf{B}\big|_{obs}^{grd}}_{n\times k} \quad \text{and} \quad \underbrace{\mathbf{H}}_{k\times n}\underbrace{\mathbf{B}}_{n\times n}\underbrace{\mathbf{H}^T}_{n\times k}=\underbrace{\mathbf{B}\big|_{obs}^{obs}}_{k\times k}, \tag{4}$$

where $\mathbf{B}\big|_{obs}^{grd}$ is the covariance defined as the expectation of the a quantity squared $\mathrm{cov}\{\mathbf{x}\}=E\left\{\left(\mathbf{x}-\overline{\mathbf{x}}\right)\left(\mathbf{x}-\overline{\mathbf{x}}\right)^T\right\}$, such that $\mathbf{B}\big|_{obs}^{grd}=E\left\{\mathbf{x}_{err}\left(\mathbf{x}_{err}\mathbf{H}^T\right)\right\}$ is the background error covariance between the observation locations and the grid locations while $\mathbf{B}\big|_{obs}^{obs}=E\left\{\mathbf{H}\mathbf{x}_{err}\mathbf{x}_{err}\mathbf{H}^T\right\}$ is the background error covariance between all of the observation locations. The diagonal background error variance, used below, is given by (dropping the matrix dimensions hereafter)

$$\mathbf{V}_{grd}=\mathrm{diag}\left(\mathbf{B}_{grd}\right), \tag{5}$$

for the diagonal variance on the analysis grid. Similarly, the diagonal background error variance at observation locations is given by

$$\mathbf{V}_{obs}=\mathrm{diag}\left(\mathbf{B}_{obs}\right). \tag{6}$$

The observation error variance $\mathbf{R}$ is also diagonal, since we assume all observations are independent. Thus, off diagonal observation error covariances are zero.

In NCODA, the observation operators $\mathbf{H}$ and $\mathbf{H}^T$ are local, such that the stencil size of the respective interpolation operator – which is 1-2 grid steps – is much smaller than the decorrelation scale. To denote this local operator assumption, we approximate equation (4) as

$$\mathbf{B}\big|_{obs}^{grd}=\mathbf{V}_{grd}^{1/2}C\big|_{obs}^{grd}\mathbf{V}_{obs}^{1/2} \text{ and } \mathbf{B}\big|_{obs}^{obs}=\mathbf{V}_{obs}^{1/2}C\big|_{obs}^{obs}\mathbf{V}_{obs}^{1/2}. \tag{7a,b}$$

The elements of the correlation matrices are computed with functions of length scale and distance between observation and analysis grid locations $C\big|_{obs}^{grd}$ or only at observation locations $C\big|_{obs}^{obs}$. The correlation model separates the horizontal, the vertical, and the flow dependence correlations (Jacobs et al. 2014a)

$$C\left(x,y,z,x',y',z'\right)=C_hC_vC_f \tag{8}$$

where C_h and C_v are respectively the horizontal and vertical analytical functions of two locations, $\left(x,y,z\right)$ and $\left(x',y',z'\right)$, and horizontal and vertical length scales at the same points, L_h, L_h', and L_v, L_v'

$$C_h=f_h\left(x,x',y,y',z,z',L_h,L_h'\right) \tag{9}$$

and

$$C_v=f_v\left(x,x',y,y',z,z',L_v,L_v'\right) \tag{10}$$

The horizontal length scale, L_h, is related to the Rossby radius of deformation, which is dependent on latitude by the Coriolis parameter. The lengths for the Gulf of Mexico, from the 2020 experiment described in section 5 below, is approximately 35 km as shown in Figure 1. The function used for C_h follows an atmospheric stochastic-dynamic model (Balgovind et al. 1983; Theibaux 1985) given by

$$C_h=\left[1+\left(s-s'\right)\right]e^{-\left(s-s'\right)/\left[\left(L_h+L_h'\right)/2\right]} \tag{11}$$

where s is the great circle distance between $\left(x,y,z\right)$ and $\left(x',y',z'\right)$. The function for C_v is Gaussian such that

$$C_v = e^{-|z-z'|/[(L_v+L_v')/2]} \tag{12}$$

The vertical length scale L_v is spatially varying, depending on the average density gradient, for the full water column has minimum near the surface of approximately 50 m increasing with depth to nearly 500 m at 3000 m. To help visualize the vertical correlation, we plot the vertical correlation in equation 9 versus depth for the location at 24 N 90 W in Figure 2. High correlation occurs only near the autocorrelation diagonal. The shortest correlation occurs near 50 m depth z (Figure 3). C_f is based on gradients of the surface geopotential height field from the previous forecast and controlled by user specified flow dependent length scales for each variable type (Jacobs et al 2014a).

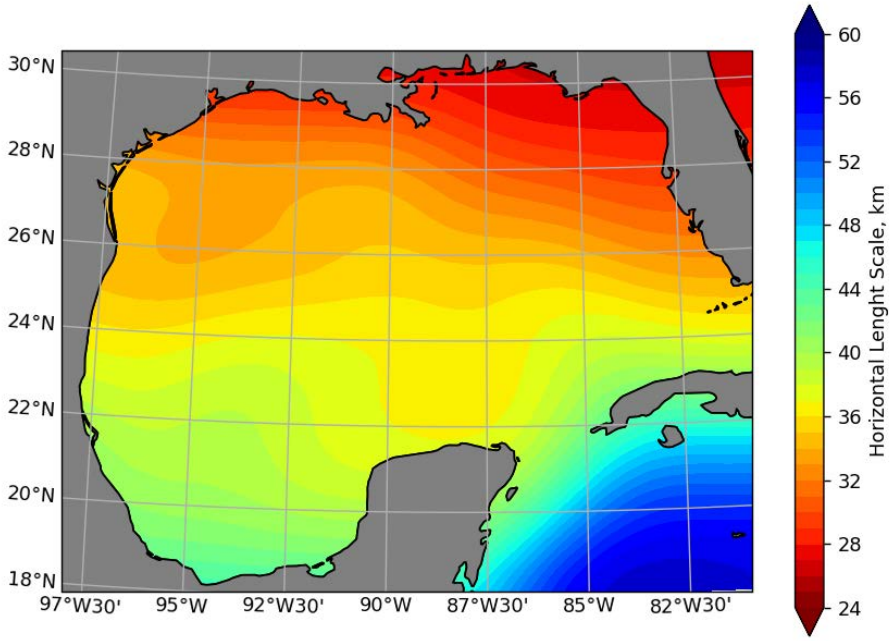

Figure 1. The horizontal length scale used to compute correlations in equation 11. Data comes from the Gulf of Mexico validation experiment described in section 5.

To help visualize the vertical correlation, we plot the vertical correlation in equation 12 versus depth for the location at 24 N 90 W in Figure 4. As we see, the correlations for two depth for two different depth are zero. Only autocorrelations, at the same depth, are related. These values can be confirmed by considering the vertical length scales, which are greater than approximately 10 m (see Figure 3). Thus, the largest e-folding depth difference is approximately 0.1 m. The vertical correlation over the upper 300 m is shown in Figure 5.

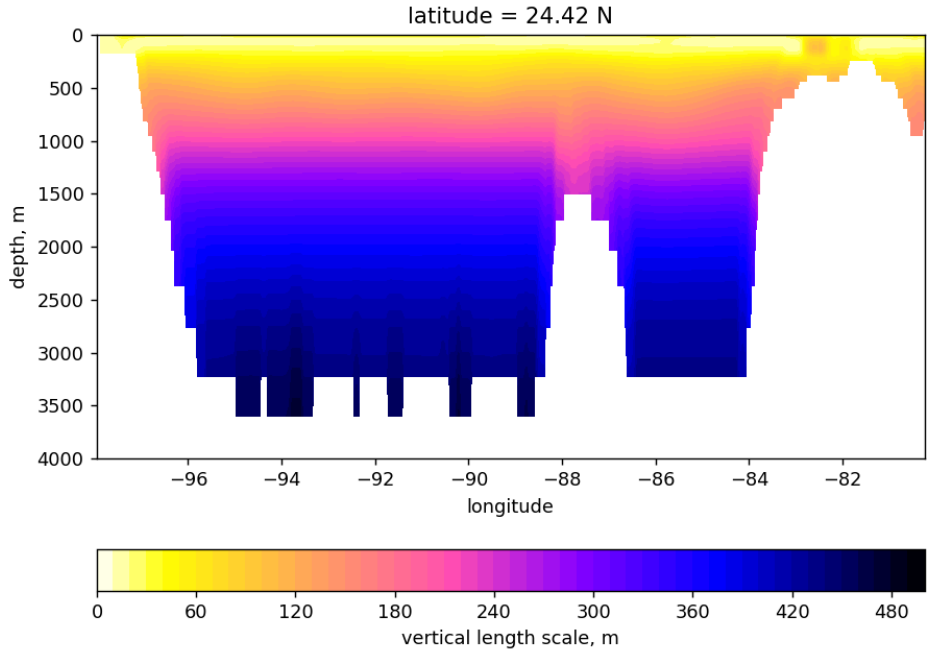

Figure 2. The vertical length scale use to compute correlations using the Gaussian function (equation 12). The length scale is based on density gradients in the near surface but grows with depth. Data comes from the 2020 Gulf of Mexico validation experiment described in section 5.

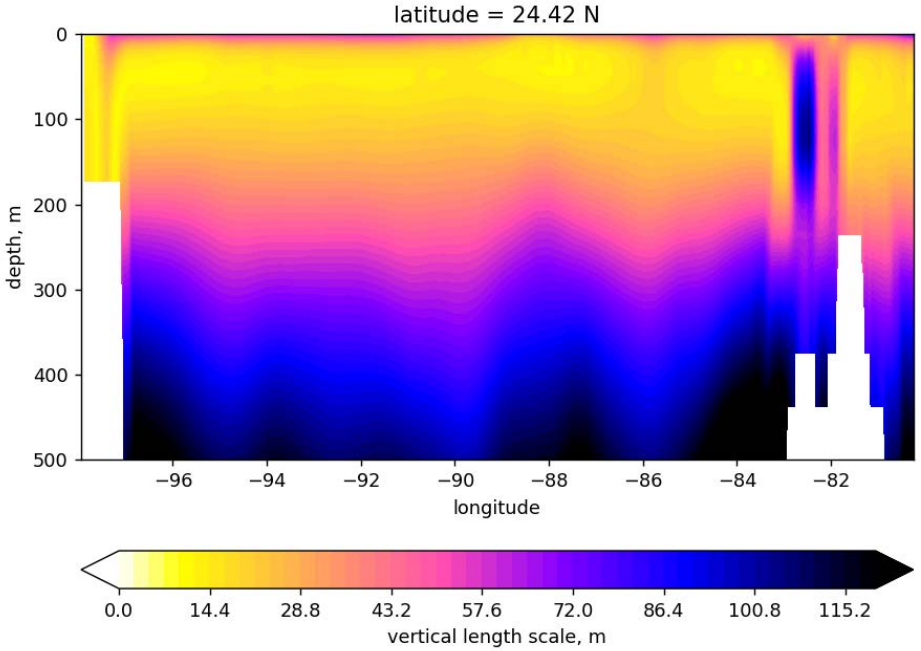

Figure 3. The vertical length scale use to compute correlations using the Gaussian function (equation 12). The length scale is based on density gradients in the near surface but grows with depth. The depht range here is only the upper 500 meters to show the detail structure in the upper ocean. Data comes from the 2020 Gulf of Mexico validation experiment described in section 5.

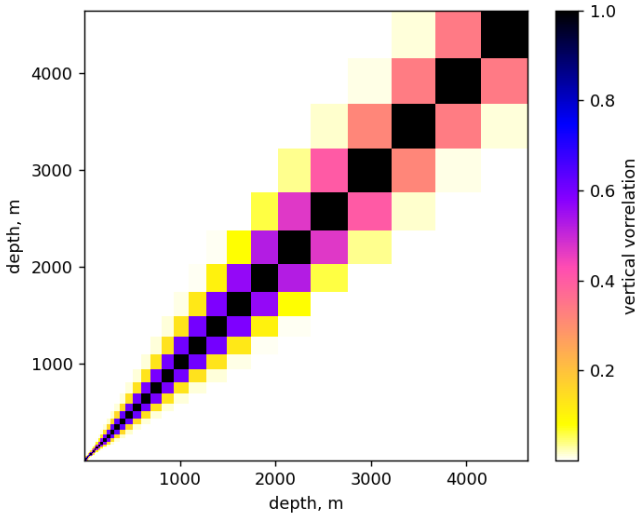

Figure 4. The vertical correlation (equation 12) versus full water column depth for the location at 24 N 90 W in the Gulf of Mexico.

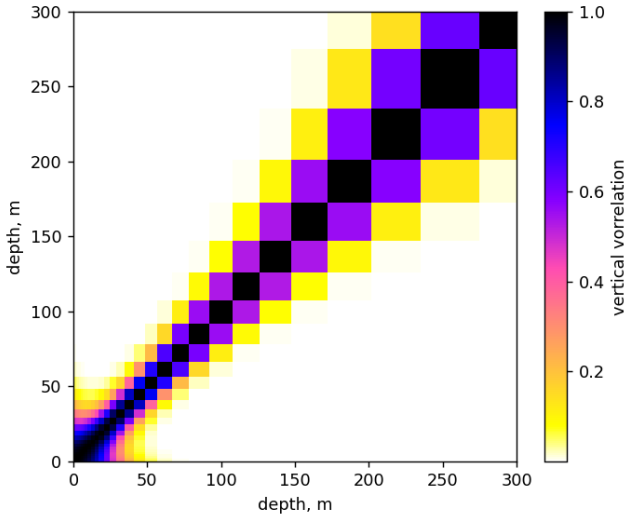

Figure 5. The vertical correlation (equation 12) versus 300 m of depth for the location at 24 N 90 W in the Gulf of Mexico.

The C_f, in equation 8, is based on gradients of the SSHA field from the previous forecast and controlled by user specified flow dependent length scales for each variable type. Note, if observations are non-local, one cannot define their "locations" – imagine one obs is the surface mean temperature and another is the acoustic travel time along a ray path and you still need to know the distance between them to compute correlation.

The interpolations from grid space to observation space is done in NCODA via computations of xi, yj, and zk, which are the fractional grid index values of each observation location. Thus, combining equations 2, 3, and 7 to equation (1) we have

$$\delta\mathbf{x} = \mathbf{V}_{grd}^{1/2} C\big|_{obs}^{grd} \mathbf{V}_{obs}^{1/2} \left(\mathbf{V}_{obs}^{1/2} C\big|_{obs}^{obs} \mathbf{V}_{obs}^{1/2} + \mathbf{R} \right)^{-1} \delta\mathbf{y} \tag{13}$$

Since the model and observation variances, $\mathbf{V}_{obs}$ and $\mathbf{R}$ are diagonal, mathematical manipulation gives

$$\delta\mathbf{x} = \mathbf{V}_{grd}^{1/2} C\big|_{obs}^{grd} \left(C\big|_{obs}^{obs} + \mathbf{V}_{obs}^{-1}\mathbf{R} \right)^{-1} \mathbf{V}_{obs}^{-1/2} \delta\mathbf{y} \tag{14}$$

The above equation is further simplified by replacing the variances, $\mathbf{V}_{obs}$, $\mathbf{V}_{grd}$ and $\mathbf{R}$, with their standard deviation values such that

$$\delta\mathbf{x} = \sigma C\big|_{obs}^{grd} \left(C\big|_{obs}^{obs} + \mathbf{I} + \mathbf{V}_{obs}^{-1/2}\mathbf{R}^{1/2} \right)^{-1} \sigma^{-1} \delta\mathbf{y}\,, \tag{15}$$

We also assume that the $\mathbf{V}_{obs}$ and $\mathbf{V}_{grd}$ are changed to standard deviations and are the same scalar value for each variable type denoted as σ. Also, for the stability of the conjugate gradient solver, there is an added identity matrix. The σ contains scalar values for each variable type, T, S, geopotential G, eastward velocity v, and northward velocity v, and is calculated by taking the root-mean-square (RMS) of the innovations for temperature, salinity, and geopotential. The velocity RMS is estimated from geopotential using the geostrophic balance.

The density dependent vertical gradient is on the order of 10 meters, meaning that observations only correlate in very vertically well mixed areas, such as the surface mixed layer. This approach thus cannot correlate surface observations with the deep ocean. For this reason, the preparation stage of the assimilation system ensures that assimilated observations below the surface are part of an observation profile only.

The density dependent vertical gradient is inherently short, meaning that observations only correlate in very vertically well mixed areas, such as the surface mixed layer. NCODA thus cannot correlate surface observations with the deep ocean. For this reason, the preparation stage of NCODA ensures that assimilated observations below the surface are part of an observation profile only. NCODA 3 and 4, prior to the ISOP2 upgrade, cannot assimilate an isolated observation below the surface that is not part of a profile. Table 1 contains a list of assumptions for NCODA v4.1 3DVAR analysis methods.

Table 1. The list of assumptions applied in the NCODA version 3 and 4, 3DVAR analysis.

Description	**mathematical effect**
sparse observations	k<<n
uncorrelated observations	diagonal observation error variance, $\mathbf{R}$
local observations	no forward H operator needed
analysis grid step is small compared to the decorrelation length scale	separable correlations
background error standard deviation in observation space, single value for each variable	$\mathbf{V}_{obs}^{-1/2}\mathbf{R}^{1/2}$, observation errors in standard deviation too, inconsistency with post-multiplication
vertical correlation is short	limited depth observation cannot be assimilated

2.2 Velocity Data Assimilation Equations and Correlation Model

For velocity data assimilation, we start with equation (14), but with a new vertical covariance model ($\tilde{C}$,described below) the addition of an adjustable stability parameter $\alpha = 1$.

$$\delta\mathbf{x} = \mathbf{V}_{grd}^{1/2}\,\tilde{C}\Big|_{obs}^{grd}\left(\tilde{C}\Big|_{obs}^{obs} + \alpha\mathbf{I} + \mathbf{V}_{obs}^{-1}\mathbf{R}\right)^{-1}\mathbf{V}_{obs}^{-1/2}\,\delta\mathbf{y} \tag{16}$$

Thus, equation 16 is the governing equation used for step-two velocity data assimilation in NCODA (see section 3 below). The two main differences in equation 16, compared to the prior version of NCODA (equation 15), are vertical correlation model, described below, and the full depth varying background error variance $\mathbf{V}_{grd}$. The correct background error matrix is required for velocity assimilation because to project the constraint of velocity observations in the vertical, the influence of observation will extend over a longer depth range. For example, in equation 15, the background error variance is a scalar number for each variable T, S, G, U, and V, denoted σ. For the location at 24.5ºN 90ºW, the correct temperature background error variances profile, used in equation 15 for velocity data assimilation is shown in Figure 6. The profile in Figure 6 indicates that the depth variability is substantial.

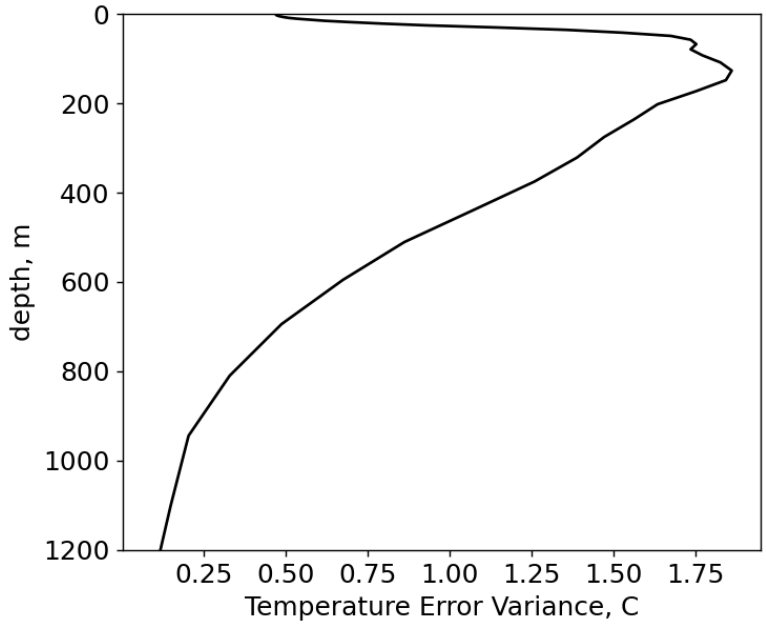

Figure 6. The temperature background error variances profile versus depth for the location at 24.5°N 90°W in the Gulf of Mexico.

The updated background error correlation matrix, $\tilde{c}$, is also required for velocity assimilation to extend observations over a longer depth range. In particular, the correlations

$$\tilde{C}\left(x,y,z,x',y',z'\right) = C_h\tilde{C}_v C_f \tag{17}$$

have a modified vertical correlation, $\tilde{C}_v$. The original version that is dependent on the density gradient is insufficient for relating observations over large depth ranges, which does not allow velocity at a single depth to influence the deep-water column. The new model for $\tilde{C}_v$ is thus, the biggest change to allow for velocity data assimilation. The vertical correlation, C_v (equation 12, Figure 4), is insufficient for projecting the influence of observations over large depth ranges.

The new vertical correlation function $\tilde{C}_v$ varies over latitude and longitude, which is provided by the sample covariances derived from historical observations of T and S on a 0.5 degree grid. As described in the ISOP validation test report (Helber et al. 2013), we have empirically derived vertical covariances at all horizontal locations represented by the truncated empirical orthogonal function (EOF) decomposition of the form

$$\tilde{\mathbf{B}}_{ts,ts} = \tilde{\mathbf{U}}_{ts}\boldsymbol{\Gamma}\boldsymbol{\Lambda}\boldsymbol{\Gamma}^T\tilde{\mathbf{U}}_{ts} \tag{18}$$

where $\boldsymbol{\Gamma}$ is a n_z by 6 matrix, containing the six leading EOF modes listed columnwise, where n_z is the number of depth levels in the empirical database. $\tilde{\mathbf{U}}_{ts}$ is the diagonal standard deviation matrix ($2n_z$ by $2n_z$) derived from the empirical data used to create the vertical covariances. See Appendix B for a full description of equation 18 and how is it computed from randomly sampled *in situ* observations. By definition, the columns of $\boldsymbol{\Gamma}$ represent the principal components of T/S variability in state space, and can be subject to physical transformations (such as specific volume anomaly) to obtain the respective error covariances for geopotential.

To enable velocity assimilation, we extend the T/S vertical correlation matrices to include the geopotential correlation by applying a linear operator, $\mathbf{L} = \mathbf{G}\boldsymbol{\alpha}$, represented by a n_z by $2n_z$ matrix. The $\boldsymbol{\alpha}$ is a matrix that converts T and S variations into specific volume variations and $\mathbf{G}$ performs the computation to determine geopotential height anomalies from specific volume anomalies. Applying this operator to the covariance, we expand the T/S covariance to obtain the $3n_z$ by $3n_z$ covariance matrix

$$\tilde{\mathbf{B}}_{tsg} = \begin{bmatrix} \tilde{\mathbf{U}}_{ts}\boldsymbol{\Gamma}\boldsymbol{\Lambda}\boldsymbol{\Gamma}^T\tilde{\mathbf{U}}_{ts} & \tilde{\mathbf{U}}_{ts}\boldsymbol{\Gamma}\boldsymbol{\Lambda}\boldsymbol{\Gamma}^T\mathbf{L}^T\tilde{\mathbf{U}}_{ts} \\ \tilde{\mathbf{U}}_{ts}\mathbf{L}\boldsymbol{\Gamma}\boldsymbol{\Lambda}\boldsymbol{\Gamma}^T\tilde{\mathbf{U}}_{ts} & \tilde{\mathbf{U}}_{ts}\mathbf{L}\boldsymbol{\Gamma}\boldsymbol{\Lambda}\boldsymbol{\Gamma}^T\mathbf{L}^T\tilde{\mathbf{U}}_{ts} \end{bmatrix} \tag{19}$$

Applied correctly, this approach maintains the positive-semi-definite (PSD) property of the resulting $3n_z$ by $3n_z$ matrix. For more details on this procedure for computing the geopotential covariance from T and S covariance, see Appendix C.

The T/S vertical covariance matrix, $\tilde{\mathbf{B}}_{tsg}$, is decomposed into a diagonal standard deviation matrix and a vertical correlation matrix such that

$$\tilde{\mathbf{B}}_{tsg} = \tilde{\mathbf{U}}_{tsg}\tilde{C}_v\tilde{\mathbf{U}}_{tsg} \tag{20}$$

where $\tilde{\mathbf{U}}_{tsg} = \sqrt{\mathrm{daig}\left(\tilde{\mathbf{B}}_{tsg}\right)}$. Using this new $\tilde{C}_v$ in equation 17, equation 16 becomes the 3DVAR equation used in step-two. Introduction of the vertical correlation model enables computing correlations of the T,S, and geopotential (G) variability with the variations in geostrophic velocity components. Equation 19 requires a capability to compute correlations between an arbitrary pair of points, For that purpose, a special interpolation procedure for the $\tilde{C}_v$ matrix is developed (see Appendix D). Figure 6 shows all the different correlation combinations over the upper 1000 m. Below 1000 m, the correlations are constant with depth, for lack of a better method for extrapolation.

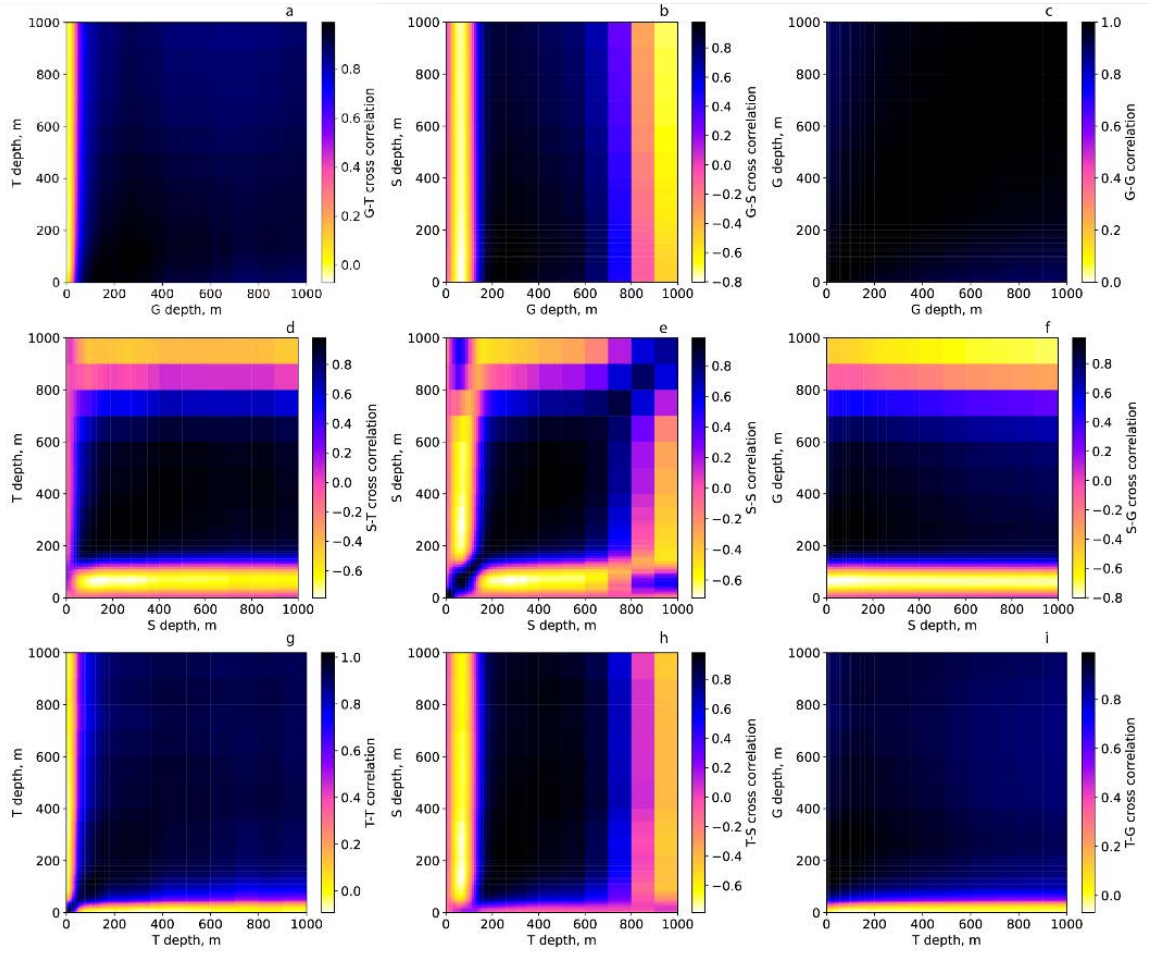

Figure 6. The vertical correlations for T, S, and G in the Gulf of Mexico at 24.5N 90W. The auto-correlations for T, S, and G, are along the diagonal in panels g, e, and c. The off diagonal cross-correlations between S and T and between T and S are in panels d and h, respectivley. The cross-correlations between G and T and between T and G are in a and I, and between G and S and between S and G are in b and f. Since the ISOP correlations are from 0 to 1000 m, the x and y axes cover the same depths. The correlations below 1000 m are taken as constant values from the 1000 m depth correlation, in both x and y directions.

The prototype implementation of the special interpolation procedure for the $\tilde{C}_v$ vertical correlations, as described in Appendix D, has imperfections. For example, the interpolation methods do not preserve asymmetry and do not guarantee ones along the diagonal. Also, the correlations are constant with depth below 1000 m. All of these issue and other potential problems indicate that the prototype system will need improvements to achieve its highest potential.

Introduction of the ISOP vertical correlation model automatically enabled computing correlations of the T, S, and geopotential (G) errors with the errors in geostrophic velocity components. In NCODA 4.1 these correlations are computed by analytic differentiation of the horizontal correlation functions C_h in equation (17) that were kept intact in the upgraded version of NCODA described in the present report.

Remember that the horizontal correlations, C_h , are associated with the background error variance $\mathbf{V}_{obs}$ while the ISOP vertical correlations $\tilde{C}_v$ are associated with the ISOP standard deviations $\tilde{\mathbf{U}}$. This blending of different background error covariances is discussed below in section 2.5 below, regarding future upgrades of the 3DVAR system.

2.3. Forecast Errors

There are four components in the processing of forecast errors. The first step is computing the "Analysis Error Covariance" as described in Daley and Barker (2000,2001). This calculation is the most computationally expensive, which is part of the reason it is not used in the Navy's Global Ocean Forecast System (GOFS; Metzger et al. 2014), and is a reduction of errors due to the assimilation of observations. The complete solution is obtained by (see Daley and Barker 2000 equation 10.1)

$$\mathbf{B}_{anal} = \mathbf{B} - \mathbf{B}\mathbf{H}^T \left(\mathbf{H}\mathbf{B}\mathbf{H}^T - \mathbf{R} \right)^{-1} \mathbf{H}\mathbf{B}. \tag{21}$$

In practice, this equation is normalized, using assumptions of locality, in the same manner for equations 7. Thus, the normalized error analysis is given by

$$\mathbf{V}_{grd}^{(anal)} = \mathbf{I} - C\big|_{obs}^{grd} \left(C\big|_{obs}^{obs} + \mathbf{V}_{obs}^{-1}\mathbf{R} \right)^{-1} C\big|_{grd}^{obs} \tag{22}$$

A detailed derivation of equation 22 is contained in Appendix E. The solution process as applied for equation 15 is similar to that of equation 22. The analysis error covariance is a similar computation to that of the main 3DVAR analysis itself, but this normalized quantity varies between 0 and 1.

The next component is to add the variability of a 24 hour T and S forecast errors, which are computed like this

$$\mathbf{V}_{grd}^{(fcst)} = \frac{1}{\Delta \mathrm{t}_{fcst} \left(24 / \Delta t_{update} \right)} \left[\frac{1}{2} \sum_{i=-10}^{1} w_i \left(\mathbf{x}_i^{fcst} - \mathbf{x}_{i-1}^{fcst} \right)^2 \right]. \tag{23}$$

The previous 10 forecasts are used in the calculation and where Δt_{fcst} is the forecast relaxation timescale in days and where Δt_{update} is the data assimilation update cycle time in hours, which is typically 24.

The next error estimate of the model or persisted analysis forecast error derived from analysis increments. To estimate errors from increments, $\delta \mathbf{x}_1$, we have

$$\mathbf{V}_{grd}^{(inc)} = \frac{1}{\Delta \mathrm{t}_{ferr} \left(24 / \Delta t_{update} \right)} \left[\frac{1}{10} \sum_{i=-10}^{1} w_i \left(\delta \mathbf{x}_{1,i} \right)^2 \right] \tag{24}$$

where $w_i = 0.9^{i-1}$ (Cummings and Smedstad, 2013; Jacobs et a. 2014a). Thus, the calculation utilizes the previous 10 forecast cycles. These three forecast error components are only for T and S forecast errors.

There is one more added forecast error computation that is used to growth back towards the climatological standard deviation levels. This is particularly important in areas that have not seen observation recently. The forecast errors in data poor regions need to be grown towards the climatology error variance levels. Typically, the times scale for this calculation is $\Delta t_{\mathrm{clim}} = 20 \text{ days}$. Finally, all of these errors are applied as

$$\mathbf{V}_{grd}^{(\mathrm{clim})} = \frac{1}{\Delta t_{\mathrm{clim}} \left(24 / \Delta t_{update} \right)} \left[\mathbf{V}_{\mathrm{clim}} - \mathbf{V}_{grd} \right] \tag{25}$$

where Δt_{update} is the data assimilation update cycle time, which is typically 24 hours.

Applying all of these forecast error components together, applied to the ith background error variances, $\mathbf{V}^{(i)}$, gives the background error variance for the next cycle

$$\mathbf{V}^{(i+1)} = \mathbf{V}^{(i)}\mathbf{V}^{(anal)} + \mathbf{V}^{(fcst)} + \mathbf{V}^{(inc)} + \mathbf{V}^{(\mathrm{clim})}. \tag{26}$$

2.4 Computing Velocity Forecast Errors from ISOP Covariances

In equation 18, we have the vertical T, S, and G covariance matrix $\tilde{\mathbf{B}}_{tsg}$. Velocity data assimilation requires the vertical error covariance matrix $\mathbf{B}_{uv}$, for the forecast (or background) velocity components, U (eastward) and V (westward). To obtain a reliable estimate of velocity covariance, $\mathbf{B}_{uv}$, we can construct a substitute $\tilde{\mathbf{B}}_{uv}$ matrix using the correlations for T, S, and Geopotential given by

$$\tilde{C}_{tsg} = \begin{bmatrix} \boldsymbol{\Gamma\Lambda\Gamma}^T & \boldsymbol{\Gamma\Lambda\Gamma}^T\mathbf{L}^T \\ \mathbf{L}\boldsymbol{\Gamma\Lambda\Gamma}^T & \mathbf{L}\boldsymbol{\Gamma\Lambda\Gamma}^T\mathbf{L}^T \end{bmatrix} \tag{27}$$

using the linear operator $\mathbf{L} = \mathbf{G}\boldsymbol{\alpha}$ from equation 18. Given this correlation structure, we can estimate the background error standard deviation, which is the diagonal matrix $\mathbf{U}_{ts}$ such that

$$\mathbf{B}_{tsg} = \begin{bmatrix} \mathbf{U}_{ts}\tilde{C}_{ts}\mathbf{U}_{ts} & \mathbf{U}_{ts}\tilde{C}_{ts}\mathbf{L}^T\mathbf{U}_{ts} \\ \mathbf{U}_{ts}\mathbf{L}\tilde{C}_{ts}\mathbf{U}_{ts} & \mathbf{U}_{ts}\mathbf{L}\tilde{C}_{ts}\mathbf{L}^T\mathbf{U}_{ts} \end{bmatrix} \tag{28}$$

where $\tilde{C}_{ts} = \boldsymbol{\Gamma\Lambda\Gamma}^T$, is the ISOP vertical correlation. Since, a reliable estimate of the background standard deviation is not readily available, an estimate is constructed using that assumption that a linear scale factor k is a suitable conversion in the form $\mathbf{U}_{ts} = k\tilde{\mathbf{U}}_{ts}$, using $\tilde{\mathbf{U}}_{ts}$ from equation 17. As a result, equation 28 becomes

$$\begin{aligned} \mathbf{B}_{tsg} &= \begin{bmatrix} k\tilde{\mathbf{U}}_{ts}\tilde{C}_{ts}k\tilde{\mathbf{U}}_{ts} & k\tilde{\mathbf{U}}_{ts}\tilde{C}_{ts}\mathbf{L}^T k\tilde{\mathbf{U}}_{ts} \\ k\tilde{\mathbf{U}}_{ts}\mathbf{L}\tilde{C}_{ts}k\tilde{\mathbf{U}}_{ts} & k\tilde{\mathbf{U}}_{ts}\mathbf{L}\tilde{C}_{ts}\mathbf{L}^T k\tilde{\mathbf{U}}_{ts} \end{bmatrix} \\ &= k^2\tilde{\mathbf{B}}_{tsg} \end{aligned} \tag{29}$$

The weighting function k, computed via least squares minimization, is described in the Appendix F.

Compute the error standard deviation for geopotential by applying these amplitudes to ISOPs geopotential eigenfunctions:

$$\mathbf{V}_g^{1/2} = \frac{1}{g}\sqrt{diag\left(k\tilde{\mathbf{U}}\mathbf{L}\tilde{C}_{ts}\mathbf{L}^T k\tilde{\mathbf{U}}\right)} \tag{30}$$

Compute the error standard deviation for velocity directly from the geopotential error:

$$\mathbf{V}_{uu}^{1/2} = \mathbf{V}_{vv}^{1/2} = \frac{g\mathbf{V}_g^{1/2}}{hf} \tag{31}$$

where *f* is Coriolis and *h* is the horizontal length scale computed by NCODA.

2.5 Hybrid Background Errors

NCODA 4.1 covariance model assumes that both correlations and variances are independent entities specified by the user. Presented transition to the ISOP covariance model allows generalization of the variance model to a hybrid formulation: with the first component of background error variance, $\mathbf{V}_{NCODA}$, supplied by the NCODA from the analysis of increment history and the second component of

background error variance, $\mathbf{V}_{ISOP}$, coming from ISOP statistics. The hybrid rms variance model $\mathbf{V}_{hyb}$ formulated by taking the weighted mean

$$\mathbf{V}_{hyb} = w\mathbf{V}_{NCODA} = (1-w)\mathbf{V}_{ISOP} \text{ , where } 0 \le w \le 1 \tag{32}$$

where $\mathbf{V}_{ISOP}$ is the representation of ISOP error covariances on the NOCDA grid

$$\mathbf{V}_{ISOP} = diag\sqrt{\mathbf{U}\boldsymbol{\Gamma}_{tsg}^{T}\boldsymbol{\Lambda}\boldsymbol{\Gamma}_{tsg}\mathbf{U}} \quad . \tag{33}$$

This formulation does not account for ISOP contribution to the geostrophic velocity error variance (only TS and geopotential). In the presented upgraded version of NCODA this contribution is parameterized by appending $\mathbf{V}_{ISOP}$ diagonal by the vector of geopotential variances divided by the product of local Coriolis parameter and horizontal decorrelation scale L_h. At the time of writing this approach is not used but under consideration.

2.6 Generalized 3DVAR Approach for Future Upgrades

For future upgrades to NCODA, a generalized equation, normalized to have no units, is more convenient. For this reason, we define two normalized forward operators given by

$$\hat{\mathbf{H}} = \mathbf{R}^{-1/2}\mathbf{H}\mathbf{V} \text{ and } \hat{\mathbf{H}}^{T} = \mathbf{V}\mathbf{H}^{T}\mathbf{R}^{-1/2} \tag{34}$$

Defining also

$$\widehat{\delta\mathbf{d}} = \mathbf{R}^{-1/2}(\mathbf{y} - \mathbf{H}\mathbf{x}_b) \text{ and } \widehat{\delta\mathbf{x}} = \mathbf{V}^{-1}(\mathbf{x}_a - \mathbf{x}_b) \tag{35}$$

we have the transformation of equation (1) to

$$\widehat{\delta\mathbf{x}} = \mathbf{V}\mathbf{C}\hat{\mathbf{H}}^{T}\left(\hat{\mathbf{H}}\mathbf{C}\hat{\mathbf{H}}^{T} + \mathbf{I}\right)^{-1}\widehat{\delta\mathbf{d}} \tag{36}$$

Equation (1) and (36) are mathematically equivalent, as is shown in detail in the Appendix G. Using this equation, NRL is planning to improve NCODA along the following lines:

- Include an option of localizing the ISOP covariances using Schur products of $\boldsymbol{\Gamma}_{tsg}$ with user-defined localization kernels. This will expand the search subspace in optimizing the increments, enable smooth transitions between the standard and ISOP setting of the co-variances and bring in a capability of the hybrid (ISOP/standard) formulation.
- Transition to more general NCODA formulation based on eq. (36) rather than on eq. (14). This development will eliminate the simplifying assumptions listed in the previous section (locality of observations, weak inhomogeneity of error statistics, diagonal observation covariances).
- Bring in a capability of formulating the correlation models in grid space. This will enforce numerically consistent properties of the covariances (symmetry, PSD) and simplify constraining the structure of the background covariances by the user-defined dynamical relationships (Yaremchuk and Martin 2016).
- Generalize formulation of the (renormalized) observation operator $\hat{\mathbf{H}}$ in eq. (36) to include efficient sparse approximations of $\mathbf{R}^{-1/2}$ (e.g., wide swath altimetry) and dynamically con- strained mapping of the analyzed states on the control variables. The latter capability will transform NCODA into a universal analysis engine that includes 4Dvar as an optional dynamically constrained analysis (linearized dynamical constraints and their adjoins will be among the natural ingredients of $\hat{\mathbf{H}}$ and $\hat{\mathbf{H}}$ respectively.

3. TWO-STEP VELOCITY DATA ASSIMILATION

While we envision future 3DVAR velocity data assimilation systems can be performed in a single step, the prototype velocity data assimilation system, for practical reasons, has a two-step assimilation cycle. Given the present constraints to enable velocity data assimilation in an existing Navy operational data assimilation system, a two-step system is most feasible. Obstacles to performing velocity, T, and S data assimilation together include issues of convergence when velocity observations occur near temperature observations. In addition, the new vertical covariances (described below) required to relate depth limited velocity observations over the water column are not yet compatible with the existing T and S data assimilation system. Future efforts will address these issues to allow for data assimilation of T, S, and velocity together.

The first step (step-one; hereafter) in the assimilation cycle uses traditional in situ data streams of temperature (T) and salinity (S) observations and satellite observations of sea surface temperature (SST) and sea surface height anomaly (SSHA) for a traditional 3DVAR analysis. Also, during step-one, a reduction in background errors due to the observations is applied and the velocity forecast errors are created from the T and S forecast error variance. The second step (step-two; hereafter) uses the first step analysis as the background and also the updated background error but ingests only velocity observations for the 3DVAR velocity assimilation analysis. The two steps each produce increments,

$$\delta \mathbf{x}_1 = \mathbf{x}_{a1} - \mathbf{x}_{b1} \tag{37}$$

and

$$\delta \mathbf{x}_2 = \mathbf{x}_{a2} - \mathbf{x}_{b2} \tag{38}$$

that are added together for assimilation in a 6 hour hindcast insertion in 24-hour assimilation cycle

$$\delta \mathbf{x} = \delta \mathbf{x}_1 + \delta \mathbf{x}_2 . \tag{39}$$

Here, $\mathbf{x}_{b1}$ is the background at the start of step-one and $\mathbf{x}_{b2}$ is the background used for step-two. The analysis for step-one and step-two are $\mathbf{x}_{a1}$ and $\mathbf{x}_{a2}$, respectively. Thus, the step-one increment is, using equation (15) becomes

$$\delta \mathbf{x}_1 = \sigma C\big|_{obs}^{grd} \left(C\big|_{obs}^{obs} + \mathbf{I} + \mathbf{V}_{obs}^{-1/2} \mathbf{R}^{1/2} \right)^{-1} \sigma^{-1} \delta \mathbf{y}_1, \tag{40}$$

where $\delta \mathbf{y}_1 = \mathbf{y}_1 - \mathbf{H}\mathbf{x}_{b1}$ are the innovations of T and S only, including synthetic profiles derived from satellite SSHA data. The background, $\mathbf{x}_{b1}$, is from the previous day 24 hour forecast, or for SST, the appropriate forecast at the observation time. The step-two increments come from application of equation (16) becomes

$$\delta \mathbf{x}_2 = \mathbf{V}_{grd} \tilde{C}\big|_{obs}^{grd} \left(\tilde{C}\big|_{obs}^{obs} + \mathbf{I} + \mathbf{V}_{obs}^{-1} \mathbf{R} \right)^{-1} \mathbf{V}_{obs}^{-1} \delta \mathbf{y}_2 , \tag{41}$$

where $\delta \mathbf{y}_2 = \mathbf{y}_2 - \mathbf{H}\mathbf{x}_{b2}$ are the innovations of velocity, relative to the background for step-two, derived from surface drifters deployed in the Gulf of Mexico. The background for step-two is averaged over the inertial period, as described below.

There are benefits from separating these assimilation steps. The first is so that we can explicitly examine the details of the velocity observations and their effects on the analysis. This allows verification of the analysis increments of all state variables due to the velocity observations without interference from the T and S observations. Secondly, the velocity assimilation uses uniquely different vertical covariance structures that relate geopotential to T and S throughout the water column. The step-one exploits several simplifications that cannot be made in assimilation of velocity at isolated points in the water column. The synthetic profiles used in the step-one do not necessitate the large vertical distance relations used in the step-two to produce a dynamical effect throughout the full water column. These simplifications lead to a faster computation. The two-step analysis allows maintaining the present assumptions in step-one while extending the analysis to assimilate velocity observations in step-two.

The ocean data assimilation processing system we use for the prototype system is the Coupled Ocean Atmosphere Modeling Prediction System (COAMPS; Allard et al. 2014). While this system is capable of ocean atmosphere coupled data assimilation modeling, we use the ocean only capabilities of the system (Allard et al. 2012), based on the Navy Coastal Ocean Model (NCOM; Barron et al 2006). The version of COAMPS we use is that used for the 4DVAR processing and is located on Subversion at the address:

`https://www7320.nrlssc.navy.mil/svn/repos/COAMPS/ocn_4dvar@112`

The revision is 112. See Table 2, below.

The following two sections describe in more detail, the two data assimilation steps including the methods for processing the observations and preparing the step-one analysis as the background for the step-two analysis. As a visual guide, the diagram in Figure 7, shows the two-step processing with the equations used in each step. In the next two section, we also describe the details for the velocity data assimilation processing in two steps.

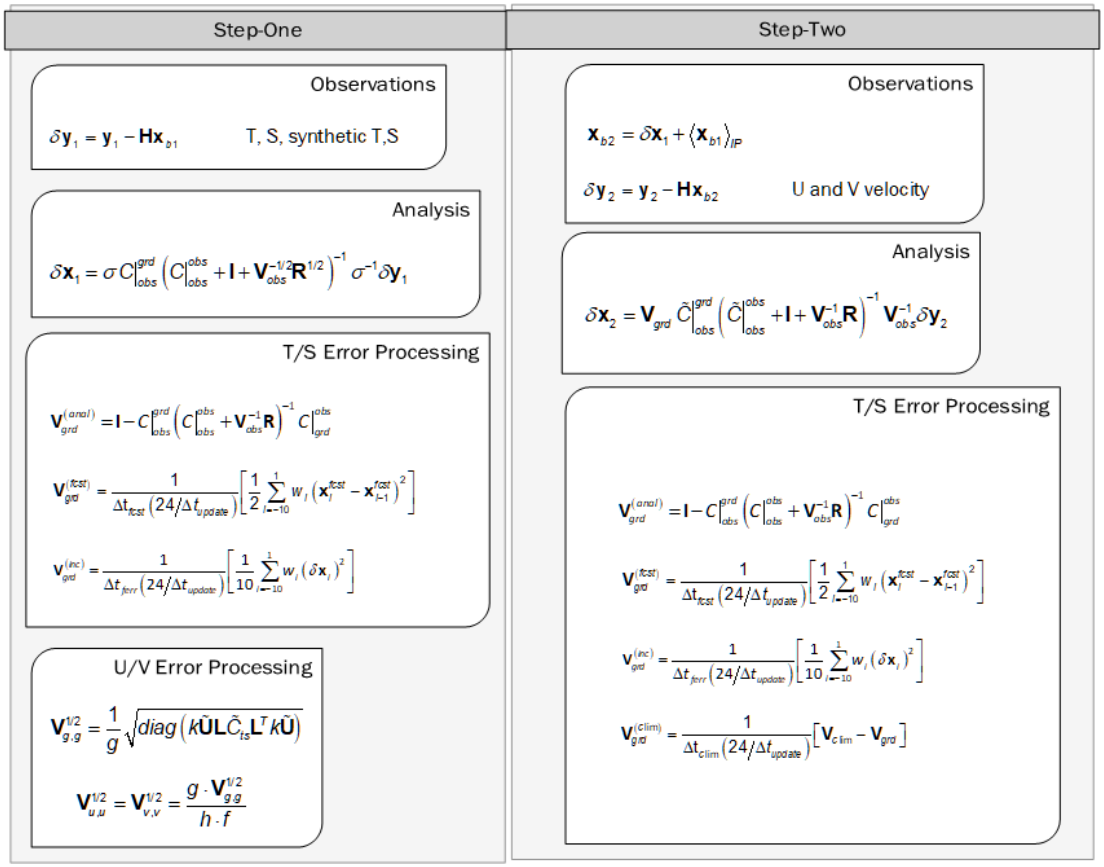

Figure 7. Adiagram of the two-step procsssing steps including the equations used in each step.

Table 2. The 3DVAR equation and NCODA version used or each step of the velocity data assimilation processing. At the end of the subversion address is an @ symbol followed by the revision number.

Processing Step	Equation	NCODA Version	Subversion Address
Step 1	14	4.1	`https://www7320.nrlssc.navy.mil/svn/repos/ncoda_var/branches/v4.1@754`
Step 2	39	trunk	`https://www7320.nrlssc.navy.mil/svn/repos/ncoda_var/trunk@861`

3.1 Analysis Step One: T and S 3DVAR Analysis

The 3DVAR analysis equations are different for each of the two steps. The first step of the Two-Step system, step-one, performs a traditional 3DVAR analysis (equation 40) with traditional data streams. Thus, the innovations are derived from only T and S. No velocity is assimilated in this step. The data preparation, however, computes geopotential (G) from the T and S profiles. Through geostrophic coupling, the 3DVAR analysis creates increments, $\delta\mathbf{x}_1$, for T, S, G and velocity U (eastward) and V (northward). Geostrophic coupling employed through the correlation model, relates innovation of T and S to increments in U and V. The G increments are not used in the dynamical ocean model, NCOM.

The two analysis steps differ also in the processing of forecast errors. The analysis step-one processes the T and S forecast errors as in equations 22 through 24 above but without the term for error growth toward climatology (equation 25; see also Figure 7). The reason to exclude the climatology growth term is that this error growth is applicable for the final analysis and is performed in the step-two only. In step-one, the U and V errors are computed from the T and S forecast errors using equation (31) above.

The first part of the step-one 3DVAR analysis is a preparation stage that creates the innovations, by subtracting the 24-hour forecast (or background) from the observations ($\delta\mathbf{y}_1 = \mathbf{y}_1 - \mathbf{H}\mathbf{x}_{b1}$). The innovations are at the location of the observations on that day, using the first-guess at the time of the obversion (FGAT) for SST data. For step-one, all observations of temperature and salinity result in innovations for direct use in the 3DVAR analysis. The sea surface height anomaly (SSHA) data from satellite altimeters define the innovations for the 1D variational analysis to create synthetic profiles of temperature and salinity using the empirically derived ISOP covariances mentioned above. These synthetic T and S profiles result also in T, S, and G innovations for the 3DVAR analysis.

During the 1st step, the full 3D increment fields ($\delta\mathbf{x}_1$) are created by the 3DVAR analysis. This analysis represents the fields averaged over one day containing updated variability associated roughly with mesoscale variability. The analysis correlation equation (8) has geostrophic coupling and horizontal length scale roughly the size of the Rossby radius of deformation (D'Addezio et al 2019). Thus, the corrections contained in the increments represent mesoscale variability and larger averaged over a day. The increments need to be added to the background to create the background for step-two. Because the purpose is to correct the geostrophic velocity field, the observation processing uses the observed positions separated by one inertial period to infer velocity. A similar processing is conducted on the model background for second step. The increments represent and average over one inertial period, the 24-hour forecast background also need to represent an inertial period. For this reason, the increments are first added to each forecast field 12 hours before and after noon on the analysis day (to represent the inertial period). All of these fields are then averaged together to get a single background for step-two

$$\mathbf{x}_{b2} = \delta\mathbf{x}_1 + \left\langle \mathbf{x}_{b1} \right\rangle_{IP} \ . \tag{42}$$

This is done because the processing for the drifter observations converts the drifter trajectory to a Eulerian velocity from positions separated by the inertial period. Thus, the background and the observations both represent a daily value, consistent with mesoscale dynamics.

The forecast error analysis, during the first step, has a new approach for creating velocity forecast errors that utilizes the approach detailed in section 2.4 ending in equation (31). As a result, velocity errors are derived from the T and S forecast errors. The T and S errors are created and evolved using the standard error analysis using equation, but with the error growth correction turned off, by setting the weight to zero.

3.2 Analysis Step Two: Velocity 3DVAR Analysis

The second step utilizes an updated 3DVAR analysis (equation 41) with only velocity data to produce the step-two increments $\delta\mathbf{x}_2$. The background for step-two is an average of 24 hours of the forecast plus the step-one increments (equation 42). The observations are also "super-observations" (see section 5.3 below), meaning that some drifter locations are averaged together to obtain a larger scale estimate of the velocity. This is done to reduce data density and eliminate sub-mesoscale variability in the observations. These then difference with the background creating innovations from the daily drifter velocities, $\delta\mathbf{y}_2 = \mathbf{y}_2 - \mathbf{H}\mathbf{x}_{b2}$. In the step-two, the forecast errors for T and S are re-computed based on equation 22 through 25, this time with the error growth toward climatology (equation 25). The U and V velocity errors are not computed because, those errors are computed in the step-one from the T and S errors.

4. THE 2012 VALIDATION TEST CASES FOR THE GULF OF MEXICO

There have been two successful experiments implementing the two-step velocity data assimilation system. The first experiment utilized the Grand Lagrangian Deployment (GLAD) of drifters in the in the Gulf of Mexico (GOM) in the summer of 2012. This deployment of drifters was successful and substantially vetted (e.g. Jacobs et al. 2014a). The experiment described below is the first experiment where the velocity data assimilation resulted in an improved ocean forecast. The second experiment is also in the Gulf of Mexico but during the summer of 2020 during a DARPA Ocean of Things deployment of ocean drifters. This second experiment is evaluated and diagnosed to a substantially greater extent than the 2012 experiment. This section (4) describes the 2012 experiment while the 2020 experiment is described in section 5.

The Navy Coastal Ocean Model used for the Gulf of Mexico is baroclinic, hydrostatic, Boussinesq, has a free-surface, and for this experiment, runs at 4 km resolution with 50 vertical levels that are terrain following near shallow topography and z-levels everywhere else (Barron et al. 2006). The model bathymetry for this simulation is shown in Figure 8. The model solution for potential temperature at 107 meters depth, after the second step of velocity data assimilation is shown in Figure 9.

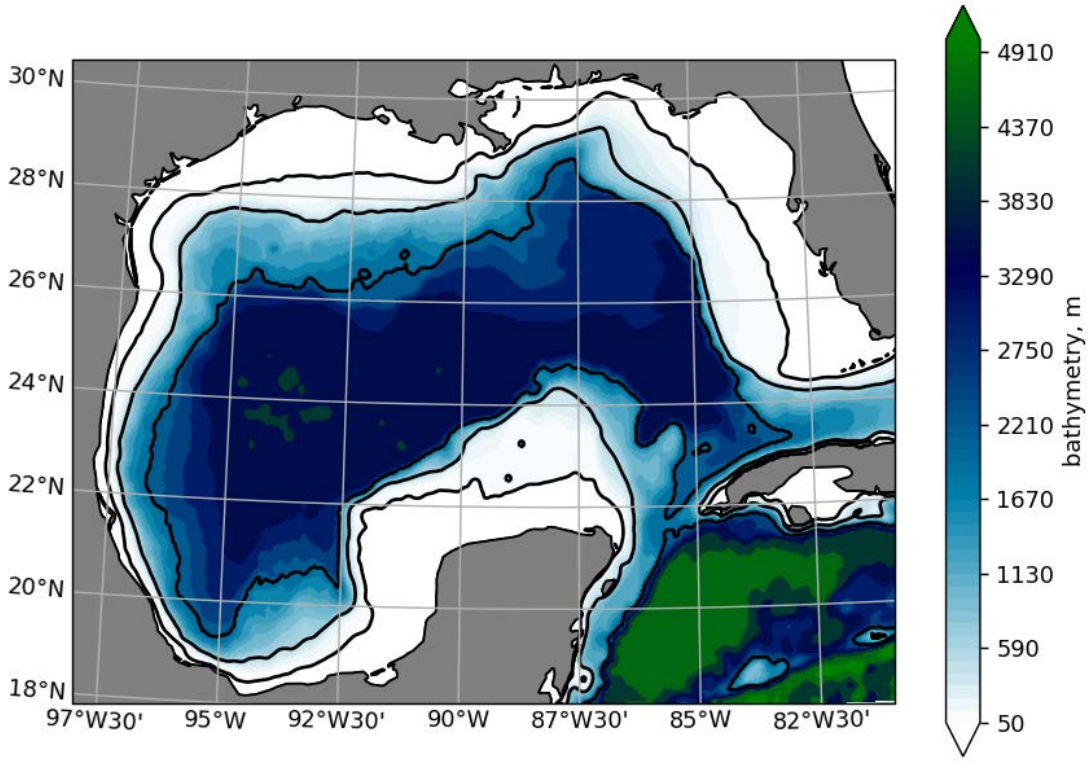

Figure 8. The Gulf of Mexico ocean depth or bathymetry on the model grid for the 2012 simulations. The black contour lines are at 50, 500, and 2000 meters depth.

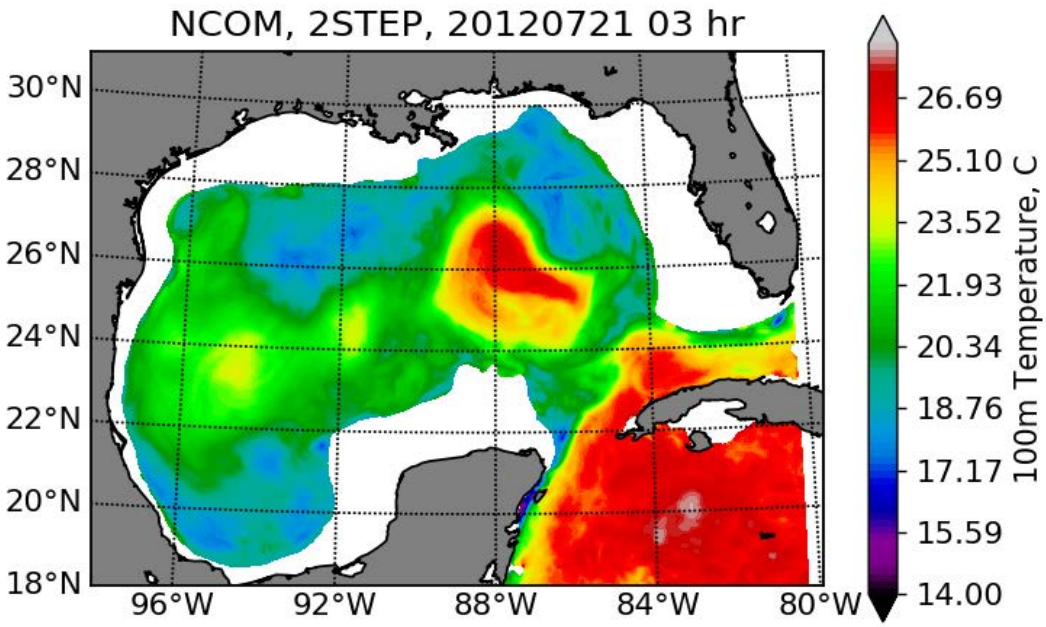

Figure 9. The potential temperature at 107.9 m depth from NCOM at 03:00 GMT, 21 July 2012. This solution is the result after the two-step, velocity data assimilation cycle.

4.1 The Forecast Cycle

The forecast begins from a climatological state on 1 June 2012. We perform a month-long spin-up with traditional data streams of in situ temperature and salinity plus satellite sea surface temperature (SST) and sea surface height anomaly (SSHA) data. Velocity data assimilation is not introduced until 20 July 2012 as described in the next section. Every day NCOM performs a 48-hour forecast with output every 3 hours. After each data assimilation cycle, the resulting increments are inserted over a 6-hour hindcast to provide the initial conditions for the next 48-hour forecast.

4.2 Two-Step Data Assimilation

The data assimilation part of the cycle, after 20 July 2012, has two steps. The first step is a traditional 3DVAR analysis using in situ temperature and salinity, SST, and SSHA data. The second step ingests surface drifter positions from the Grand Lagrangian Deployment (GLAD) in the Gulf of Mexico. The Consortium for Advanced Research on Transport of Hydrocarbons in the Environment (CARTHE) conducted GLAD in the summer of 2012. The GLAD drifter positions are first decimated to retain only locations reported at intervals of 24 hours. These decimated drifter positions then provide trajectory velocities representing roughly a 24-hour average velocity. Innovations are created from these velocities relative to an average of 9 three-hourly forecast velocity fields for the day of the observations.

Figure 10 shows the analysis increment, at 107.9 m depth, for meridional velocity, v, from a second step 3DVAR analysis. While the second step includes only velocity observations in the analysis, temperature (Figure 11) and salinity (Figure 12) increments are also produced. The temperature and salinity increments result from the covariance model that includes correlation between temperature and salinity with geopotential, which itself is related to velocity though geostrophic coupling. The qualitative nature of geostrophic coupling can be seen in Figure 11, where high temperature is found to the right, with respect to the direction of the velocity vectors. In the norther hemisphere, geostrophic velocities are clockwise (anti-cyclonic) around high sea surface height. By virtue of these correlations, the associated variance estimates, and covariance of velocity with temperature and salinity, the second step produces increments in scalar quantities due to the velocity innovations.

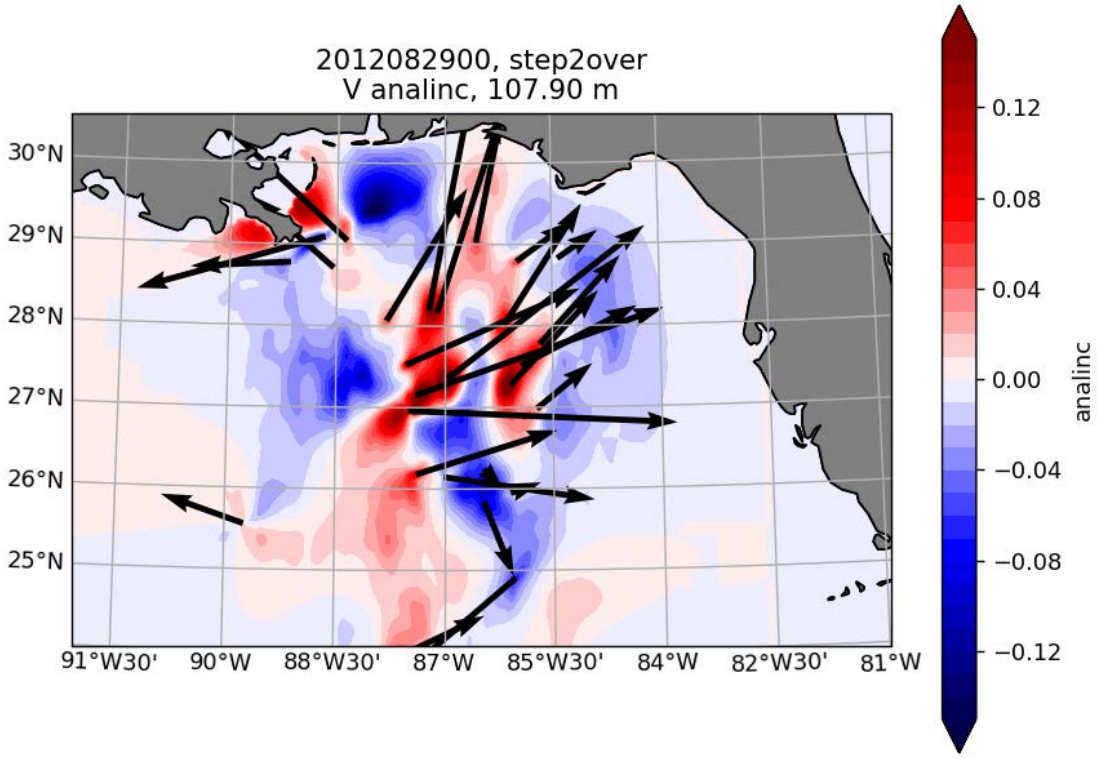

Figure 10. The second step analysis increment, at 107.9 m depth, for the meridional velocity component, V, on 29 September 2012. The black arrows represent the innovation velocity vectors for the same analysis day.

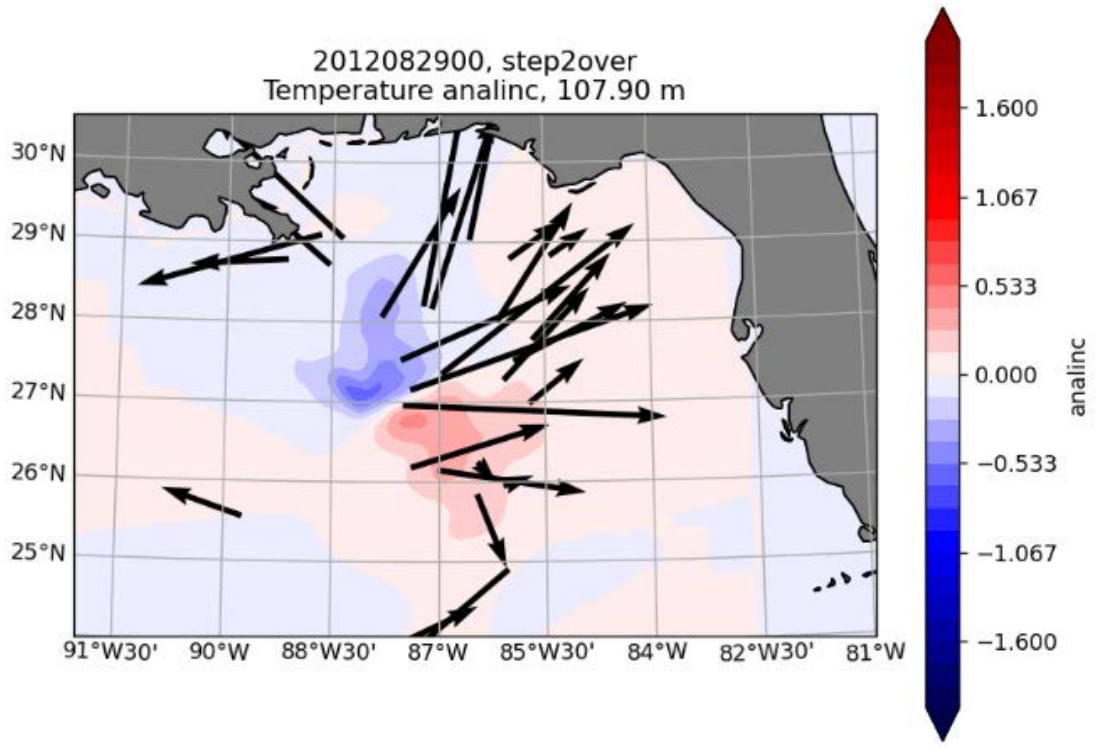

Figure 11. The second step analysis increment, at 107.9 m depth, for temperature on 29 September 2012. The black arrows represent the innovation velocity vectors for the same analysis day.

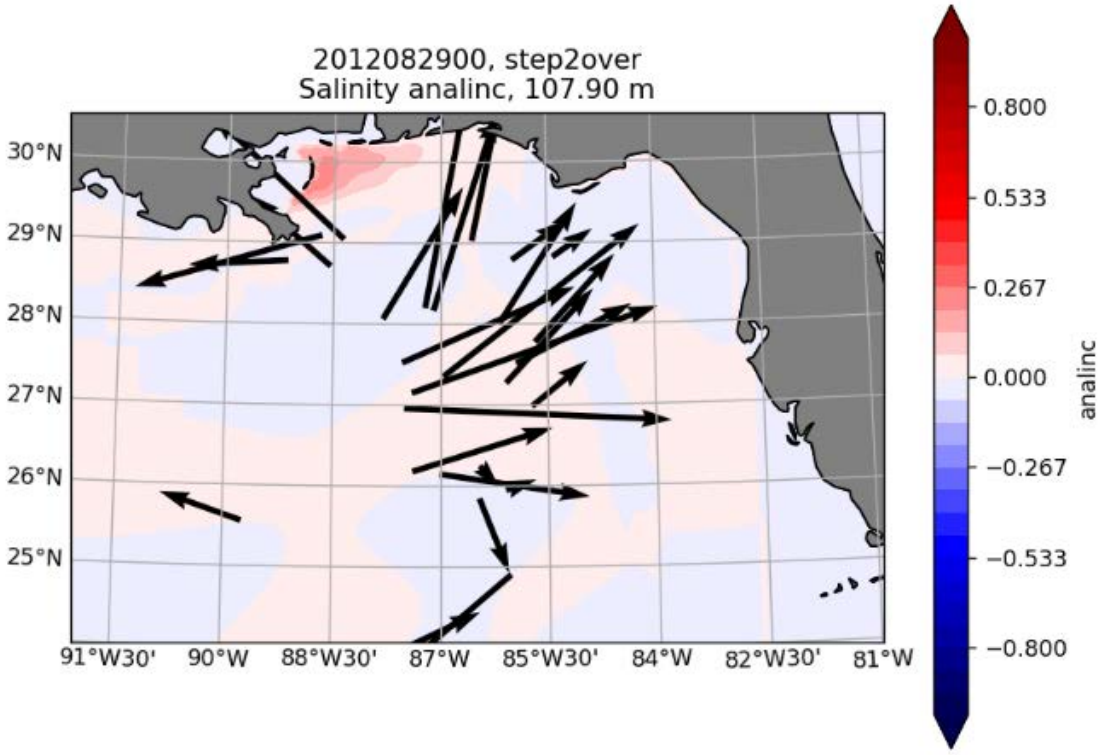

Figure 12. The second step analysis increment, at 107.9 m depth, for salinity on 29 September 2012. The black arrows represent the innovation velocity vectors for the same analysis day.

4.3 Validation Results

Validation is performed by comparing the drifter trajectory velocity speed and direction with the Eulerian velocity speed and direction of the model 24 hour forecast. We have completed twin validation test cases that ran from 25 July until 22 October 2012. The control test (CNTRL) case assimilates temperature, salinity, SST, and SSHA data using a traditional, single 3DVAR analysis, forecast cycle. The experiment test case (TWO-STEP) uses two 3DVAR analyses, as described in the previous section. The first 3DVAR analysis step is identical to the analysis step of the CNTRL case. The differences between the two test cases are due to the application of velocity data assimilation in the second step of the TWO-STEP case. Figure 13 shows the magnitude and direction errors for the TWO-STEP case. Figure 14 shows the magnitude and direction error difference between to the cases.

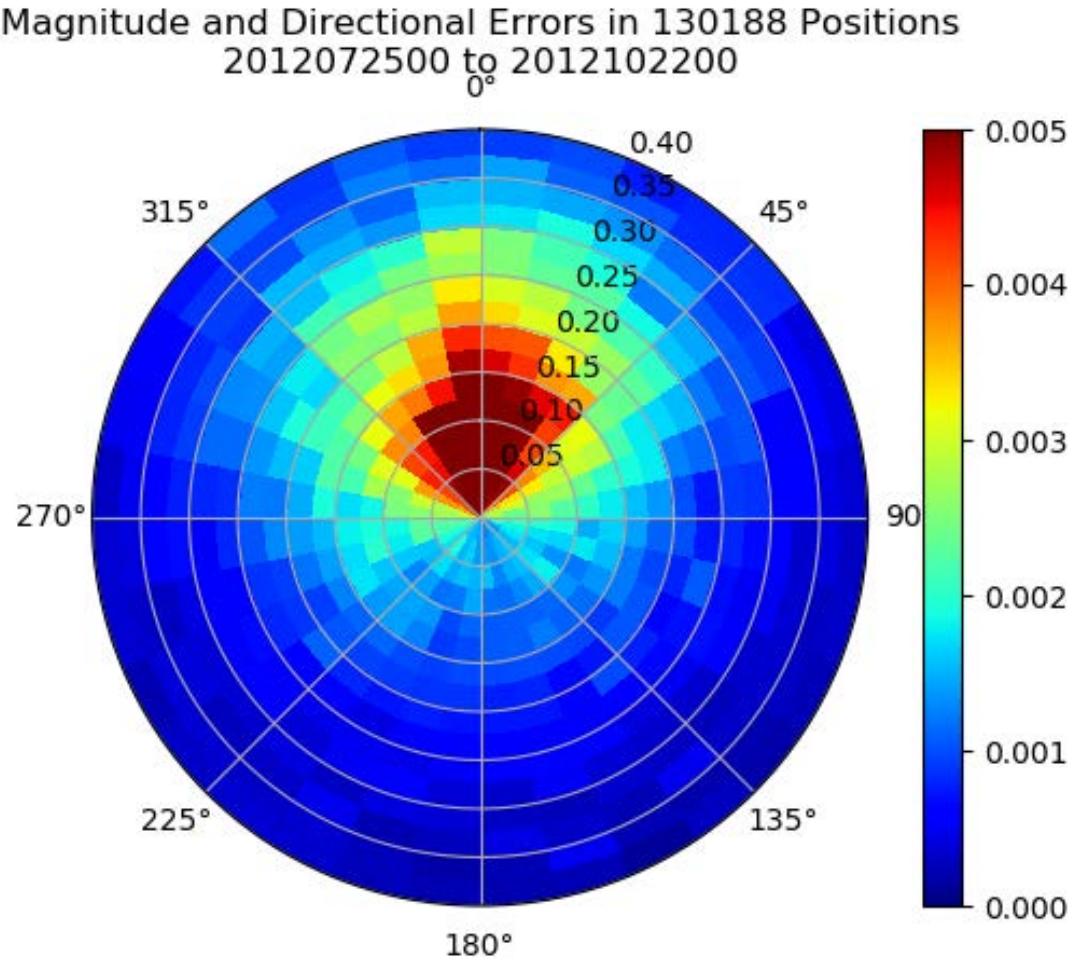

Figure 13. The probability density of velocity magnitude (m/s) and direction (°) errors for 130,188 data points for the 24-hour forecast from the TWO-STEP data assimilation test case. The polar location represents the angular directional error and the radial distance is the magnitude error. The colors represent the fraction of all data in each direction and magnitude pair bin.

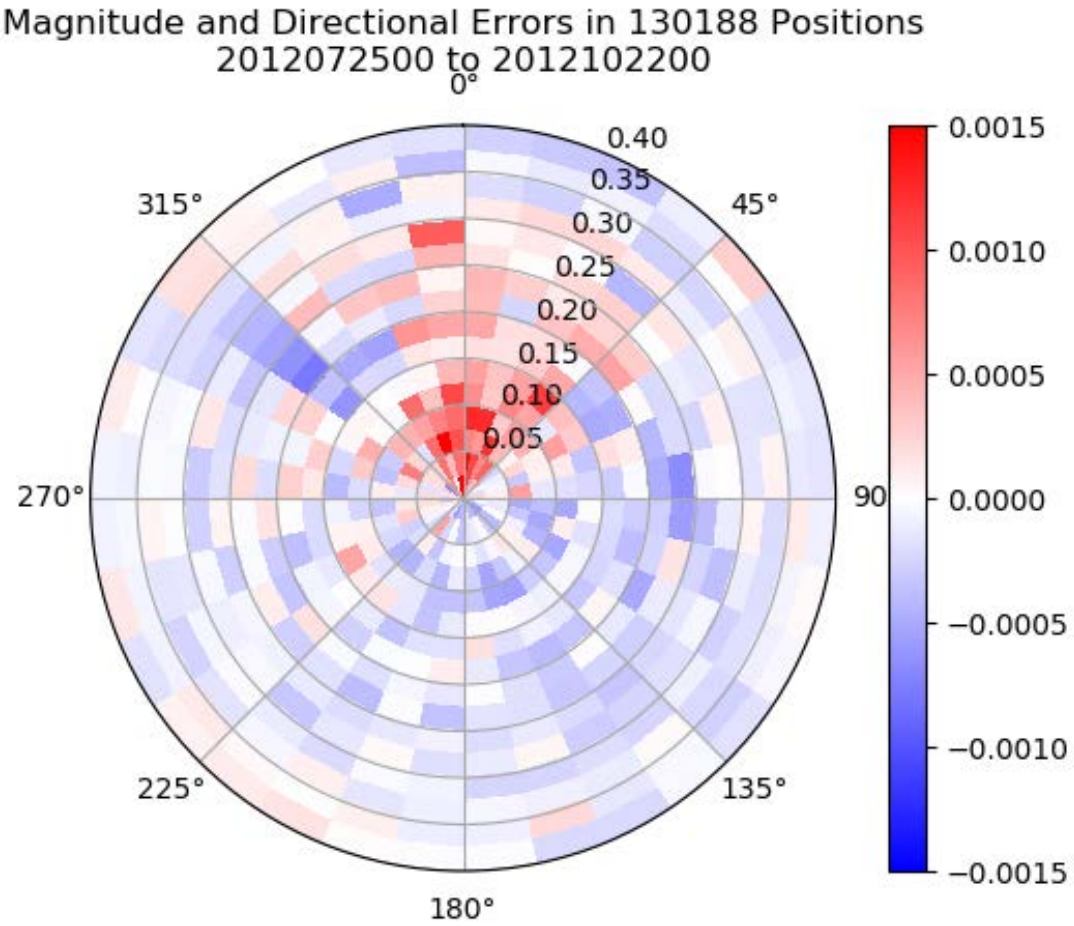

Figure 14. The probability density of the difference between the TWO-STEP minus the CNTRL test cases of the velocity magnitude (m/s) and direction (°) errors. 14-hour forecasts from both cases are compared over the same set of 130,188 observations.

We see in Figure 13 that the TWO-STEP 24 hour forecast velocity errors are generally less than 0.2 m/s in magnitude and 45° in direction. Figure 14 shows the difference in velocity errors with the convention of TWO-STEP minus CNTRL. Thus, relatively more CNTRL comparisons fall in the blue bins, while relatively more TWO-STEP comparisons fall in the red bins. We can see that most of Figure 14 is blue, indicating the large direction errors more often occur in the CNTRL case. The red areas in Figure 14 correspond to bins where both direction and magnitude errors are small, indicating that the TWO-STEP case velocity is likely to be more accurate in the 24-hour forecasts.

5. THE 2020 VALIDATION TEST CASE FOR THE GULF OF MEXICO

The system functionality was tested in the Gulf of Mexico during August through December 2020. During this time period there was a large deployment of 377 drifters in the northeast region of the Gulf of Mexico as part of the DARPA Ocean of Things program. The time period of the experiments was from August 15, 2020 to December 31, 2020, and encompasses the deployment of a large set of deployed drifters (Figure 15). The model domain for the experiments in this paper is the Gulf of Mexico, and spans from 98° W to 80.25° W and 18° N to 30.8° N. The NCOM model uses a spherical projection with an Arikawa C grid discretization. The horizontal grid resolution was 1 km, which corresponds to 1800 and 1420 grid points in the meridional and zonal directions respectively. At 1 km resolution, the ocean model is able to resolve a significant portion of submesoscale features. The model bathymetry for this experiment, at higher resolution than the 2012 experiment, is shown in Figure 16.

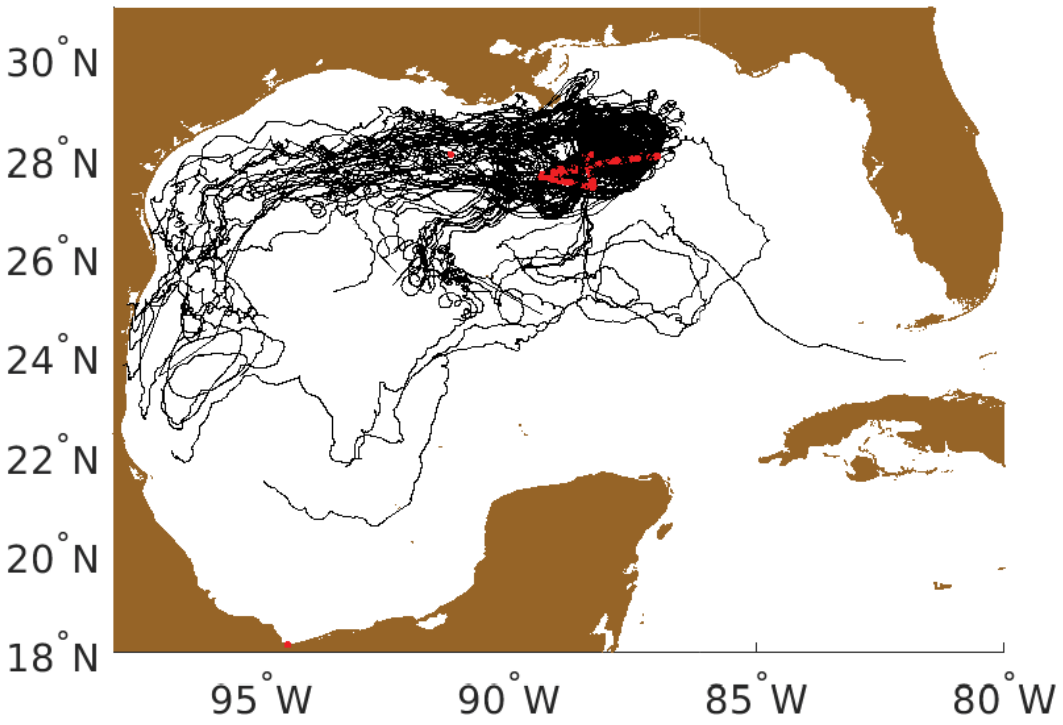

Figure 15: Map of the Gulf of Mexico where the experiments took place. Overlaid on the map are the tracks from 377 drifters that were deployed starting Aug 28,2020 and lasting till Dec 25, 2020 (black lines). The red dots indicate the location of the initial drifter locations.

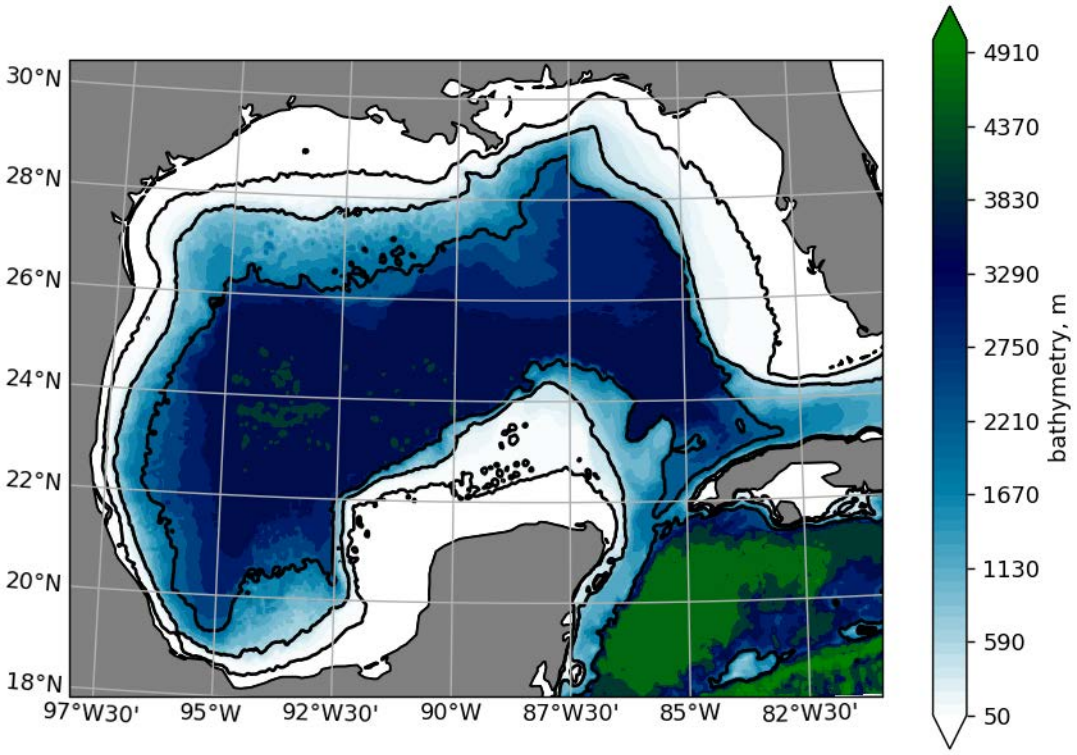

Figure 16. The Gulf of Mexico ocean depth or bathymetry on the model grid for the 2020 simulations. The black contour lines are at 50, 500, and 2000 meters depth.

5.1 The Control Case (CNTRL)

Two experiments were performed, one with velocity data assimilation and one without. The experiment without data assimilation was performed using the standard version of COAMPS using NCODA version 4.1, assimilating the operational stream of observations; consisting of in situ T and S and satellite SST and SSHA observations. The 3DVAR equation 38 is applied in NCODA version 4.1 that is described in section 2 of this report. This experiment was initiated on July 15, 2020 with an initial condition from GOFS, and cycled with daily assimilation until December 31, 2020. Hereafter, this simulation is called the CNTRL case. Due to the daily data assimilation, a 1-month spin-up period, from July 15 to August 15, is more than sufficient to remove any noise or artifacts created by the GOFS initial condition.

5.2 The Velocity Data Assimilation Case (TWO-STEP)

The experiment with velocity data assimilation was performed using the new Two-Step system described in section 3, and assimilated the same data as in the CNTRL experiment, but with the addition of velocities inferred from drifter locations (Figure 15). This experiment was initiated on Aug 15, 2020 directly from the non-velocity data assimilation experiment and cycled until December 31, 2020. The setup of these two experiments are the same so that the differences between the two are due to the velocity data assimilation. The drifters were not deployed until Aug 28 at the location of the red dots in Figure 15. As a result, there was no velocity data assimilation for the first 2 weeks of this experiment, until Aug 29. The updated two-step version of NCODA was still used during this time period, even

though the step-two, which is solely used for velocity assimilation, did not produce any increments. There will still be slight differences between these 2 experiments during these first 2 weeks, because the way the forecast errors are calculated are different and will naturally diverge due to non-deterministic processes.

5.3 Observation Processing

The observations include but are not limited to: satellite SST and SSHA, in situ SST from ships and drifters, and in situ profile T and S from fixed buoys, profiling floats, XBTs (expendable bathythermographs), AXBTs (aerial expendable bathythermographs), CTDs (conductivity, temperature, and depth measurements), and gliders. The observational data are prepared and processed through the NCODA automated data quality control system (NCODA-QC) which identifies spurious observations compared against climatological or model fields and associated variability information (Cummings 2011). Observations that satisfy the quality control are then passed into another NCODA module called NCODA-PREP where they are combined with the previous forecast fields to produce the innovations.

A few million SST observations are collected and read in from NOAA, METOP, and GOES satellites each 24-hour observation window. Therefore, the SST of the Gulf of Mexico is over observed. These are supplemented by in situ observation of SST collected from ships, drifters and buoys. Additional treatment of these observations is applied to better account for the scales and processes represented in the assimilation stage. The First Guess at Appropriate Time (FGAT) method is used in the creation of SST innovations to distinguish between diurnal warming or other temporal changes that are represented by the model and model errors to be reduced by the 3DVAR analysis (Barron et al. 2009). This means that instead of using just the previous forecast at the analysis time to compute the innovations, the forecast field is interpolated from 3-hourly forecast fields to each observation time. Since SST is oversampled, many SST innovations are combined into a super-observation, meaning that observations within one horizontal length scale (of the background error covariance) are averaged together as one observation. The super-observation method projects millions of SST innovations to thousands. The satellite SST observation instrument errors range from 0.3 – 0.5 °C, depending on the satellite, while errors associated with in-situ buoy observations of SST are on the order of 0.1 °C.

SSHA observations from the CryoSat-2, Jason-3, Sentinel, and Altika satellite altimeters are used. SSHA observations have a high resolution along their ground tracks, but tracks are spaced O(100 km) apart. Also, a particular altimeter may only fly over the Gulf of Mexico once every few days. Therefore, since SSHA observations are critical for resolving mesoscale features below the surface, a longer 5-day time window is used for SSHA observations. This means that all SSHA observations collected within the previous 5-days are assimilated. The system does not assimilate SSHA observations directly; instead, SSHA is converted to profiles of synthetic T and S (Helber et al. 2013). In-situ profile observations are treated similarly to SSHA in that the previous 5 days of observations are used. In situ profiles have a much lower observation error and therefore have more influence in the assimilation than the synthetic profiles computed from SSHA observations.

The velocity observations that were assimilated in this experiment were derived from a total set of 377 drifters deployed in the northeast Gulf of Mexico, near the mouth of the Mississippi River (see Figure 15). The drifters were part of the Defense Advanced Research Project Agencey (DARPA) Ocean of Things program. Drifters were deployed August 28-31, 2020. An additional deployment was made October 8-10. The number of active drifters changed day to day, because they either flowed out of the Gulf of Mexico, the GPS malfunctioned, ran ashore, or instruments were picked up. The collection of data from drifters concluded on Dec 25, 2020. For each analysis cycle, drifter positions were read in for the previous 36 hours and up to the next 12 hours surrounding the analysis time. For each drifter identification number, consecutive positions, were used to compute velocities during the observation time window. This produced on the order of ~10,000 individual observations. These high-resolution velocity observations can represent small-scale features that are not resolved by the analysis system. Therefore, the observations were averaged, so that a super-observation is more representative of the mesoscale.

Surface drifters are influenced by a wide range of ageostrophic processes. One is inertial oscillations that can create clockwise rotating currents. This is accounted for by differencing in positions that are approximately one inertial period apart, which is equivalent to averaging individual velocity estimates over one inertial period. The effects of inertial oscillations are also accounted for in the observation errors. The velocity observation error is calculated with a minimum value of $\mathbf{v}_{\text{min error}} = 0.1 \text{ m/s}$ and increases dependent on the position separation time difference Δt_{sep} given by

$$\mathbf{v}_{err} = \mathbf{v}_{\text{min error}} \left\{ 1 + \left[\left(f \left| \Delta t_{sep} \right| / 2\pi \right) - 1 \right]^2 \right\}, \tag{43}$$

where f is the Coriolis parameter. The velocity observation error increases the further the time between consecutive drifter positions is from the inertial oscillation period. Therefore, for the velocity data assimilation experiment in this paper, the velocity observation error was around 0.2 m/s. A check was performed on the final velocity innovations to remove spurious velocities, typically caused by fishing vessels.

5.4 Additional Experiment Settings

The 3DVAR analysis was performed at one quarter of the horizontal grid resolution of the forecast model (which is 1km) in order to save on computation time. Tests were performed and showed that this had minimal effect on the result. Experiments were performed using 220 processors on a super computer. Each analysis/forecast cycles used ~2 hrs of computational time for the non-velocity data assimilation (DA) experiment and about twice this for the velocity DA experiment. A significant portion of this computation time was with computing the analysis error in the post processing. This is because the analysis error calculation requires a significant amount of RAM, and therefore the number of processors had to be reduced down to 22 so as to not exceed the maximum RAM on each node. The velocity DA experiment required more computation time primarily in the post processing with using the vertical covariances to compute the velocity analysis errors.

5.5 Diagnostic Validation Results

5.5.1 Innovations, Increments, Residuals, and Errors

To determine how well the TWO-STEP velocity data 3DVAR analysis is performing, we evaluate the innovations, increments, residuals, and errors for each step of the 3DVAR analysis. The innovations for each step are $\delta\mathbf{y}_1 = \mathbf{y}_1 - \mathbf{H}x_{b1}$ and $\delta\mathbf{y}_2 = \mathbf{y}_2 - \mathbf{H}x_{b2}$, and occur only at the location of the observations. The residual is given by $\delta\mathbf{r}_1 = \mathbf{y}_1 - \mathbf{H}\mathbf{x}_{a1}$ and $\delta\mathbf{r}_2 = \mathbf{y}_2 - \mathbf{H}\mathbf{x}_{a2}$, therefore also occurs at the location of the obversions and provides an estimate of the misfit of the resulting 3DVAR analysis. There are two kinds of errors, those associated with the observations, $\mathbf{y}_{err1}$ and $\mathbf{y}_{err1}$, and those associated with the model forecast, $\mathbf{H}\mathbf{x}_{err1}$ and $\mathbf{H}\mathbf{x}_{err2}$. In this section, we evaluate these errors and the increments $\delta\mathbf{x}_1$ and $\delta\mathbf{x}_2$ at the location of the observations. In the next section will consider increments and errors of the full 3D fields.

Figure 17 shows the step-one observations, analysis, and background data for September 5th, 2020. The numbers in the upper left of each plot are the regression slope, correlation coefficient (r), and root mean square error (RMSE). The two-dimensional histograms indicate the quality of fit in scatter plots of observations versus background and observations versus analysis, for temperature and salinity data. Using linear regression, values of correlation coefficient, RMSE, and slope characterize the 3DVAR analysis. Since September 5th is well into the experiment, the background fits the data well, with a near perfect r value and slope (Figure 17a and 17b). Because the analysis is designed to fit the

observations, to the extent controlled by the observation and background errors, the observation versus analysis regression is slightly better (Figure 17b and 17d). This indicates the 3DVAR analysis is improving the forecast by assimilating increments that improve the background, at the location of the observations.

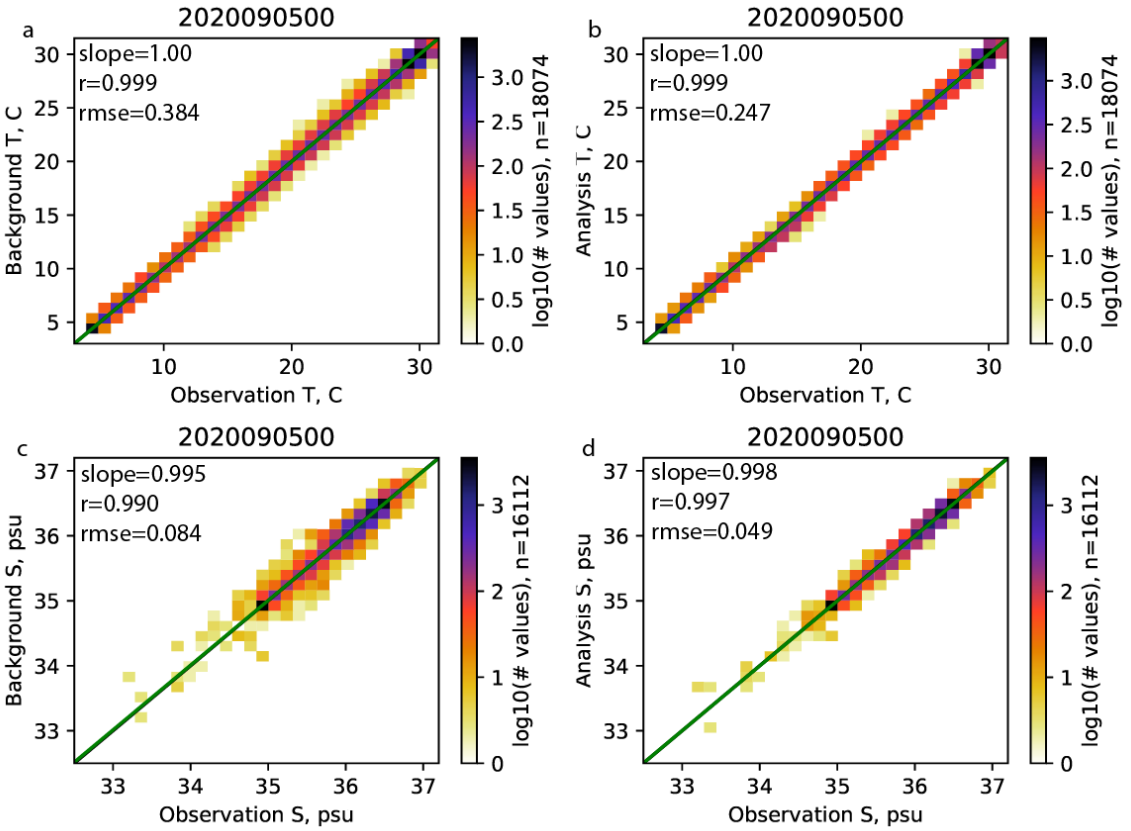

Figure 17. Two-dimensional histogram, scatter plots of step-one (a,c) observations versus background and (b,d) observations versus analysis for (a,b) T and (c,d) S data that is assimilated for the September 5th analysis. The 2D histogram colors represent the log10 of the number of observations that fall in each bin, which include 31 evenly distributed bins over the x and y axis. In the upper left corner of each plot is the regression slope, correlation coefficient (r) value for the green line, and root mean square error (rmse). The number of assimilated observations, n, is indicated in the color bar label.

The step-one increments, in general, are smaller than the innovations, which can be seen in the slopes in Figure 18a and 18b. In Figure 18, regression lines for the step-one increments versus the innovations have slopes that are less than one, 0.561 and 0.562 for T and S, respectively. This indicates that the increments are a little more than half the magnitude of the innovations. The slopes in Figure 18a and 18b are related to the ratio of the background versus observations errors. To demonstrate this relationship, Figures 18c and 18d are created such that the slope is related to the Kalman gain factor, $\mathbf{BH}^T\left(\mathbf{HBH}^T+\mathbf{R}\right)^{-1}$ of equation 1 above. The increments are on the left-hand-side while the innovations are on the far right side of equation 1. Thus, the Kalman gain is the slope of the regression between the innovations and the increment. Since the Kalman gain is the ratio of the background versus the background plus the observations errors, the slopes in Figures 18c and 18d are as estimate of the average Kalman gain of the system.

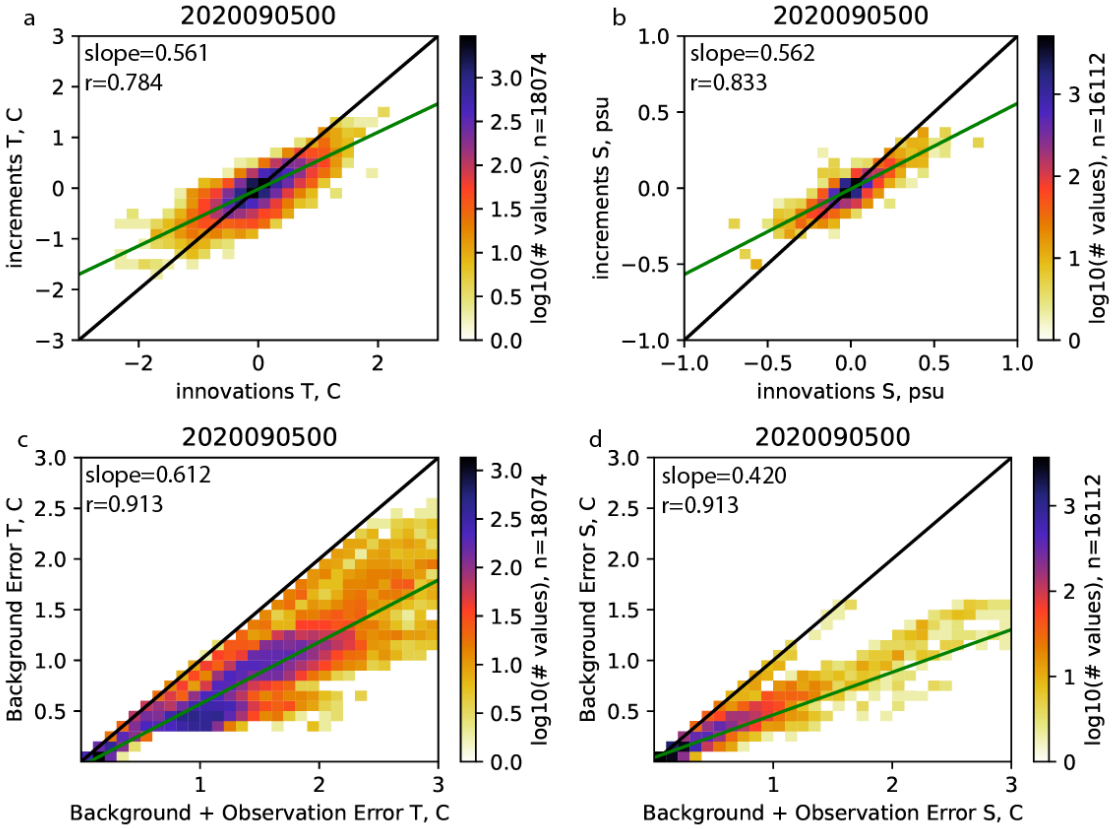

Figure 18. Two-dimensional histogram, scatter plots of step-one of (a,b) innovations versus increment and (c,d) background plus observation versus background errors for data that is assimilated for the September 5th analysis. The 2D histogram colors represent the log10 of the number of observations that fall in each bin, which include 31 evenly distributed bins over the x and y axis. In the upper left corner of each plot is the regression slope and r value for the green line. The number of assimilated observations, n, is indicated in the color bar label.

A similar analysis is performed for the step-two analysis, for u and v data. Figure 19 shows the step-two U and V observations, analysis, and background data for September 5th, 2020. Because the slopes in Figure 19 are not one, there is a mismatch between the velocity observations versus the background and analysis. The encouraging result is that the analysis (Figure 19b and 19d) has a slope closer to one, a correlation coefficient that is higher, and an RMSE that is smaller than the background (Figure 19a and 19c). This indicates the assimilation is fitting the observations closer than the background. Similarly, the step-two velocity increments are not as large as the innovations (Figure 20). Because the slope of the regressions in Figure 20 are less than 0.5, the increments are less than half the magnitude of the innovations. Thus, the velocity 3DVAR analysis is fitting the velocity observations weaker than the step-one analysis fits the T and S data. This may be due to the relatively large observation error, which tends to be approximately 0.196 m/s, which is large compared to the innovations themselves.

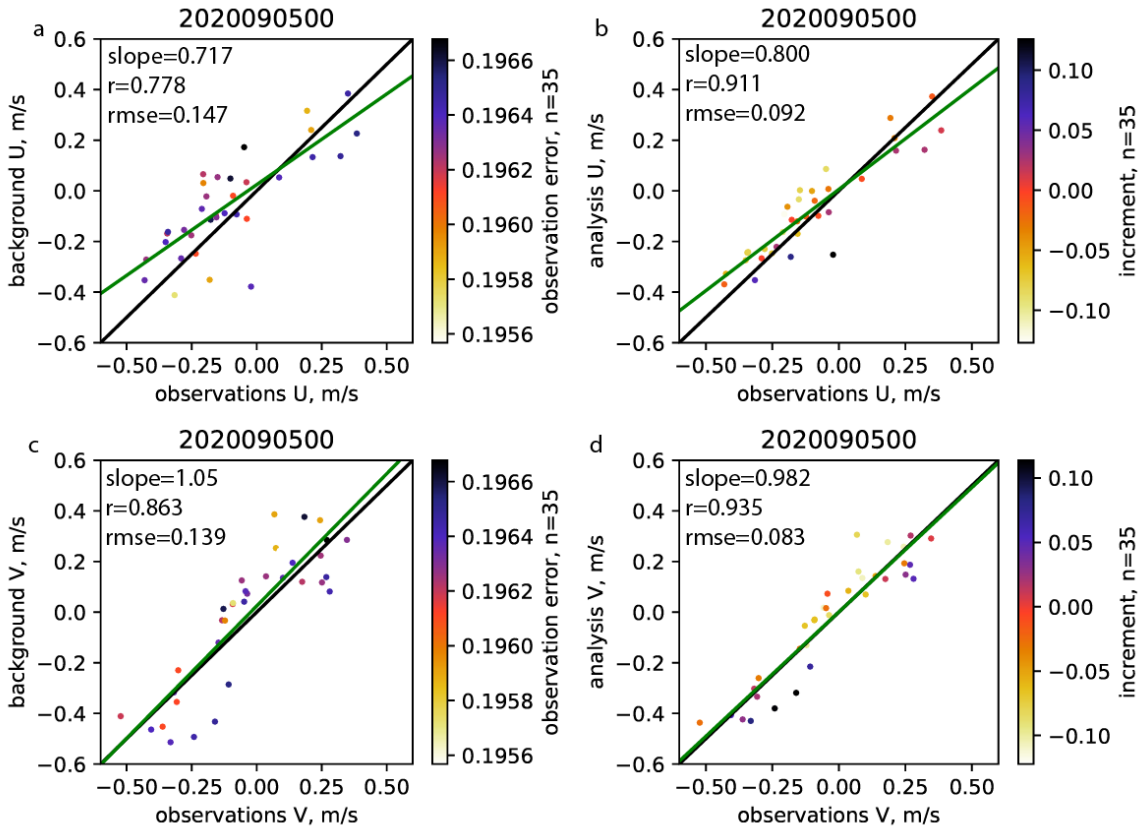

Figure 19. Scatter plots of step-two (a,c) observations versus background and (b,d) observations versus analysis for (a,b) U and (c,d) V data that is assimilated for the September 5th analysis. The colors are the observation value in (a and c) and the increment value in (b and d). In the upper left corner of each plot is the regression slope, correlation coefficient (r) value for the green line, and root mean square error (rmse). The number of assimilated observations, n, is indicated in the color bar label.

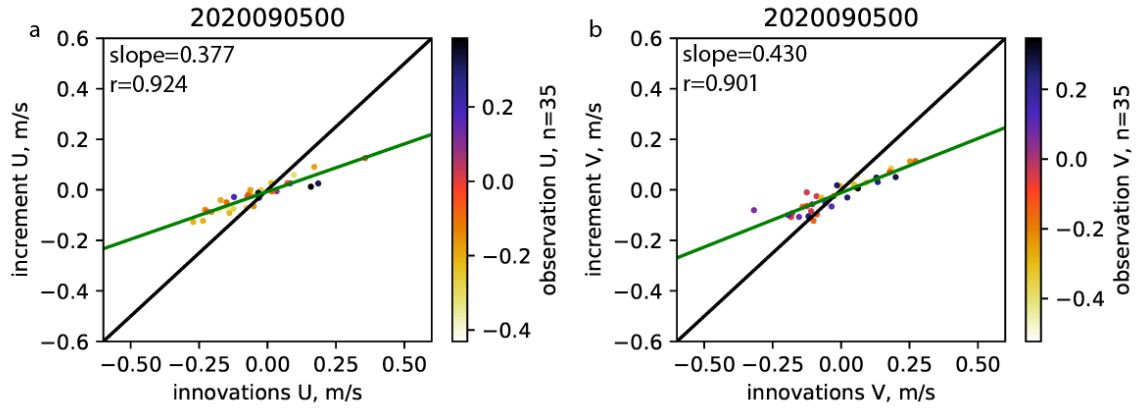

Figure 20. Scatter plots of step-two innovations versus increments for (a) U and (b) V data that is assimilated for the September 5th analysis. The colors are the observation values. In the upper left corner of each plot is the regression slope and r value for the green line. The number of assimilated observations, n, is indicated in the color bar label.

The observation, background, and observation plus background errors for step-two are shown in Figure 21. The preparation stage of the modified NCODA has a rudimentary methodology for estimating the errors for the drifter observations. The drifter observation error has a minimum value of 10cm/s and increases exponentially for increasing time between drifter locations from 24 hrs (see equation 43). The drifters are recorded at constant intervals, therefore, producing the same error. Future research will determine a more realistic approach that accounts for actual phenomenon influencing observation accuracy.

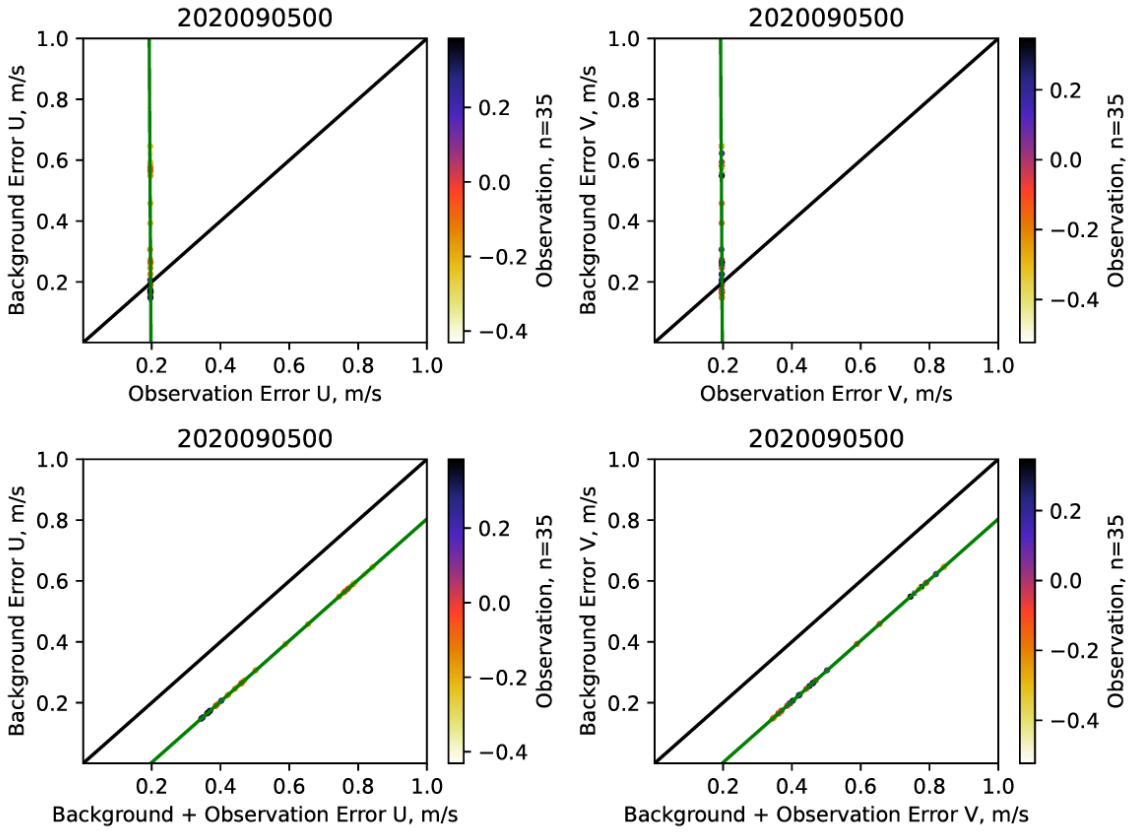

Figure 21. Scatter plots of step-two (a) U and (b) V observation versus background error and (c) U and (d) background plus observation versus background errors for the September 5th analysis. The colors are the observation values. In the upper left corner of each plot is the regression slope and r value for the green line. The number of assimilated observations, n, is indicated in the color bar label.

To provide a timeseries of the 3DVAR velocity assimilation in step-two, Figure 22 shows the slope and correlation coefficient from the start of velocity data assimilation until September 21st. The regressions are between the U and V observations and the background and analysis. The regression is larger and the slope is closer to one for the observation versus analysis regressions. This confirms that the velocity data assimilating is making the analysis more accurate, since the analysis fits the observations more closely.

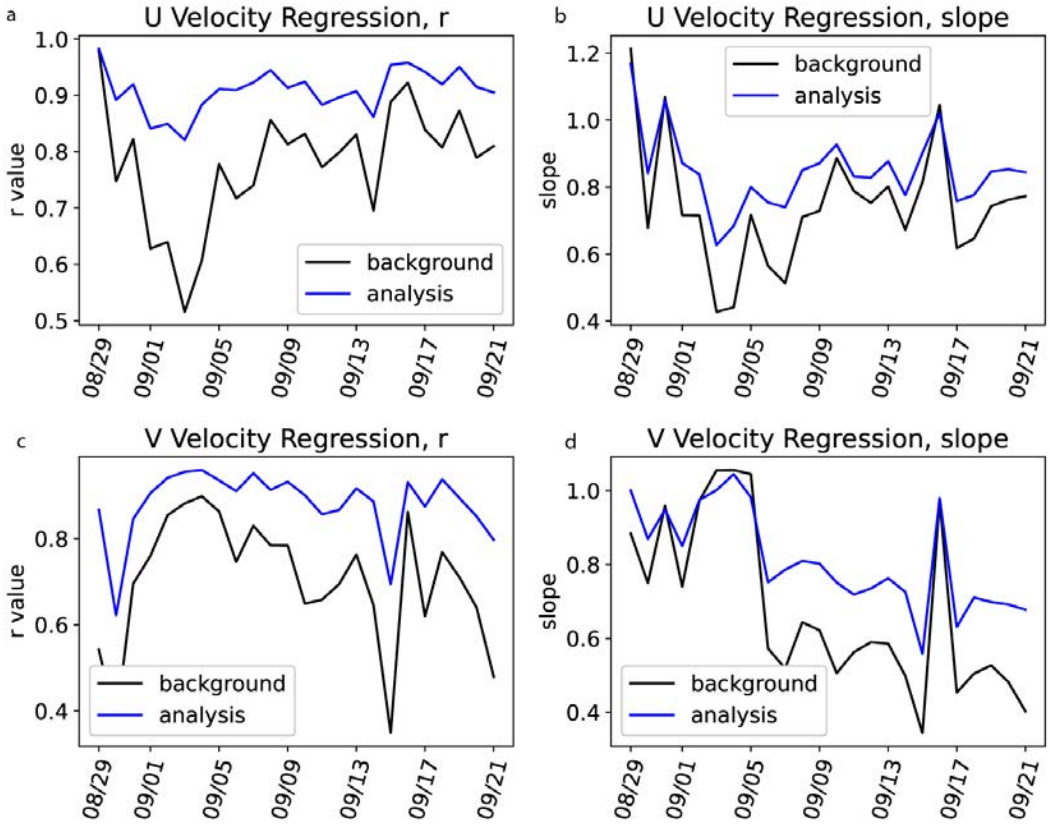

Figure 22. The linear regression (a and c) goodness-of-fit (r value) and (b and d) slope for (a and b) u and (c and d) v velocity observations versus background and analysis. The blue lines are for the observation versus analysis regression and the black lines are for the observation versus the background regression.

At the start of the velocity assimilation, the forecast system was already skillful. Thus, we expect velocity assimilation to provide and improvement relative to an already accurate system. The velocity innovations (Figure 23) maintain roughly twice the magnitude of the observation error which is roughly 0.196 m/s. The velocity magnitudes themselves are larger than the innovation and the observation error. At the start of velocity data assimilation, in early September, the innovations decrease (Figure 23c) as the number of observations increase (Figure 23a). On September 15, there was an increase in observations with an increase in median innovations. Again, in October, an increase in observations is followed with a decrease in innovations. Towards the end of the drifter deployment, when the observation number go down, the innovations increase as fewer observations constrain the system.

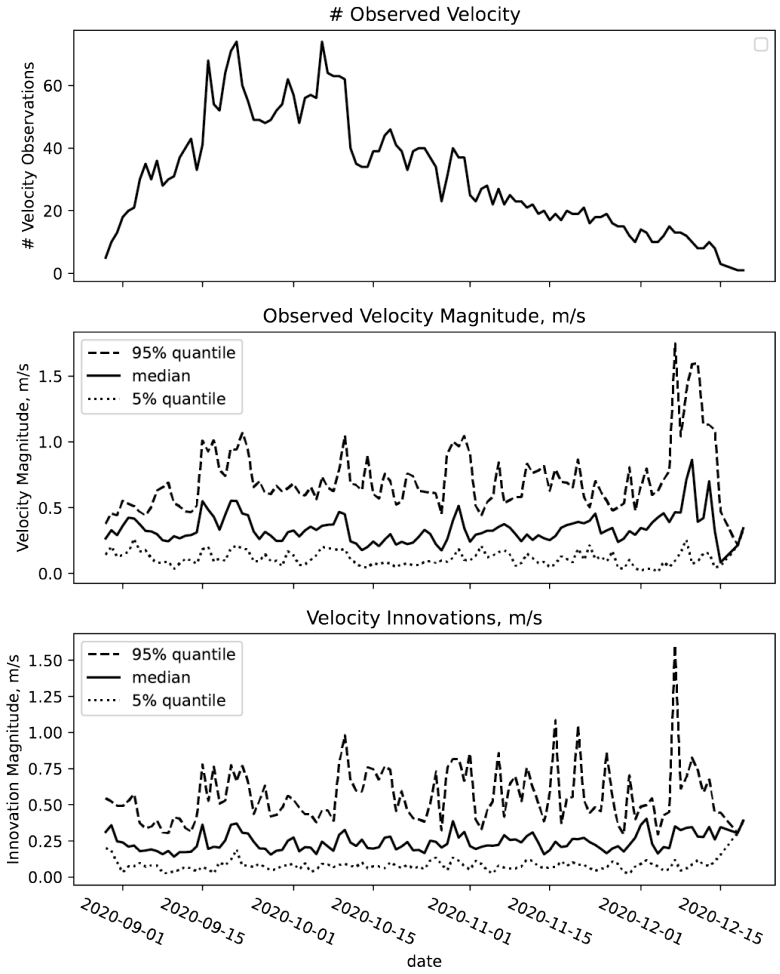

Figure 23. The a) number of observations assimilated, the median b) observed and c) innovation velociy magnitude versus date from the step-two analysis. Velocity observation begin on August 15 and end on December 25th, 2020. The 5% quantile (dotted line) and the 95% quantile in b) and c) show the spread of velocity magnitude on each day.

To visualize the analysis increments relative to the forecast errors, Figure 24 show the T, S, U, and V forecast errors with velocity innovations plotted on top, for the September 5th, 2020 analysis. The forecast errors are those as a result of the step-one analysis cycle and the velocity increments are from the step-two analysis.

To diagnose the effect of velocity innovations on the resulting increments of T, S, U, and V, Figure 25 shows the velocity innovations from step-two plotted on top of the increment. Because the observations are super positioned at a daily sampling interval the innovations represent a mesoscale or geostrophic displacement relative to the forecast background. Thus, the T and S increments need to adjust according to the geostrophic balance. This can be seen in Figure 25a. Because geostrophy dictates that warm water occurs in the center of anti-cyclonic eddies, when facing in the direction of the velocity, warm water will occur to the right of the velocity innovations. This is also true in Figure 26a, that shows the innovation vectors relative to geopotential increments. The increments confirm that the geostrophic balance is upheld in the velocity data assimilation system.

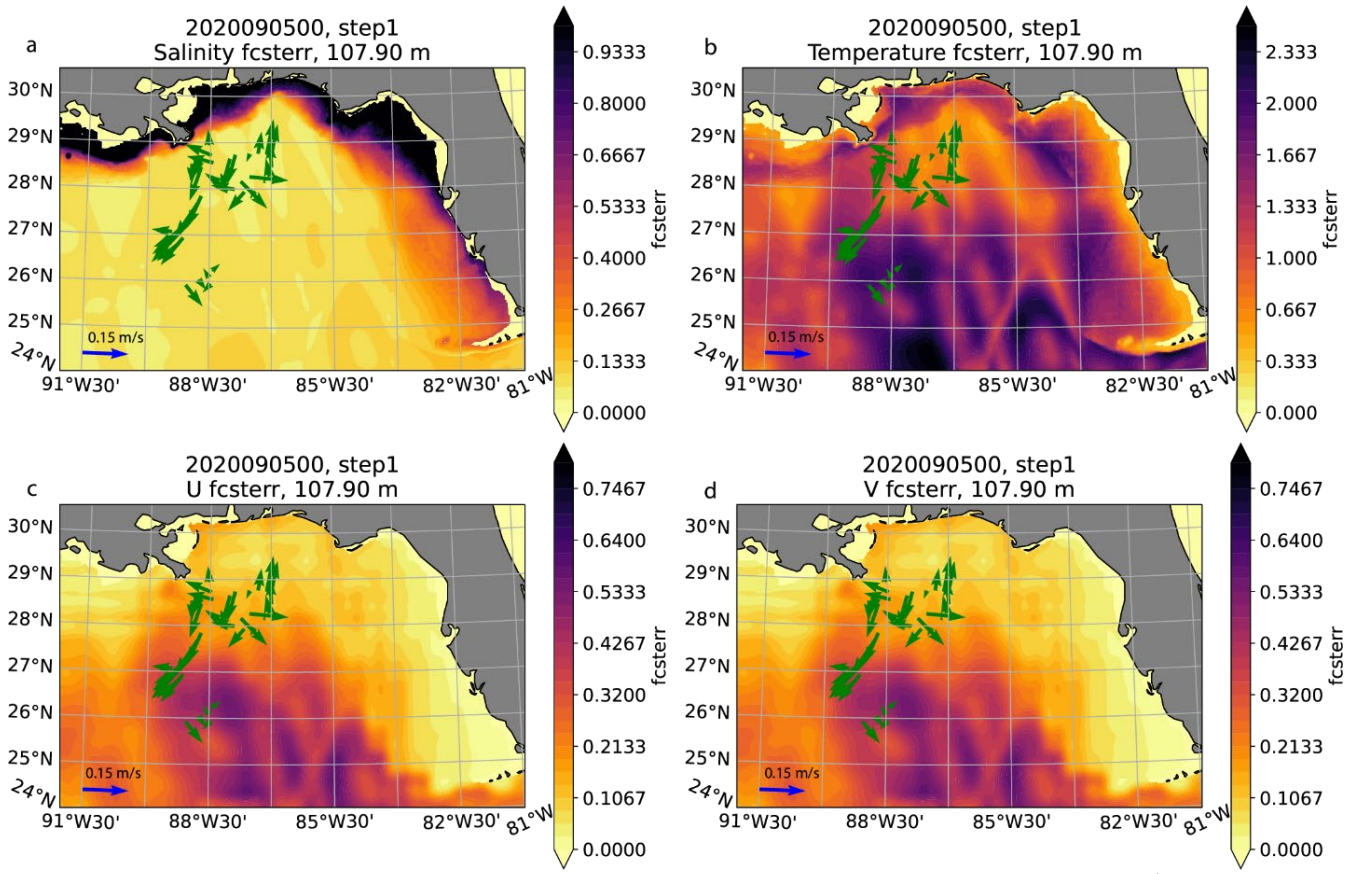

Figure 24. Forecast (background) error maps at 107.90 meters depth for (a) T in C, (b) S in psu, and (c) U and (d) V in m/s on September 5th. The black arrows overlaid are 24-hour super-observation Eulerian drifter velocity increment vectors assimilated on that day. The legend arrow in the upper right is for 0.25 m/s.

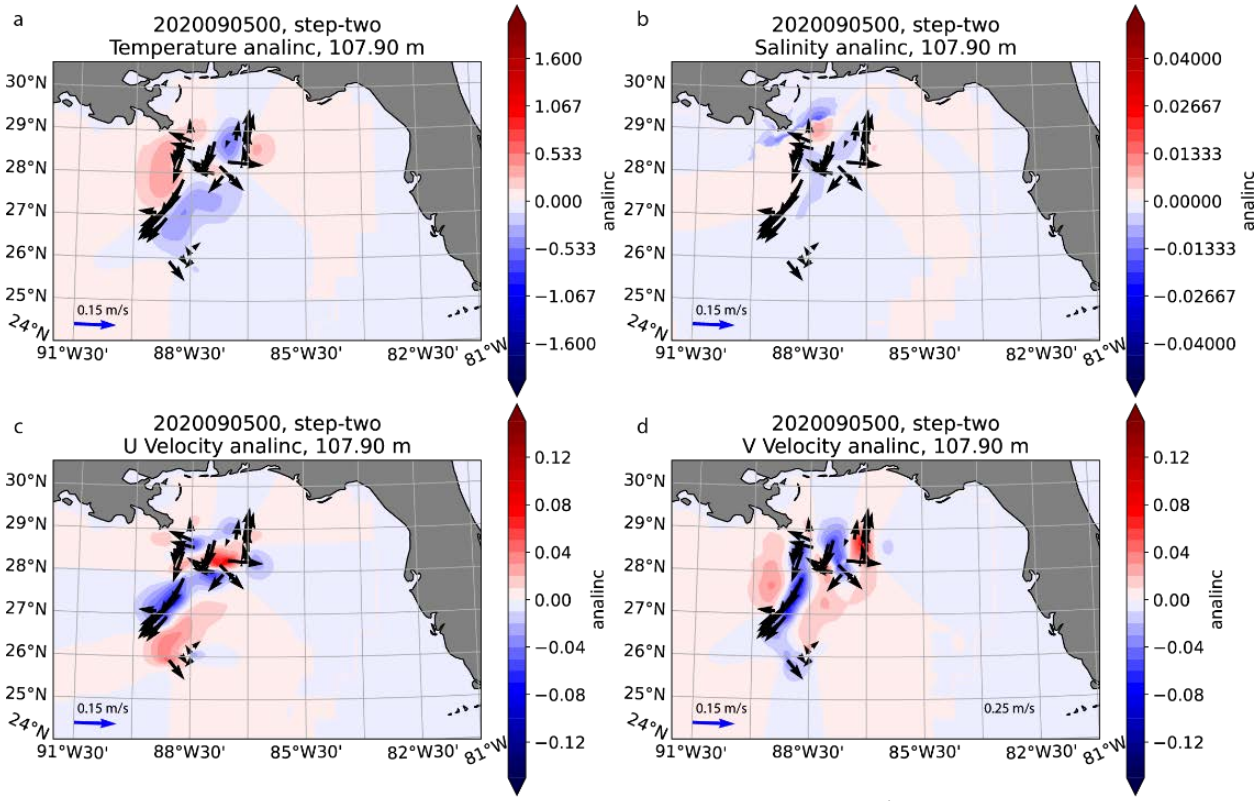

Figure 25. Increment maps at 107.90 meters depth for (a) T in C, (b) S in psu, and (c) U and (d) V in m/s on September 5th. The black arrows overlaid are 24-hour super-observation Eulerian drifter velocity innovation vectors assimilated on that day. The legend arrow in the upper right is for 0.15 m/s.

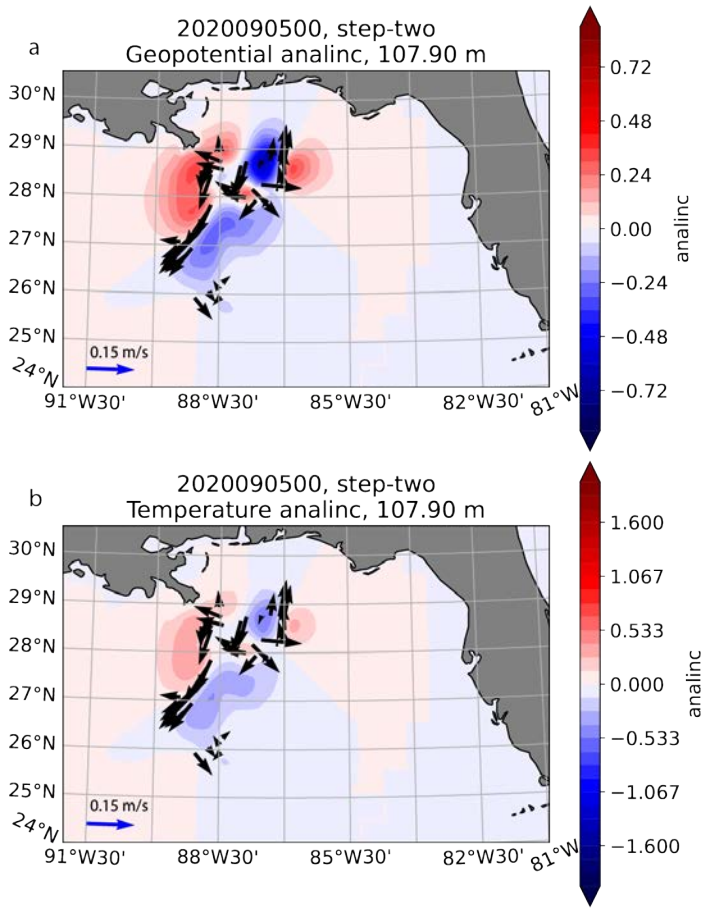

Figure 26. Increment maps at 107.90 meters depth for (a) G in m and (b) T in C on September 5th. The black arrows overlaid are 24-hour super-observation Eulerian drifter velocity innovation vectors assimilated on that day. The legend arrow in the upper right is for 0.15 m/s.

5.6 Forecast Validation Results

5.6.1 Qualitative Assessment of an Eddy Location

The comparison between the two experiments, CNTRL and TWO-STEP, are analyzed qualitatively by visually examining the position of an anticyclonic eddy in the NE portion of the Gulf of Mexico (28.4°N, 87.3°W on Aug 28). Figure 27 shows the position of this eddy with (TWO-STEP) and without (CNTRL) velocity data assimilation on Aug 28, 2020, when the drifter were first deployed, and 2 weeks later on Sep 10, 2020. The color contours in these plots is of temperature at 100 m depth, and the black dots represent the position of the drifters. The white tails trailing the black dots represent the drifters previous positions over several days, therefore, showing the direction that they are moving. On Aug 28, the solutions are very similar, especially the location of the anticyclonic eddy. No velocity observations were assimilated on this day, because there were no drifter positions on the previous day to compute velocity. The slight differences between the left panels of Figure 27 are due solely to the differences in the versions of NCODA that were used (section 2.2). The experiment with velocity DA was initiated on Aug 15 and used an updated 2-step version of NCODA that included an updated formulation to compute forecast errors. Therefore, the slight differences in the left panels are due to the accumulation of 2 weeks' worth of computing forecast errors differently.

After two weeks of assimilating inferred velocity observations from the drifters, on Sep 10, there is a clear difference in the position of the anticylonic eddy (right panels of figure 27). It can clearly be

seen that the velocity assimilation has repositioned the eddy to be in the correct position relative to the movement of the drifters. It can also be seen that the drifters to the west of the eddy are affecting the circulation in the region.

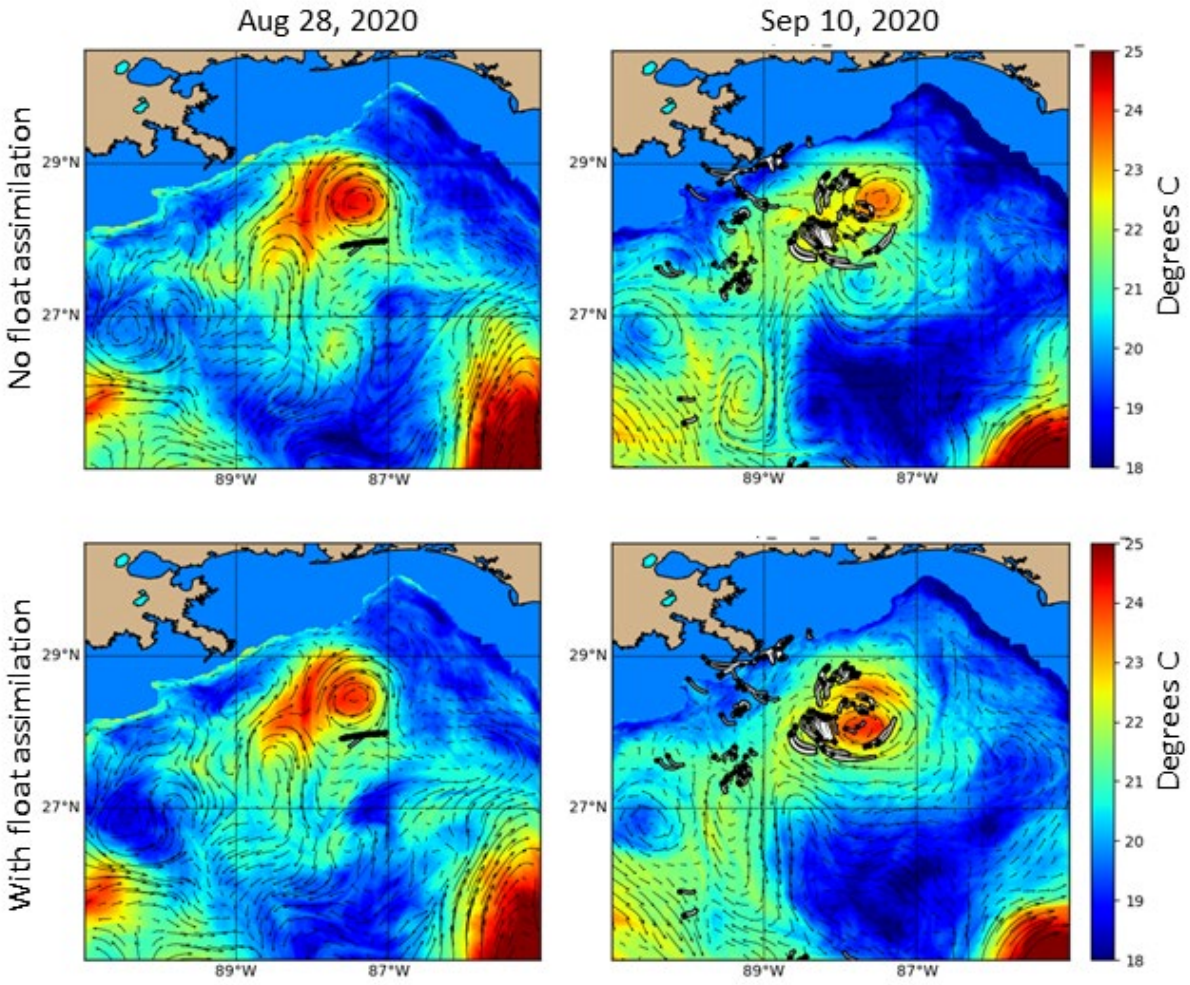

Figure 27. Comparison of the position of an anticyclonic eddy between the CNTRL experiment with no velocity assimilation (top row) and the TWO-STEP experiment with velocity assimilation (bottom row). The panels show temperature at 100 m depth for the NE quadrant of the Gulf of Mexico on Aug 28, 2020 (left column) and on Sep 10, 2020 (right column). The overlaid black dots are the positions of the drifters and the white tails are their previous positions for the past one day to represent their movement.

5.6.2 Error Analysis Relative to Unassimilated Glider Data

T and S profiles from two NOAA gliders were intentionally withheld from assimilation in either experiment. As can be seen in Figure 28, both gliders operated in the same vicinity and during the same time frame as the drifter deployment. NOAA glider SG601 collected data from Sep 6 to Dec 1, 2020, and NOAA glider NG357 collected data from Sep 6 to Sep 21, 2020. Figure 29 shows the average distance of the drifters from each of the gliders along with the number of drifters relative to time. The drifters used in these plots are the positions of the averaged velocities. The distance between drifters and glider increases for both gliders with time. Even though glider NG357 only collected data for 2 weeks, it is generally closer to the drifters and therefore may be more relevant in validating the experiments.

This figure also shows the tracks of two autonomous underwater buoyancy gliders (Rudnick, 2016) deployed during the same time period. We withheld the glider data from the assimilation for validation with independent data.

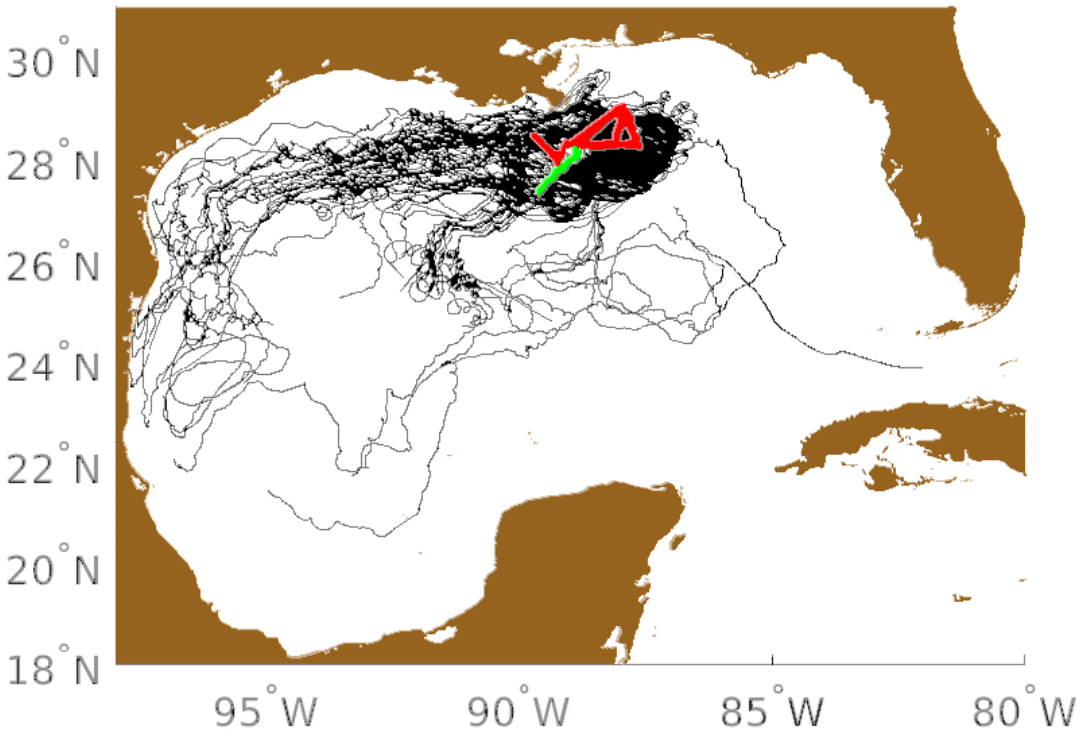

Figure 28: Map of the Gulf of Mexico where the experiments took place. Overlaid on the map are the tracks from 377 drifters that were deployed starting Aug 28,2020 and lasting till Dec 25, 2020 (black lines). The red and green lines show the tracks of NOAA gliders SG601 and NG357 respectively. The data from these gliders were not assimilated and used for independent evaluation.

The 0-24 hour forecast of temperature, salinity and velocity from the 2 experiments are used in the comparison with the T and S in situ profile observations from both gliders. Velocities are also compared, where the depth-averaged velocity provided by the glider operator is inferred from the displacement of the surfacing position of the glider from the predicted position based on the glider subsurface attitude and direction. The hourly forecasts are interpolated in time and space to each glider observation. The interpolated velocity fields are depth averaged over the depth of each glider dive. Table 3 shows a summary of the overall RMS differences of T, S, U and V between both experiments and both gliders. In addition, for glider SG601 we included the RMS differences for just the month of September, because after this month the distance between the glider and drifters becomes large and the influence that the drifter velocity assimilation has on the solution near the glider is expected to diminish (Figure 29). The results in this table show that overall the inclusion of velocity assimilation slightly reduces the T and S errors and drastically reduces the velocity error; at times by more than half.

Figures 30, 31, and 32 show the time series of the differences between the two experiments and the two gliders for T, S, and velocity respectively.

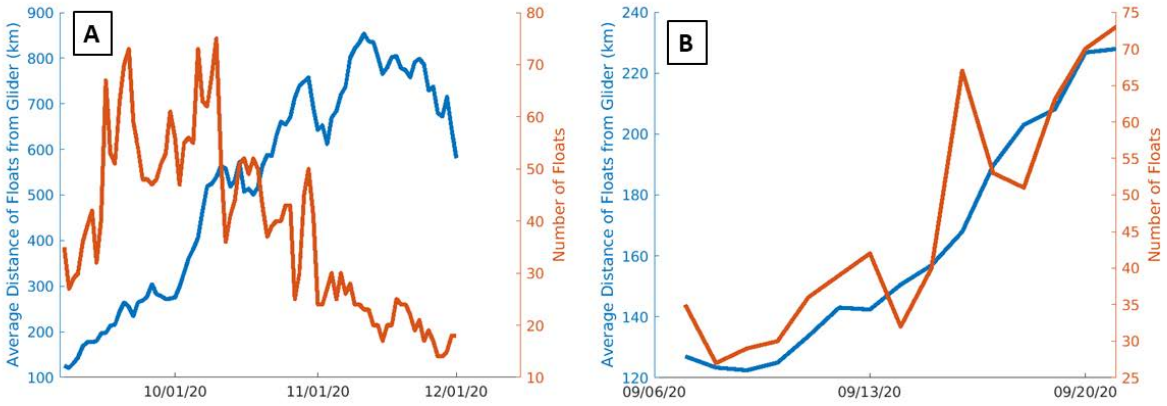

Figure 29. Average distance (blue line) of the drifters from glider SG601 (A) and glider NG357 (B) relative to time. Also shown is the filtered number of active drifters (orange line) relative to time.

Table 3. RMS errors of temperature, salinity, and velocity between the 2 experiments and the glider data, where the non-velocity DA experiment is labeled Exp1 and the experiment with velocity DA is labeled Exp2. There are 2 sets of RMS values for glider SG601; 1 for the entire time period of the glider (SG601-All) and the other just for the month of September (SG601-Sep). The lower RMS values are highlighted in green for easier comparison.

	Temperature (°C)	Salinity (PSU)	u velocity (m/s)	v velocity (m/s)
SG601 - All				
Exp1 - Glider	0.766	0.197	0.107	0.142
Exp2 - Glider	0.734	0.181	0.095	0.096
SG601 - Sep				
Exp1 - Glider	0.865	0.222	0.128	0.198
Exp2 - Glider	0.733	0.183	0.103	0.078
NG357 - All				
Exp1 - Glider	0.566	0.172	0.152	0.124
Exp2 - Glider	0.574	0.138	0.087	0.058

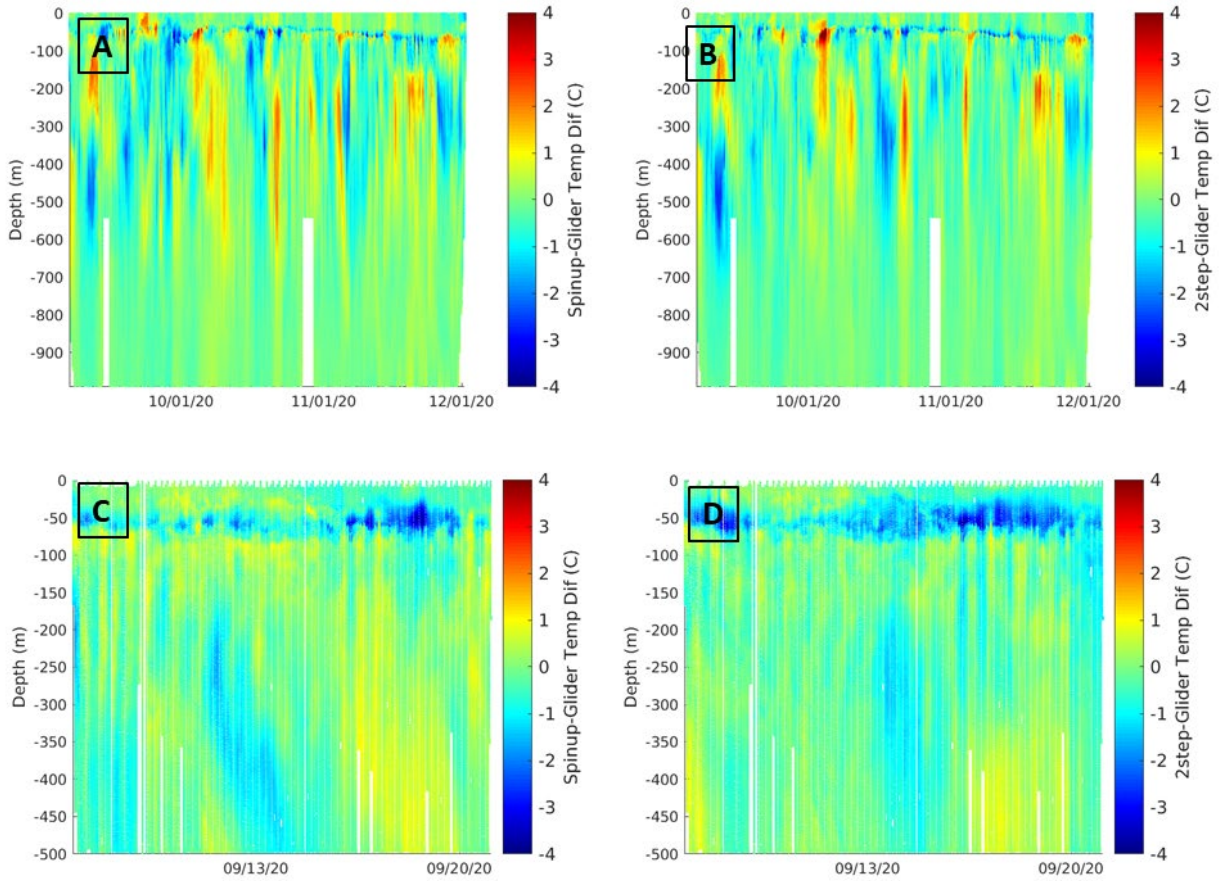

Figure 30. Temperature errors of Exp1 relative to gliders SG601 (A) and NG357 (C). Likewise for Exp2, the errors relative to gliders SG601 (B) and NG357 (D).

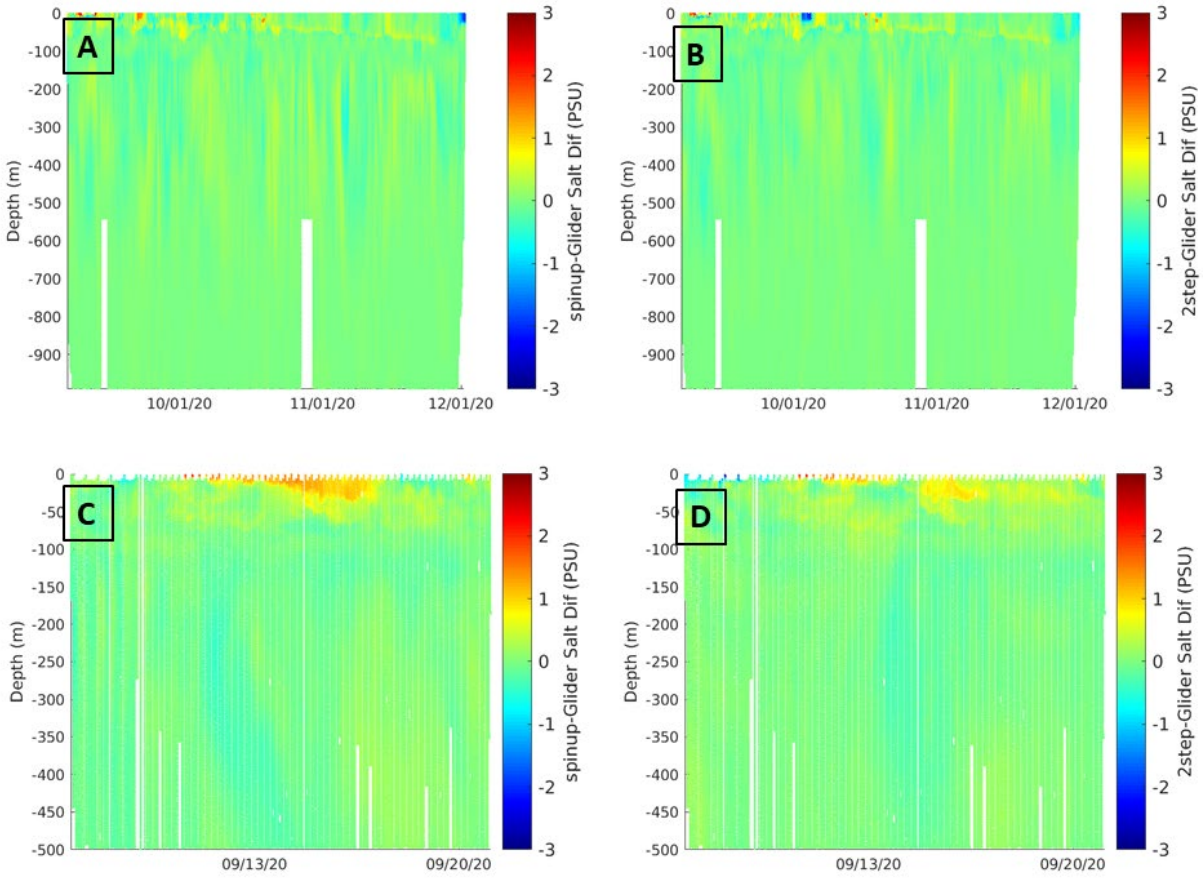

Figure 31. Similar to figure 13 but for salinity.

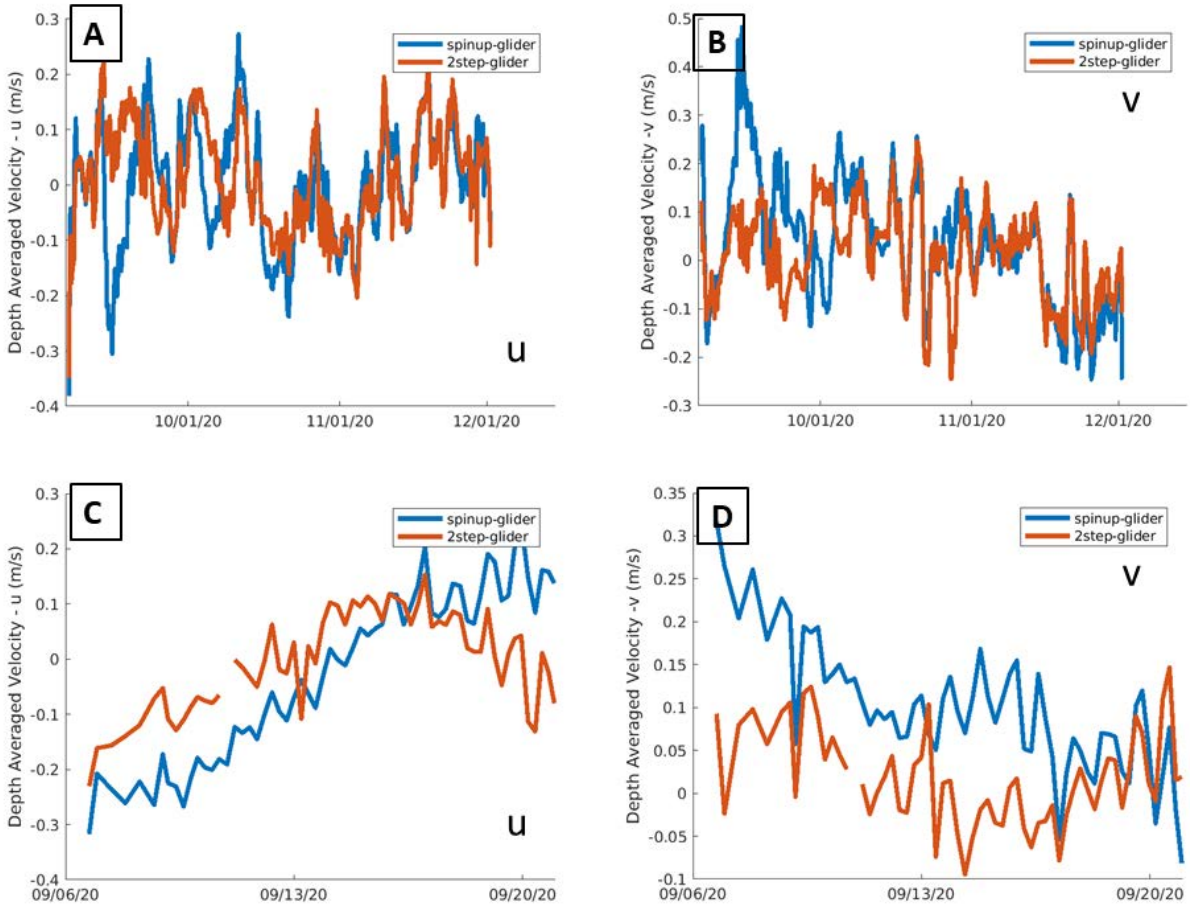

Figure 32. Depth averaged velocity differences between the 2 experiments and the 2 gliders. Panels (A) and (C) show the differences of the u component relative to gliders SG601 and NG357 respectively, and panels (B) and (D) show the differences of the v component relative to gliders SG601 and NG357 respectively.

5.6.3 Forecast Error Comparison of Temperature, Salinity, and Velocity

In this section, the errors of the 0-48 hour forecast fields of T, S, and velocity from the two experiments are examine and compared. These forecast field errors are relative to future observations that have not been assimilated yet, but many of the validating observations will likely be assimilated.

To evaluate the skill of the forecasted temperature and salinity values, we have acquired more than 2000 profiling float data (Figure 33) from the NOAA World Ocean Database (WOD). Figure 34 shows a map of the location of the observations at 200 m compared with the two-step forecast values at 200 m.

In this section, the errors of the 0-48 hour forecast fields of temperature, salinity, and velocity from the two experiments are examined and compared. The prediction skill of temperature and salinity is evaluated by comparing the forecasts from the two experiments with temperature and salinity observations from profiling floats in the NOAA World Ocean Database (WOD) available at the National Center for Environmental Information (NCEI; https://www.ncei.noaa.gov/). These profile observations are included in the data that is assimilated in the experiments; since we are examining the forecasts, however, we are comparing the model forecast at a time when the observed profiles have not yet influenced the system. Figure 33 shows the overall number of WOD profile observations with depth that are within the time period and region of the experiments. For ease of comparison, the observations were

binned into 10 m bins where the center of the first bin start at 10 m depth and extends every 10 m until 1900 m. Due to the sparseness of profile observations in the Gulf of Mexico during this time (about 2000), not all depth bins have data. The stars in Figure 33 denote the depth bins that have data.

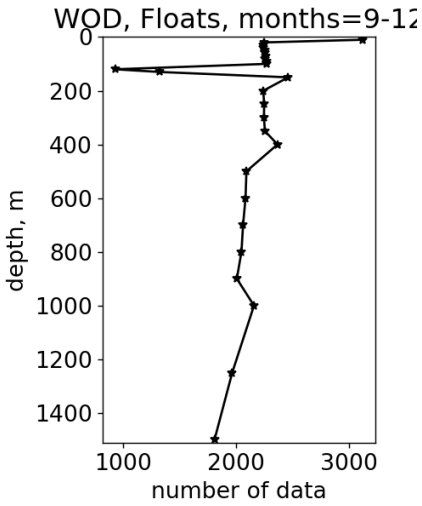

Figure 33. The number of profiles float data versus depth used in the forecast T and S validation. The * along the plotted line the depths where data exists at the center of 10 meter depth bins. See text below for more discussion on the validation methods.

Figure 8 shows a map of the location of the WOD observations at the 200 m depth bin for the month of October where the colors indicate the temperature difference between the observations and the 0-24 hour forecast fields from the CNTRL (left panel) and 2STEP (right panel) experiments. The 200 m depth bin was selected because this is about the depth of the thermocline, which is an important ocean feature to accurately predict, and examining the month of October gives the drifters a month to spread and cover more area. Examination of the resulting temperature differences in this figure reveal that differences appear to be less in the northeast region of the Gulf of Mexico where the drifters are, and larger in the southwest.

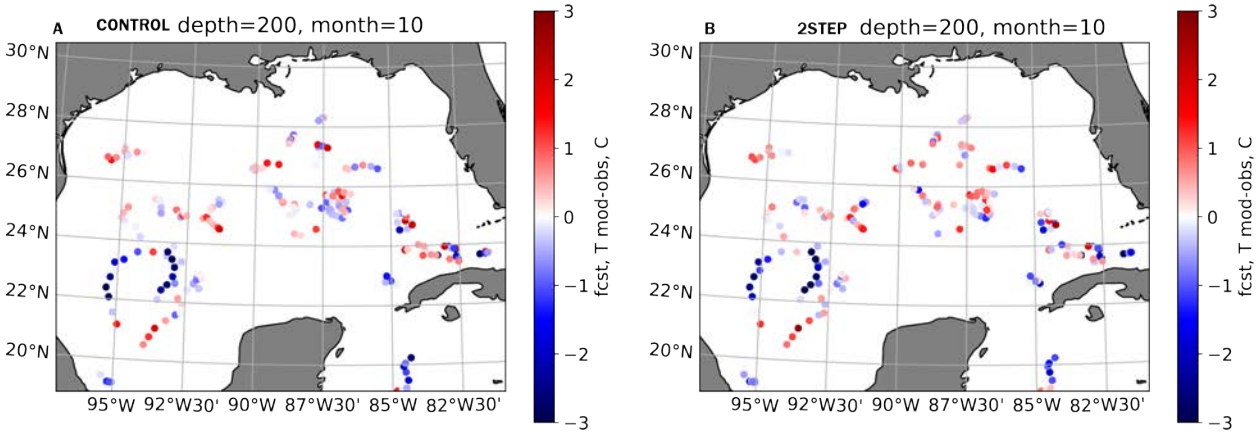

Figure 34. The location of all the WOD profile float observations at the 200 m depth bin for the month of October. The colors indicate temperature difference between the A) CNTRL and B) 2STEP 0-24 hour forecast and the observed values.

We perform comparisons with the forecast in two stages. Observation profiles are compared with the model forecasts from the 3 to the 24 hour taus and also with the 27 to 48 hour taus. For example, an

observation taken at 4:00 UT is compared with the 3 hour tau on that day and also the 27 hour tau. The forecast model only saves output every three hours. We also bin the observations into 10 meter bins, the center of the bins start at 10 meters depth and extend very 10 m until 1900 m. Not all depth bins have data.

For depth dependent error estimates, we compute the rout mean square (RMS), bias, and median absolute deviation (MAD) error are given by:

$$RMS = \left[\sum_{n=1}^{n} \left(y - x \right)^2 \right]^{1/2}, \tag{39}$$

$$bias = \frac{1}{n} \sum_{i=1}^{n} \left(y_i - x_i \right), \tag{40}$$

and

$$MAD = \text{median}\left[\left| \mathbf{y} - \mathbf{x} \right| \right]. \tag{41}$$

Here the vectors $\mathbf{x} = \left[x_1, x_2, x_3, \cdots x_n \right]$ and $y = \left[y_1, y_2, y_3, \cdots y_n \right]$ represent the model and observation values, respectively, for temperature or salinity within a single depth bin. The two model cases are the control run described above and the observations are the WOD float data. The RMS and bias measures are standard validation measure while the MAD represents a measure that is more robust is case of non-Gaussian data distribution, and is thus less influences by outliers.

The result of equations 1, 2, and 3, for temperature for each depth and the CNTRL and TWO-STEP cases is shown in Figure 35. Results are shown for both forecast stages as well. Except near the surface (less than approximately 200 m), the velocity data assimilation case, TWO-STEP, has greater accuracy, in terms of RMS, bias, and MAD errors. Since the MAD results are similar to those of the RMS, the distribution of the validation data are relatively Gaussian without many outlying data points. The bias results are considerably worse for the TWO-STEP case above approximately 150 meters. The results for salinity are shown in Figure 36. For salinity, the TWO-STEP case is even more accurate below 200 m to about 800 m in terms of RMS and MAD. The salinity bias for the TWO-STEP, however, is not better than the CNTRL case, except near the surface., in contrast with temperature bias, near the surface.

A comparison is made between the forecast errors and the gridded predicted forecast errors used in the 3DVAR analysis system. Figure 37 shows a two-dimensional histogram of the predicted temperature (A) and salinity (B) forecast errors using the 2STEP cycling system from September 1 until December 25. The green lines in Figure 37 is the RMS error, for the same time period, of the 0-24 hour forecast fields relative to the WOD data; which are the same lines as the solid red lines of the RMS plots of figures 35 and 36. We find that the predicted forecast errors in the 2STEP experiment tend to be slightly larger compared to the actual temperature forecast RMS errors. Whereas, the actual salinity forecast errors tend to line up more closely with the predicted forecast errors used in the system, except for at the surface. This suggests that for temperature, the forecast errors in the system could be reduced for potential improvement to the system.

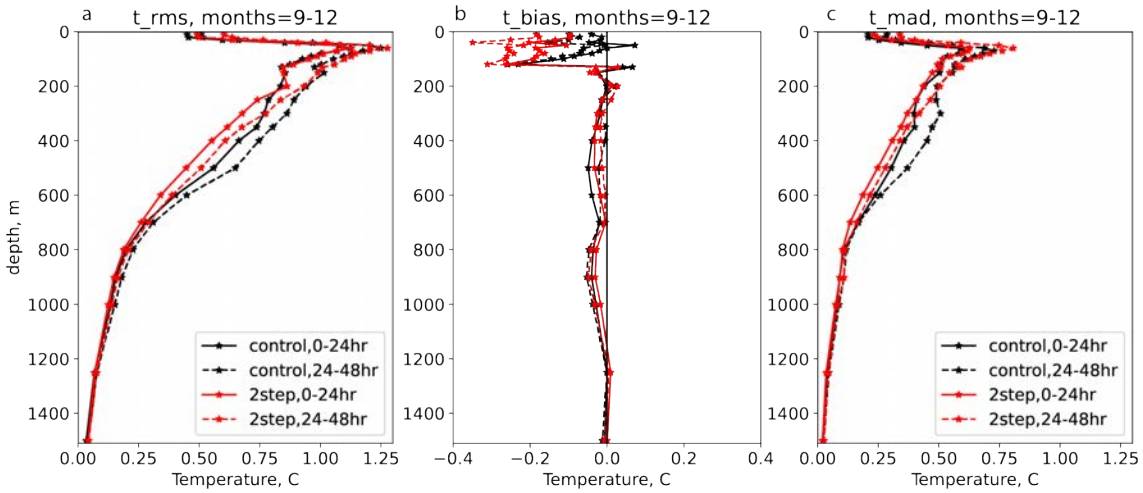

Figure 35. The statistical calculations of RMS, BIAS, and Median Absolut Deviation (MAD) for temperature versus depth for the control run and the two-step velocity data assimilation cases for the 3 to 24 and the 27 to 48 hour forecasts. The dots on each line indicate the depths where data exists at the center the 10 meter depth bins.

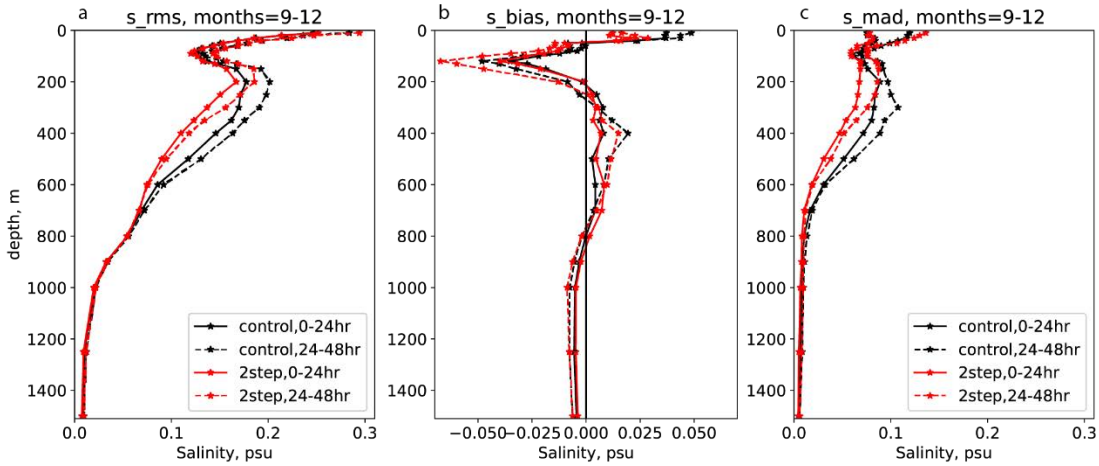

Figure 36. The statistical calculations of RMS, BIAS, and Median Absolut Deviation (MAD) for salinity versus depth for the control run and the two-step velocity data assimilation cases for the 3 to 24 and the 27 to 48 hour forecasts. The dots on each line indicate the depths where data exists at the center the 10 meter depth bins.

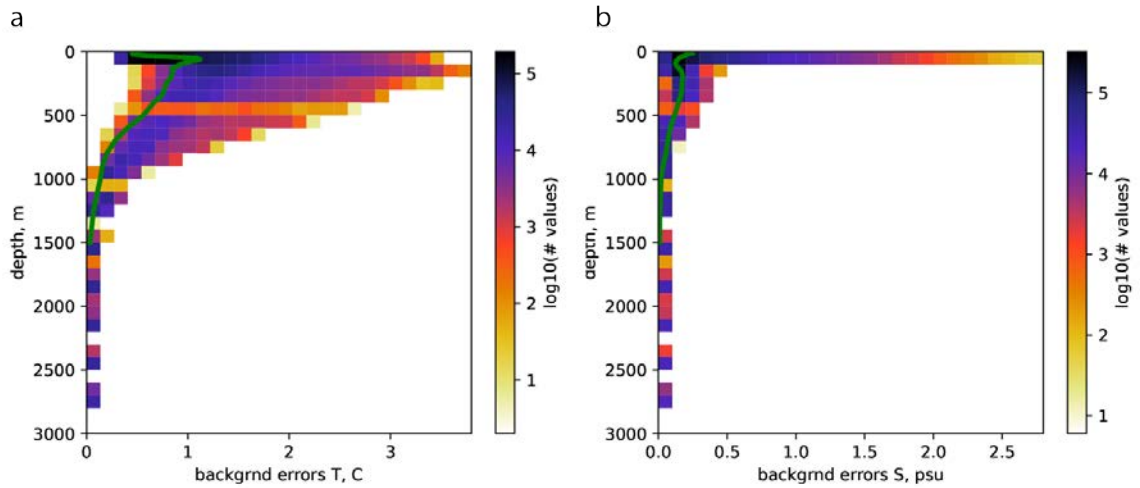

Figure 37. a) Temperature and b) salinity forecast error 2D histograms versus depth, evaluated at the location of assimilated observations from September 1 through December 25. The green line is the forecast error from the 2STEP test case relative to the WOD profiling float observations during the same time period. Note that the colorbar is on a logarithmic scale.

Figure 37 examines the velocity forecast error, where Figure 38A shows a polar histogram of the velocity error of the CNTRL experiment relative to the inferred drifter velocities. To compute the polar histogram, the magnitude of the velocity error determined the distance from center, and the direction of the error determines the angle from the line from the center to the top of the plot. Thus, small errors in magnitude cluster toward the center, and small errors in direction cluster toward the line from the center toward the top. Similarly, Figure 38B shows the error distribution for the 2STEP experiment. Note that the colorscale on Figures 38A and B are logarithmic, where the counts in each bin have been normalized by the total number of counts and by the area of each bin from August 28 to October 10. The counts include all inferred drifter velocities and not just the filtered ones that were assimilated. For each drifter velocity, the 0-24 hour model forecast fields were interpolated in space and time to the observed velocity. The more red the bin color is towards the center (magnitude error) and the 0° line toward the top of the panel (directional error), the better the model forecast is matching the observed velocities. The case with velocity data assimilation (2STEP; Figure 38B) has red near the center and on the 0º line, indicating a more skillful result for velocity data assimilation.

To make the difference between the two experiments more apparent, Figure 38C shows the direct difference between Figures 38B and 38A. In Figure 38C, bins that are red (blue) indicate that 2STEP has a higher (lower) count in the bin. As can be seen, the redder bins are in the more accurate portion of the polar plot, which signifies that the 2STEP is outperforming the CNTRL run. Figure 38d shows the distributions of the observed speeds and of the velocity magnitude of the error for the experiments. The distribution of observed velocity indicates typical 0.2 to 0.4 m/s speeds with a long distribution toward higher speeds. Both experiments show error distributions with concentrations containing errors at lower magnitudes than the distribution of observed speeds, which demonstrates both experiments have skill. 2STEP (solid black line) shows lower counts in the 0.15 – 0.5 m/s error bins and higher counts in the 0.0 – 0.1 m/s bins relative to CNTRL (dashed black line), demonstrating an overall reduction of velocity magnitude forecast error when velocities are included in the assimilation.

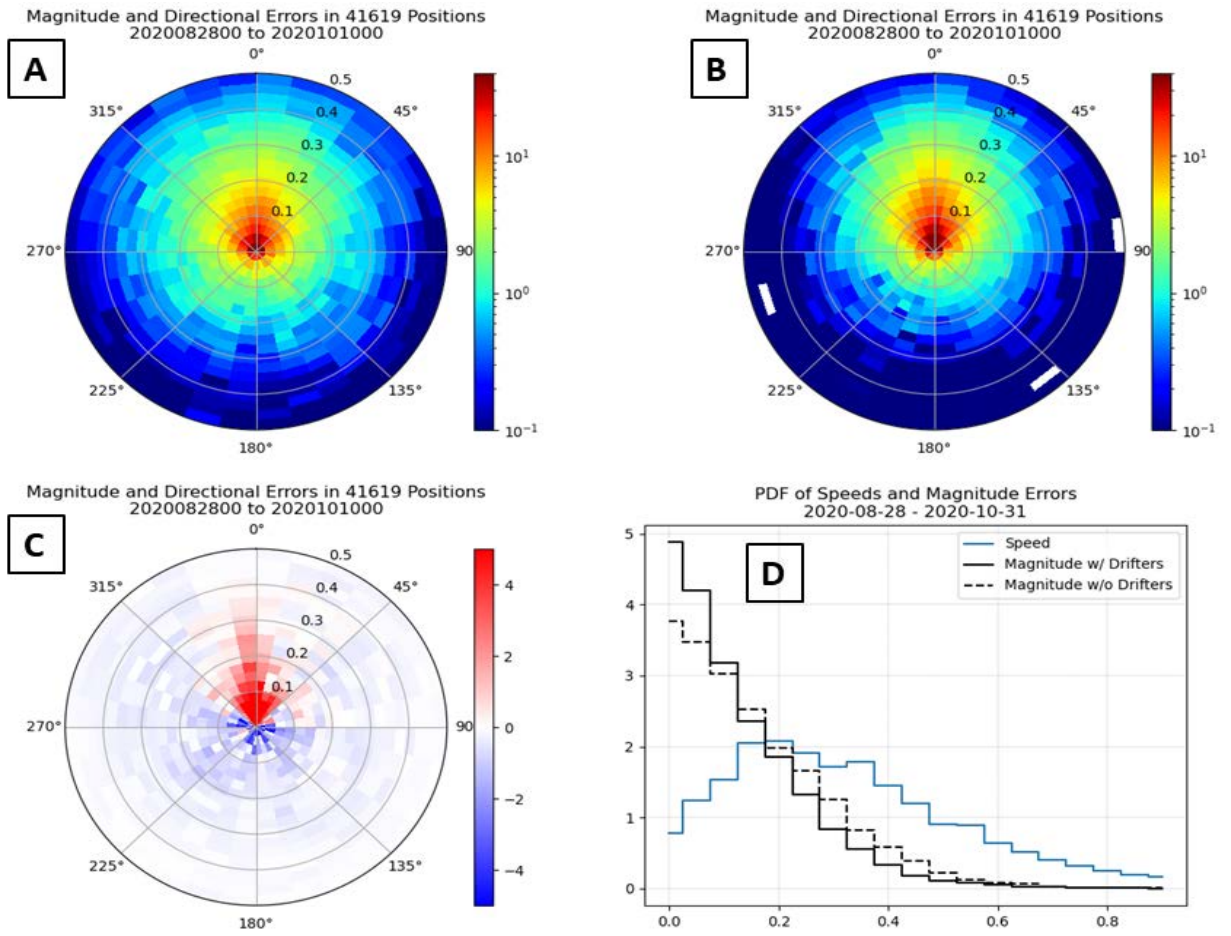

Figure 38. Polar histogram difference plots between velocity vectors from model forecasts and the inferred drifter velocities. Panels (A) and (B) show the error distributions of the CNTRL and 2STEP experiments respectively relative to observations. These histograms span the results from August 28 to October 10. The error in direction is the angle from the line pointing up from center, and the magnitude error is distance from the center. The labels on the circles are in terms of m/s. Panel (C) is the difference between panels (B) and (A). Note that the colorbar on panel (C) is linear, whereas it is on a log10 scale in panels (A) and (B). Panel (D) shows the distributions of the observed speeds (blue line) and of the velocity magnitude error for CNTRL (dashed black line) and 2STEP (solid black line).

5.6.4 Lagrangian Displacement Errors

Numerical Lagragian drifter trajectories can be a very valuable tool in analyzing the skill of a prediction system (van Sebille et. al. 2009, Liu and Weisberg 2011, and Barron et. al. 2007). In this section, we examine simulated Lagrangian trajectories created by seeding tracers into the experiment's forecast fields at the drifter locations, and propagating these positions using the forecasted velocity fields. For this analysis, we filtered the drifter data set and removed the drifters that lasted less than days and those that had a large gap between recorded positions. We started the analysis on Sep 1, 2020 with 180 drifters (the number of drifters drop off gradually until there's none by around Dec 15, 2020). Each experiment was seeded with the drifter positions on each day from Sep 1 to Dec 10, 2020. Trajectories were then created by propagating these positions through the experiments' hourly velocity forecast fields for 5 days using software (Barron et. al., 2007). This process created 101 different 5-day forecasts for each drifter and each of the two experiments. Figure 39a shows the RMS separation distance between the drifter locations and the model's predicted drifter locations of all the forecasts. All told, each hourly tau

on the x-axis contains thousands of individual separation distances in the RMS calculation. The separation distance is zero at the beginning, since the model drifter positions start off at the same locations as the actual drifters. This separation distance increases to about 105 km after 5 days in the experiment without velocity DA, and about 80 km in the experiment with velocity DA.

The model results from both experiments were passed through a filter that separated the velocity fields into constrained and unconstrained components, following the methods described in the "Ocean Confidence" VTR (Jacobs et al. 2022). When the model solution is unfiltered, small scale, potentially inaccurate, features are retained in the solution. In this case, the RMS difference between observations and the model solution is relatively large. Using the Ocean Confidence methods, an optimal filter is designed to retain only the constrained scales of variability, and is thus more accurate. Figure 39b was created in a similar fashion as figure 39a, except that the separation distances used just the constrained component of the velocity fields. The overall separation distance is reduced for both experiments when the drifter tracks are compared with just the constrained component of the velocity fields. It is interesting to note that the case with filtered/constrained case has a more significant reduction compared to unfiltered/unconstrained case.

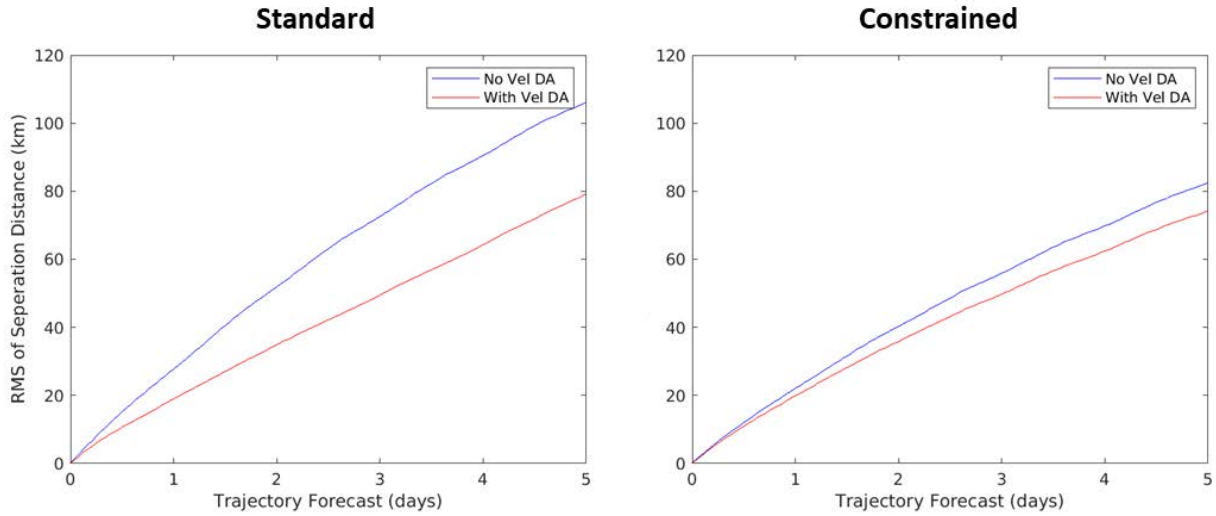

Figure 39. (a) RMS of the separation distance between the drifters and 5-day Lagrangian trajectories from the non-velocity DA experiment (blue line) and the experiment with velocity DA (red line). (b) Similar to panel (a) except comparison is made with the constrained component of the filtered forecasted velocities.

6. CONCLUSIONS

In this manuscript, we describe the updates made to the Navy's operational forecasting system COAMPS in order to assimilate velocity observations inferred from the movement of surface drifters. The operational version of COAMPS uses 3DVAR (NCODA) for the ocean data assimilation and NCOM for the forecast. The upgrades made to COAMPS were primarily with the NCODA system and they include: adding software to process drifter observations and infer their velocities, splitting the analysis into 2 steps assimilating temperature and salinity in the first step and velocity in the second, and calculating velocity forecast errors. In order to assimilate velocities in the second step, a covariance model was created (derived from historical *in situ* observations) to relate velocity innovations to changes in T and S.

The following summary of conclusions for the methods evaluation and the 2020 Gulf of Mexico validation experiment are adapted from that in the Ocean Modelling research articles.

Conclusion of Methods Evaluation (Helber et al. 2022):

In this report, we describe a method to assimilate velocity observations inferred from the movement of surface drifters. The assimilation approach is in two steps, each step performs a 3DVAR analysis creating increments for the purpose of correcting a numerical forecast model. The increments from each step are added together to create a single set of increments for data assimilation. The reasons for performing velocity data assimilation in two steps are due to convergence issues when velocity observations occur near T and S observations and because the new vertical covariances required for velocity data assimilation are not yet compatible with the Navy's existing 3DVAR data assimilation system. The first assimilation step (step-one) performs a traditional assimilation of observations of T, S and SSHA. The covariances in step-one relate the T and S innovations to velocity through geostrophic coupling to create velocity increments in addition to T and S increments. The second 3DVAR analysis (step-two) performs data assimilation ingesting velocity vector innovations that are related, through the correlation model, back to create increments of T and S, in addition to velocity innovations.

Key aspects of the system stem from the need to project velocity information over the water column. Many in situ velocity observations are made at a single depth, as in the case of this analysis, which is done using surface drifters. Correcting velocity only at one depth in a forecast model would not produce good results because increments need to have a dynamical balance so as to not shock the numerical model into a dynamically unbalance state. In order to provide the relationship of velocity over the entire water column, the vertical correlations and the vertical error variance (separately) are an important aspect of the system, which we have been upgraded, compared to an existing data assimilation system. In particular, the 3DVAR equation has been adjusted to apply forecast error variance over the whole water column and the vertical correlations are altered to have empirically derived vertical correlations created from historic in situ profile observations.

Another important aspect of the two-step system is the processing of forecast errors. Forecast errors are updated after step-one. This is done to account for the skill of the analysis from step-one, which reduces the forecast error in the vicinity of the observations. For the step-two 3DVAR analysis we used the vertical covariances to estimate the velocity forecast errors from the T an S forecast errors. Thus, the velocity forecast errors are consistent with the dynamical balances created from the new vertical covariances.

Because the vertical covariances are derived from in situ observations that can only resolve the mesoscale structure, the entire system is a mesoscale data assimilation system. For this reason, the dynamical balance of the covariance model is strictly geostrophic coupling. Also, the velocity obversions are filtered to represent geostrophic velocities. As a result, the velocity observations are computed via super-observation representing the diurnal time-scale.

The results presented section 5.5, examine the different components of the analysis system: innovation, increments, and errors. These were solely diagnostic, in order to ensure that the updated two-step analysis was working properly. This analysis system is capable of assimilating velocity observations

inferred from surface drifters, and the results presented in this report show analysis increments that consistently and accurately correct the background towards the in situ observations. In section 5.6 the two-step system is compared with a twin experiment, one without velocity assimilation, to show that the corrections provided by the new system do improve the forecast of T and S as well as velocity.

Conclusions regarding the 2020 Gulf of Mexico validation experiment (Smith et al 2022):

In section 5.6 we present several different types of validation results show improvement in the forecast skill with the assimilation of inferred velocity observations. The first set of validation results was a qualitative assessment. The position of an anticyclonic eddy was examined in the region where the drifters were deployed. By comparing the 100m temperature field from the two experiments, it is obvious that the added velocity data assimilation was able to reposition the anticyclonic eddy to the correct position. The second set of results compared the 0-24 hour forecast fields of temperature, salinity and velocity from the two experiments with un-assimilated observations from a pair of independent gliders. These results show that adding velocity data assimilation to the analysis improved the accuracy of temperature and salinity, and reduced the velocity error. The third set of results compared the forecast fields with future observations that had not yet been assimilated. These results show a reduction in temperature and salinity profile error when velocity data assimilation is included, especially below the mixed layer and for salinity. The polar plots for velocity error show an improvement when velocity observations are added to the analysis, especially with the direction of the velocity vectors. The final set of results is a comparison of the forecast velocity fields in a Lagragian sense. In this analysis, simulated drifters were injected into each experiment at the actual drifter locations and advected using the experiment velocity fields. These paths were compared with the observed drifter paths, and the resulting RMS separation distances from this analysis show that adding velocity assimilation improves the prediction of velocity in a Lagrangian sense too.

In conclusion, we find the relatively inexpensive surface drifters have positive impact on the surface velocity forecast. In addition, when the proper use of the surface velocity is implemented then the subsurface temperature and salinity are also positively impacted. It has been demonstrated that the updated assimilation system is capable of assimilating velocity observations inferred from surface drifters, and that their inclusion benefits forecasting velocity, temperature, and salinity.

ACKNOWLEDGEMENTS

This research is funded by the DARPA program Ocean of Things and is approved for public release. This document was cleared by DARPA on March 28, 2022 [DISTAR case 35970]. The views, opinions and/or findings expressed are those of the author and should not be interpreted as representing the official views or policies of the Department of Defense or the U.S. Government. The glider data used in this study are available at https://gliders.ioos.us/erddap/tabledap/SG601-20200906T1631.html. The authors would also like to thank Joseph D'Addezio, Innocent Souopgui, and Pete Spence, and Vivian Montiforte at the Naval Research Laboratory for fruitful discussions and collaboration regarding data assimilation and the research contained in this report.

APPENDIXES

Appendix A: Variable Description

Table A. The name, size, and description of the variables used in the 3DVAR analysis equations, where n is the number of analysis grid points times the number of variables and k is the number of observations. The n_z is the number of depth levels in the vertical covariance database. The symbols $\in \mathbb{R}^D$ under the "Size" column indicate the variable is a scalar, vector, or matrix of real numbers with dimension D and $\in \mathbb{R}$ is a scalar.

Variable	Size	description
x, x'	$\in \mathbb{R}$	zonal coordinate values
y, y'	$\in \mathbb{R}$	merdional coordinate values
z, z'	$\in \mathbb{R}$	depth, vertical coordinate values
T	$\in \mathbb{R}$	ocean water temperature in ^{o}C
S	$\in \mathbb{R}$	ocean water salinity psu
U	$\in \mathbb{R}$	ocean water velocity, eastward
V	$\in \mathbb{R}$	ocean water velocity, northward
G	$\in \mathbb{R}$	ocean geopotential meter
g	$\in \mathbb{R}$	gravity
f	$\in \mathbb{R}$	Coriolis parameter
σ	$\in \mathbb{R}^5$	vector of observation standard deviations for T,S,G,U, and V
w	$\in \mathbb{R}$	a weighting parameter
$\mathbf{x}_a$	$\in \mathbb{R}^n$	analysis field vector
$\mathbf{x}_b$	$\in \mathbb{R}^n$	background field vector
$\mathbf{x}_{err}$	$\in \mathbb{R}^n$	background error field vector
$\mathbf{x}_{a1}$	$\in \mathbb{R}^n$	analysis field vector, step-one
$\mathbf{x}_{a2}$	$\in \mathbb{R}^n$	analysis field vector, step-two
$\mathbf{x}_{b1}$	$\in \mathbb{R}^n$	background field vector, step-one
$\mathbf{x}_{b2}$	$\in \mathbb{R}^n$	background field vector, step-two
$\mathbf{x}_{err1}$	$\in \mathbb{R}^n$	background error field vector, step-one
$\mathbf{x}_{err2}$	$\in \mathbb{R}^n$	background error field vector, step-two
$\delta\mathbf{x}_1$	$\in \mathbb{R}^n$	analysis increment field vector, step-one
$\delta\mathbf{x}_2$	$\in \mathbb{R}^n$	analysis increment field vector, step-two
$\delta\mathbf{x}$	$\in \mathbb{R}^n$	analysis increment field vector
$\mathbf{B}$	$\in \mathbb{R}^{nxn}$	background error covariance matrix, between grid locations
$\mathbf{B}_{obs}^{grd}$	$\in \mathbb{R}^{nxk}$	background error covariance matrix, between observation and analysis grid locations
$\mathbf{B}_{grd}^{obs}$	$\in \mathbb{R}^{kxn}$	background error covariance matrix, between observation and analysis grid locations
$\mathbf{B}_{obs}^{obs}$	$\in \mathbb{R}^{kxk}$	background error covariance matrix, at observation locations

$\tilde{\mathbf{B}}_{ts}$, $\tilde{\mathbf{B}}_{uv}$	$\in \mathbb{R}^{2n_z x 2n_z}$	background error vertical covariance matrix. Subscripts "ts" are for T and S data and "uv" if for velocity data.
$\tilde{\mathbf{B}}_{tsg}$	$\in \mathbb{R}^{3n_z x 3n_z}$	subscripts "tsg" is for T, S, and G data
Γ	$\in \mathbb{R}^{2n_z x 6}$	column wise the six leading EOF modes of the vertical covariances
$\tilde{\mathbf{U}}_{ts}$	$\in \mathbb{R}^{2n_z x 2n_z}$	the diagonal standard T/S deviation matrix from empirical covariance database
$\mathbf{U}_{ts}$	$\in \mathbb{R}^{2n_z x 2n_z}$	the diagonal background standard deviation matrix
$\mathbf{\Lambda}$	$\in \mathbb{R}^{6x6}$	diagonal matrix of ISOP eigenvalues
$\mathbf{G}$	$\in \mathbb{R}^{n_z x 2n_z}$	performs the computation of geopotential height from specific volume
$\boldsymbol{\alpha}$	$\in \mathbb{R}^{2n_z x 2n_z}$	a matrix that converts T and S into specific volume
$\mathbf{L}$	$\in \mathbb{R}^{n_z x 2n_z}$	the linear operator that performs the computation of geopotential height from T and S variance
C	$\in \mathbb{R}$	correlation function between two locations separated in horizontal, vertical and flow dependent
$c\Big\|_{obs}^{grd}$	$\in \mathbb{R}^{nxk}$	Step-one Correlations as function of distance at observation and analysis grid locations
$c\Big\|_{obs}^{obs}$	$\in \mathbb{R}^{kxk}$	Step-one Correlations as function of distance at between observation locations
$\tilde{C}$	$\in \mathbb{R}$	step-two correlation function between two locations separated in horizontal, $\tilde{C}_v$ vertical, and flow dependent
$\tilde{C}\Big\|_{obs}^{grd}$	$\in \mathbb{R}^{nxk}$	Step-Two Correlations as function of distance at observation and analysis grid locations
$\tilde{C}\Big\|_{obs}^{obs}$	$\in \mathbb{R}^{kxk}$	Step-Two Correlations as function of distance between observation locations
C_h	$\in \mathbb{R}$	horizontal correlation function between two locations
C_v	$\in \mathbb{R}$	vertical correlation function between two depths, Gaussian dependence on the density gradient
C_f	$\in \mathbb{R}$	flow dependent correlation function between two locations
$\tilde{C}_v$	$\in \mathbb{R}$	vertical correlation function between two depths, empirically derived from historical observations
L_h, L_h'	$\in \mathbb{R}$	horizontal length scales
L_v, L_v'	$\in \mathbb{R}$	vertical length scales
s, s'	$\in \mathbb{R}$	great circle distances
$\mathbf{V}$	$\in \mathbb{R}^{nxn}$	diagonal background error variance matrix
$\mathbf{V}_{obs}$	$\in \mathbb{R}^{kxk}$	diagonal background error variance matrix, at observation locations
$\mathbf{V}_{grd}$	$\in \mathbb{R}^{nxn}$	diagonal background error variance matrix, at analysis grid locations
$\mathbf{V}^{inc}$	$\in \mathbb{R}^{nxn}$	diagonal background error variance matrix, estimated from history of increments
$\mathbf{V}_{anal}$	$\in \mathbb{R}^{nxn}$	background error analysis, values between 0 and 1
$\mathbf{x}_i^{fcst}$	$\in \mathbb{R}^n$	the i-th prior forecast
Δt_{fcst}	$\in \mathbb{R}$	the forecast relaxation timescale in days

Δt_{update}	$\in \mathbb{R}$	the assimilation update cycle in hours
w_i	$\in \mathbb{R}$	the i-th weighting value, use twice
$\mathbf{H}$	$\in \mathbb{R}^{kxn}$	matrix projecting observation space of k values onto the model space of n values (vice versa: $\mathbf{H}^T$, $\in \mathbb{R}^{nxk}$)
$\mathbf{R}$	$\in \mathbb{R}^{kxk}$	observation error variance, which is assumed to be diagonal
$\mathbf{y}_1$	$\in \mathbb{R}^k$	observation vector, T and S data, step-one
$\mathbf{y}_2$	$\in \mathbb{R}^k$	observation vector, u and v Eulerian velocity data, step-two
$\mathbf{y}_{err1}$	$\in \mathbb{R}^k$	observation error vector, T and S errors, step-one
$\mathbf{y}_{err2}$	$\in \mathbb{R}^k$	observation error vector, u and v velocity errors, step-two
$\delta\mathbf{y}_1$	$\in \mathbb{R}^k$	innovation vector, step-one
$\delta\mathbf{y}_2$	$\in \mathbb{R}^k$	innovation vector, step-two

Appendix B: Vertical Covariances from Historical in situ Observations

Equation 18 in the text is the background vertical error covariance matrix of size $\left(2n_z, 2n_z\right)$

$$\tilde{\mathbf{B}}_{ts,ts} = \tilde{\mathbf{U}}_{ts}\boldsymbol{\Gamma}\boldsymbol{\Lambda}\boldsymbol{\Gamma}^T\tilde{\mathbf{U}}_{ts} \tag{B1}$$

where n_z is the number of depth levels. This is the vertical error covariance matrix originally constructed for ISOP1 and briefly described in Helber et al. (2013). The diagonal standard deviation matrix in B1 is

$$\tilde{\mathbf{U}}_{ts} = \mathrm{diag}\left(\tilde{\mathbf{B}}_{ts}\right) = \left[\begin{array}{cccccccc} \mathrm{var}\left\{\tilde{\mathbf{T}}_1\right\}^{1/2} & \mathrm{var}\left\{\tilde{\mathbf{T}}_2\right\}^{1/2} & \cdots & \mathrm{var}\left\{\tilde{\mathbf{T}}_{nz}\right\}^{1/2} & \mathrm{var}\left\{\tilde{\mathbf{S}}_1\right\}^{1/2} & \mathrm{var}\left\{\tilde{\mathbf{S}}_2\right\}^{1/2} & \cdots & \mathrm{var}\left\{\tilde{\mathbf{S}}_{n_z}\right\}^{1/2} \end{array}\right] \tag{B2}$$

and at the center of B1 is the correlation matrix

$$\tilde{\mathbf{C}}_{ts} = \boldsymbol{\Gamma}\boldsymbol{\Lambda}\boldsymbol{\Gamma}^T \tag{B3}$$

where the diagonal eigenvalue matrix is $\boldsymbol{\Lambda}$ of size $\left(m,m\right)$, where m is the number of EOF modes and the eigenvectors are in the matrix $\boldsymbol{\Gamma}$ of size $\left(2n_z, m\right)$. The formulation error covariance is commonly used at is Kalnay (2003) section 5.4.1, for example. In the parlance of statistics or machine learning, variance is $\mathrm{var}\left\{\mathbf{x}\right\} = E_{P(\mathbf{x})}\left\{\left(\mathbf{x} - E_{P(\mathbf{x})}\left\{\mathbf{x}\right\}\right)^2\right\}$, where $E_{P(\mathbf{x})}\left\{\mathbf{x}\right\}$ is the expectation of the variable, $\mathbf{x}$ (e.g. Rogers and Girolami 2017). The decomposition of the correlation in B3, however, is a necessity that stems from deriving the error covariance from historical in situ observations.

Because the ocean varies in depth and historically available in situ profiles observations vary in depth sampling. The observations of T and S at each depth level k, are vectors, $\tilde{\mathbf{T}}_k$ and $\tilde{\mathbf{S}}_k$, that each have a different number of values. These types of data set in present NRL software are contained in two dimensional matrixes of size $\left(n_z, \max\left(n_k\right)\right)$ or "ragged arrays" with many missing values, where n_k is the number of observations at depth k. The $\max\left(n_k\right)$ value is usually near the surface. In addition, each observation profile is a different horizontal location. The first version of ISOP has a different $\tilde{\mathbf{B}}_{ts}$ at each ½ degree location on a regular global grid. Using a profile selection criterion, each $\tilde{\mathbf{B}}_{ts}$ is constructed from all available in situ observations. Thus, at a given location the observation vectors each have a different length and distance from the analysis location. At depth k, we have

$$\tilde{\mathbf{T}}_k = \left[\begin{array}{cccc} \tilde{T}_k^{(1)} & \tilde{T}_k^{(2)} & \cdots & \tilde{T}_k^{(n_k)} \end{array}\right] \text{ and } \tilde{\mathbf{S}}_k = \left[\begin{array}{cccc} \tilde{S}_k^{(1)} & \tilde{S}_k^{(2)} & \cdots & \tilde{S}_k^{(n_k)} \end{array}\right]. \tag{B4,5}$$

Thus each $\tilde{\mathbf{T}}_k$ and $\tilde{\mathbf{S}}_k$ potentially has a different length, n_k. For this reason, $\tilde{\mathbf{C}}_{ts}$ is not a simple correlation matrix constructed from rectangular matrixes of observation values. This notation, using the superscript parenthesis, comes from Machine Learning methods for dealing with matrixes of "elements" that have different sizes (Goodfellow, Bengio, and Courville, 2016).

B.1 Spatial Profile selection

The in situ data for the correlation matrix are temperature and salinity data versus depth in a "ragged" array or vector of elements. The term ragged refers to the fact that in situ observations are not available at all depths or the matrix is a vector of elements of different sizes. We write this as:

$$\mathbf{x} = \left[\mathbf{x}_1 \quad \mathbf{x}_2 \quad \cdots \quad \mathbf{x}_{n_z} \right] \tag{B6}$$

Where the $\mathbf{x}$ can be either T or S values, n_z is the number of standard depth levels and where each can have a different size, as in equations B4 and B5.

The selection for each grid point is dependent on a 50 km length scale, L . Since the rough distance for one degree is 110 km, the latitude search distance is

$$\Delta lat^s = L / 110 . \tag{B7}$$

The longitude search distance is (Figure B1)

$$\Delta lon^s = (1.3 + 1.7 * e^{-\left(lat^{anal}/15\right)^2}) * \left(L \Big/ \left(110 * \cos\left(lat^{anal} \pi / 180 \right) \right) \right) \tag{B8}$$

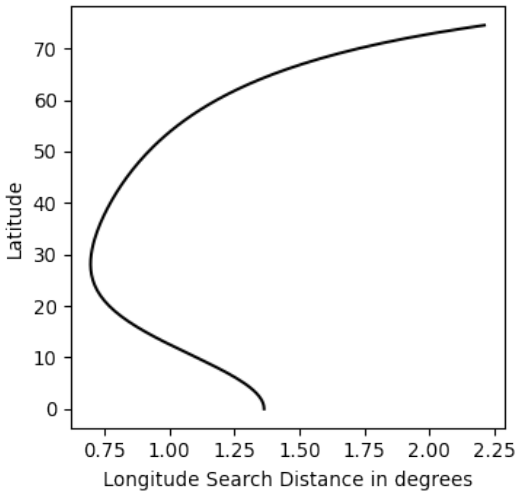

Figure B1. The longitude search distance (Δlon^s) in degrees versus latitude. The latitude search distance (Δlat^s) is 0.45º.

Thus, the longitude search distance is a function of latitude (Figure 1). The selection box, for the profile search becomes

$$lon^{\min} = lon^{anal} - i * \Delta lon^s \tag{B9}$$

$$lon^{\max} = lon^{anal} + i * \Delta lon^s \tag{B10}$$

$$lat^{\min} = lat^{anal} - i * \Delta lat^s \tag{B11}$$

$$lat^{\max} = lat^{anal} + i * \Delta lat^s \tag{B12}$$

Where i=2. Thus for the first iteration, the selection box is $2\Delta lon^s$ by $2\Delta lat^2$. If the selection returns fewer than 1000 profiles, the search is expanded by approximately 50 km using for i=3.

To handle the ragged array with different locations and number of observations at each depth, the summation is only over the number of observation depth levels that occur at both depth levels, i and j. Also, we employ a weighting factor, w_i , that is zero for observations far away from the target horizontal location. The weighting function has an exponential decay computed as:

$$w_{im} = e^{-\left[\left(\Delta lon_{im}/\Delta lon_i^s\right)^2+\left(\Delta lat_{im}/\Delta lat_i^s\right)^2\right]} \tag{B13}$$

Where the longitude and latitude selection ranges, at depth level i, are Δlon_i^s and Δlat_i^s, respectively. The distance from the analysis longitude and altitude, at depth level i and observation profile m, is given by Δlon_{im} and Δlat_{im}, respectively.

B.2 Compute Standard Deviation and Correlation

It is important to note that Δlon_i^s and Δlat_i^s are the search distances that increase based on how many profiles exist. In areas with few data, these values increase by 50 km, iteratively. This could be important and problematic. Future version of ISOP will likely revise these methods.

Computing the correlation using the weights will be more accurate. The weighted mean becomes

$$\overline{\mathbf{x}}_k = \frac{\sum_{m=1}^{n_k} w_m x_k^{(m)}}{\sum_{m=1}^{n_k} w_m}, \tag{B14}$$

where $x_k^{(m)}$ is the mth of n_k observations at depth k, either T or S at depth k. Note that the weight of each profile is the same for each depth but each profile has a different weight. Using the language of probability (e.g. Morin 2016) the mean is an expectation value such as

$$\begin{aligned}\overline{\mathbf{x}}_k &= E_{P(\mathbf{x})}\left\{\mathbf{x}_k\right\} \\ &= \sum_{m=1}^{n_k} x_k^{(m)} P_k^{(m)}\end{aligned} \tag{B15}$$

where $\mathbf{x}_k = \left[\begin{array}{cccc} x_k^{(1)} & x_k^{(2)} & \cdots & x_k^{(n_k)} \end{array}\right]$. Thus, the probability, for each observation is given by

$$P_k^{(m)} = \frac{w_m}{\frac{1}{n_k}\sum_{m=1}^{n_k} w_m} \tag{**B**16}$$

Here $P_k^{(m)}$ is the probability that the mth observation at depth k, represents the ocean at the analysis location. The probability depends on depth, because each depth has potentially a different n_k.

The weighted standard deviation is in terms of expectation values is the square root of variance

$$\begin{aligned}\sigma_k &= \sqrt{\mathrm{var}\left\{\mathbf{x}_k\right\}} \\ &= \sqrt{E_{P(\mathbf{x})}\left\{\left(\mathbf{x}_k - \overline{\mathbf{x}}_k\right)^2\right\}}.\end{aligned} \tag{B17}$$

With the assumption that $\left(\mathbf{x}_k - \overline{\mathbf{x}}_k\right)$ are independent, the probabilities multiply (Rogers and Girolami 2017; Morin 2016) such that

$$\sigma_k = \sqrt{\sum_{m=1}^{n_k}\left(P_k^{(m)}\right)^2\left(x_k^{(m)} - \overline{\mathbf{x}}_k\right)^2} \tag{B18}$$

Or

$$\sigma_k^2 = \sum_{m=1}^{n_k}\left(P_k^{(m)} x_k^{(m)}\right)^2 - \left(\overline{\mathbf{x}}_k\right)^2 \tag{B19}$$

Written "old school" we have

$$\sigma_k = \sqrt{\frac{\sum_{m=1}^{n_k} w_m^2 \left(x_k^{(m)} - \overline{\mathbf{x}}_k \right)^2}{\left(\sum_{m=1}^{n_k} w_m \right)^2}} . \tag{B20}$$

The weighted covariance, between two depths, k1 and k2, is then

$$\mathrm{cov}\left\{ \mathbf{x}_{k1}, \mathbf{x}_{k1} \right\} = \sqrt{E_{P(\mathbf{x})} \left\{ \left(\mathbf{x}_{k1} - \overline{\mathbf{x}}_{k1} \right) \left(\mathbf{x}_{k2} - \overline{\mathbf{x}}_{k2} \right) \right\}} \tag{B21}$$

or

$$\mathrm{cov}\left\{ \mathbf{x}_{k1}, \mathbf{x}_{k2} \right\} = \sum_{m=1}^{(n_{k1}, n_{k2})} P_{k1}^{(m)} P_{k2}^{(m)} \left(x_{k1}^{(m)} - \overline{\mathbf{x}}_{k1} \right) \left(x_{k2}^{(m)} - \overline{\mathbf{x}}_{k2} \right) \tag{B22}$$

where the m summation is only over the profiles that have values at both depths k1 and k2, thus the summation is either n_{k1} or n_{k2} long, denoted $\left(n_{k1}, n_{k2} \right)$ in the top of the summation. In the traditional notation we have

$$\tilde{C}_{k1,k2} = \frac{\sum_{m=1}^{(n_{k1}, n_{k2})} w_m^2 \left(x_{k1}^{(m)} - \overline{\mathbf{x}}_{k1} \right) \left(x_{k2}^{(m)} - \overline{\mathbf{x}}_{k2} \right)}{\left(\sum_{m=1}^{(n_{k1}, n_{k2})} w_m \right)^2 \sigma_{k1} \sigma_{k2}} \quad . \tag{B21}$$

B.3 Time Profile Selection

We have yet to explain how the historical in situ observations are assigned to a particular grid point. For ISOP we compute a monthly climatology of covariances at each grid point. Thus, there is a time selection procedure to assign and month, in addition to the space selection described above.

Time selection uses day-of-year as the time coordinate. Present versions of ISOP ignore interannual variability. Future version will address the issue of climate change particularly at high latitude. The in situ profile's day-of-year, t_m , determines if it will be included in the analysis for a given analysis time, t^{anal} . Because in situ profile observations are more plentiful near the surface, decreasing in number with depth, the time selection expands with depth. Fewer profiles exist at depth because XBTs, for example, only extend down to 900 m at most. Many of the older Arco profiles extend only to 1000 m. The less plentiful CTD casts, however, can extend over the full water column, sometimes to 3000 m.

Version 1 of the ISOP database has a, less than ideal, stepped time expansion with depth. All profiles are selected with an maximum allowable time difference, $\Delta t_k^{\max}$, that varies with depth. Each profile selected satisfies

$$\left| t^{anal} - t_m \right| < \Delta t_k^{\max} , \tag{B22}$$

at each depth. The $\Delta t_k^{\max}$ at standard depth level k, is determined as

$$\begin{aligned}
\Delta t_k &= 45, \quad \text{for } z_k < 100 \text{ m} \\
\Delta t_k &= 60, \quad \text{for } z_k > 100 \text{ m } \& \; z_k \le 200 \text{ m} \\
\Delta t_k &= 90, \quad \text{for } z_k > 200 \text{ m } \& \; z_k \le 400 \text{ m} \\
\Delta t_k &= 120, \quad \text{for } z_k > 400 \text{ m } \& \; z_k \le 700 \text{ m} \\
\Delta t_k &= 400, \quad \text{for } z_k > 700 \text{ m}
\end{aligned} \tag{B23}$$

Thus, some profiles will satisfy (B22) at some depths but not others. The discontinuous function defined by (B23), however, results in blocky covariances. A better function is continuous, such as

$$\Delta t(z_k) = 22.5 + 90.0\left[w(0) - w(z_k)\right], \tag{B24}$$

where

$$w(z_k) = \tan^{-1}\left(s(z_k + p)\right) - \tan^{-1}\left(s(z_k - p)\right). \tag{B25}$$

This function with the parameters $s = 6.0 \times 10^{-3}$ and $p = 9.2 \times 10^{2}$ is shown in Figure B2. At the surface, the maximum time difference is 22.5 days, such that the average time window is 45 days, at the surface increasing with depth.

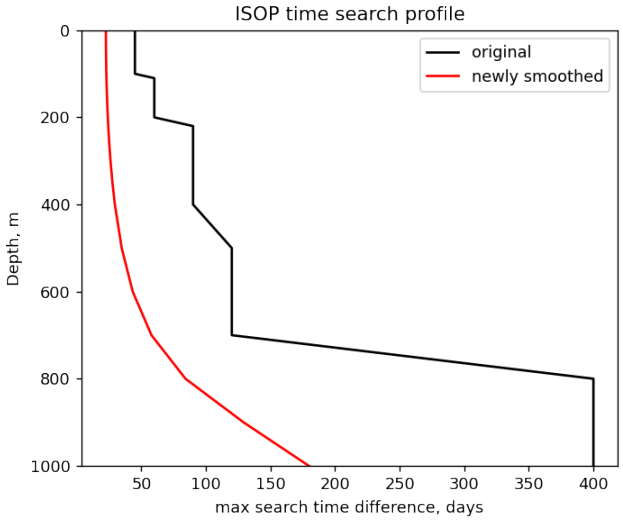

Figure B2. The depth profiles of the depth dependent search time difference for equation (B23) in black and equation (B24) in red.

The result of using equation (B24) is a smoother covariance compared to the covariance from using equation (B23) (Figure B3), which has undesirable blocky structure because of the discontinuous time search function. Figure B3 is for a point in the Greenland Sea and the same set of figures for the North Atlantic are shown in Figure B4. We expect these blocky features in the present (circa 2022) global ocean ISOP database since equation B23 was used. Future versions of ISOP will use a function like that in equation B24.

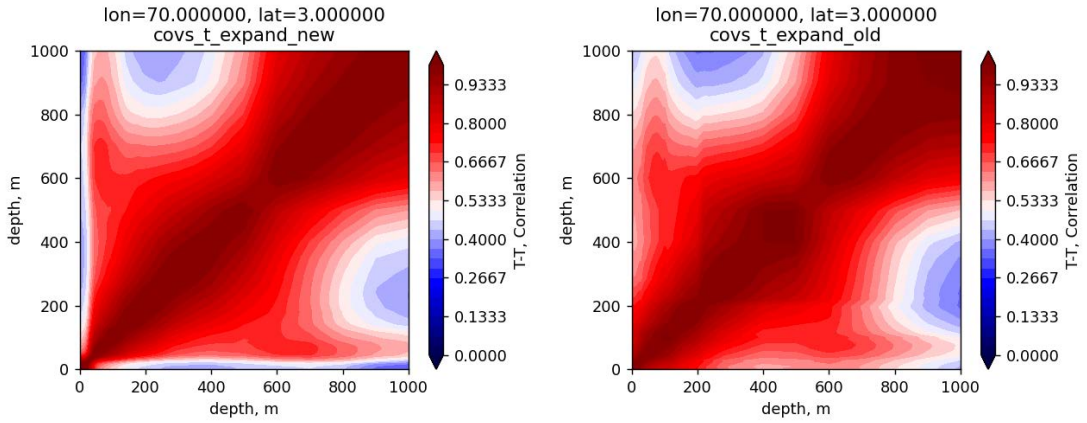

Figure B3. The temperature-temperature vertical covariance in the Greenland Sea at 70^{o}, 3^{o}E, computed (left plot) using the smooth time search profile given in equation (B24). The plot on the right is from using the original, step function methods of equations (B23). The details of the covariance calculation are described in the next section.

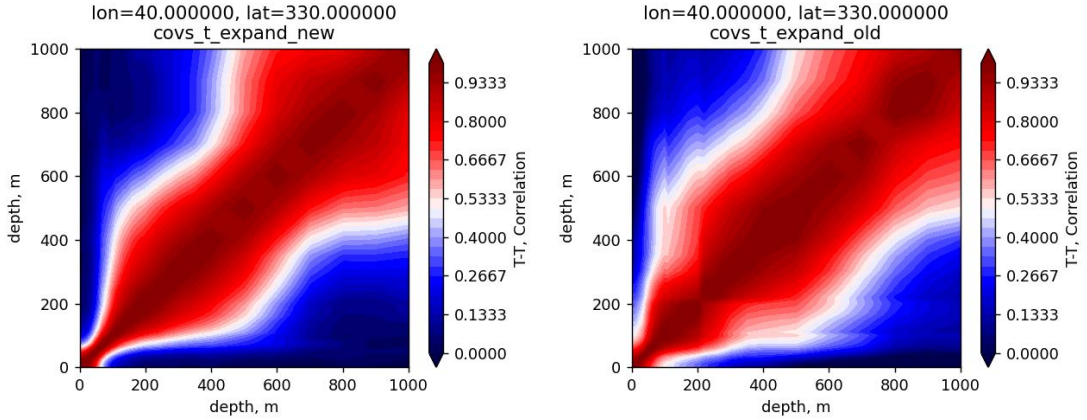

Figure B4. The temperature-temperature vertical covariance in the North Atlantic at 40^{o}, 30^{o}W, computed (left plot) using the smooth time search profile given in equation (B24). The plot on the right is from using the original, step function methods of equations (B23). The details of the covariance calculation are described in the next section.

Appendix C: Computing Geopotential Error Covariance

Since the observation database provides only T and S vertical covariances, geopotential is estimated from the T and S data. Once the vertical geopotential covariances are determined, they can be used for velocity as well. Then, the 3DVAR equation can operate on all five variables T,S,G,U, and V. To do this, we need to construct covariances for geopotential. Geopotential is derived from T and S. Given T and S values at fixed depths define a vector

$$x^T = \left[T_1, T_2, T_3, \cdots T_N, S_1, S_2, S_3, \cdots S_N\right]. \tag{C1}$$

The goal is to convert these T and S into specific volume and then use to get geopotential in the form of steric height, in units of meters. First step is constructing a functional that converts x^T into specific volume

$$\delta = \alpha x \ , \tag{C2}$$

where the functional α operates on the T and S in x to give specific volume

$$\delta = \left[\nu_1, \nu_2, \nu_3, \cdots, \nu_N\right]. \tag{C3}$$

Using specific volume, the steric height can then be computed with another functional

$$\Phi = G\alpha x \tag{C4}$$

to give

$$\Phi = \left[\phi_1, \phi_2, \phi_3, \cdots, \phi_N\right]. \tag{C5}$$

Once we have Φ , then the vertical covariance of geopotential is available for use in NOCDA. Covariance of geopotential ϕ and T,S

$$\left\langle \left(\phi - \overline{\phi}, TS - \overline{TS}\right)^2 \right\rangle \tag{C6}$$

Geopotential anomaly is related to T,S by integrating the specific volume anomaly from the reference level to depth *z*.

Pressure is integral of density times gravitational acceleration above a particular depth. Translate the fixed vertical position to a fixed parcel of material. Consider the total mass above this fixed parcel of material. Regardless of the variation in specific volume either below or above this parcel, the total material above the parcel is constant. Thus the pressure is constant when following this material parcel. The geopotential height is the work done in moving the height of this parcel that represents a particular pressure. To determine how this parcel of fixed pressure moves vertically, it is only necessary to consider the specific volume anomaly beneath the parcel. Thus, the geopotential height anomaly (work done moving height of a particular pressure level due to deviations in T&S from 0,35) is determined by the specific volume anomaly integrated from the ocean bottom to the depth of the parcel prior to displacement:

$$\phi = \int_{bottom}^{\text{pressure level}} \delta(z)\, dp \tag{C7}$$

Given that the T,S variation is assumed to be 0 below a reference level, geopotential can be expressed as a vertical integral from the reference level to a specified depth:

$$\phi = \int_{z_{ref}}^{\text{pressure level}} \delta(z)\, dp \tag{C8}$$

The reasoning behind this assumption is not necessarily physically based but rather motivated by the observational data set, which is only capable of extending to a depth of about 1000m on a regular basis. There is certainly vertical structure of the ocean mesoscale field relating the T,S variations below 1000m to the variations above 1000m, and there is horizontal relations between the vertical structure such as the trailing cyclonic vortices related to the surface manifestations. This variability is not considered. It should be included in future extensions.

Given T,S values at fixed levels, define the vector $x^T = [T_1 \cdots T_N, S_1 \cdots S_N]$, assume there is a specific volume functional α, linearized about an initial temperature and salinity that operates on x. Also define a linear functional operator G that provides a vertical integral from the reference depth to all z and thus provides the geopotential at all depths

$$\phi = G\alpha x \tag{C9}$$

G is a $N \times N$ matrix, and α is a $N \times 2N$ matrix. Extend the vector x by appending the geopotential at each depth so that $y^T = [x^T, \phi_1 \cdots \phi_N]$ so that the length of y is 3N. Given the covariance of x to be defined as UBU^T where U is the diagonal matrix containing the standard deviations of x, the covariance of y is then

$$\langle (y - \bar{y})(y - \bar{y})^T \rangle = \begin{bmatrix} UBU^T & UBU^T\alpha^T G^T \\ G\alpha UBU^T & G\alpha UBU^T\alpha^T G^T \end{bmatrix} \tag{C10}$$

The transformation from x to geopotential specific volume anomaly is provided by the operator α. Formally, computation of specific volume anomaly from temperature and salinity is a nonlinear operation (TEOS-10). Because the transpose of α is necessary, it is easiest to provide α and its transpose by constructing a linear operator that relates temperature and salinity to specific volume anomaly. NCODA is computing analysis increments from observation increments. The increments are relative to the prior forecast. If the prior forecast is relatively accurate, it can be used as the state around which the operator α is linearized. Certainly, the error in the linearization must be considered.

From the Thermodynamic Equation of SeaWater 2010 (TEOS-10), the specific volume anomaly is computed as a function of absolute salinity S_A (which is different from practical salinity) and constant temperature T_C (which is slightly different from potential temperature) and pressure. The ocean models use potential temperature rather than constant temperature, so the datasets computed and shown in the plots are shown as functions of potential temperature, and conversions to constant temperature are performed for calculations in TEOS-10. At pressure 10,153 KPa (given a density of 1035 kg/m^3 at a depth of 1000m), the relation between specific volume anomaly and S_A and T_P computed by TEOS-10 is presented in Figure C1.

The derivative with respect to S_A and T_P is computed numerically using the TEOS-10 routines. The derivatives with respect to S_A and T_P are shown in Figure C2.

With the numerically computed derivative, it is possible to consider the accuracy of a linear approximation over a given temperature or salinity increment. This is computed by first assuming the first derivative with a specified temperature or salinity change (either 1°C or 1 absolute salinity unit) and comparing the value to the value computed at the changed temperature and salinity using TEOS-10. The normalized errors are shown in Figure C3. The errors are normalized by the specific volume anomaly. The errors in using the first derivative with respect to either S_A and T_P are typically well below 1% of the specific volume anomaly. The area in which the errors are larger are where the specific volume anomaly is 0.

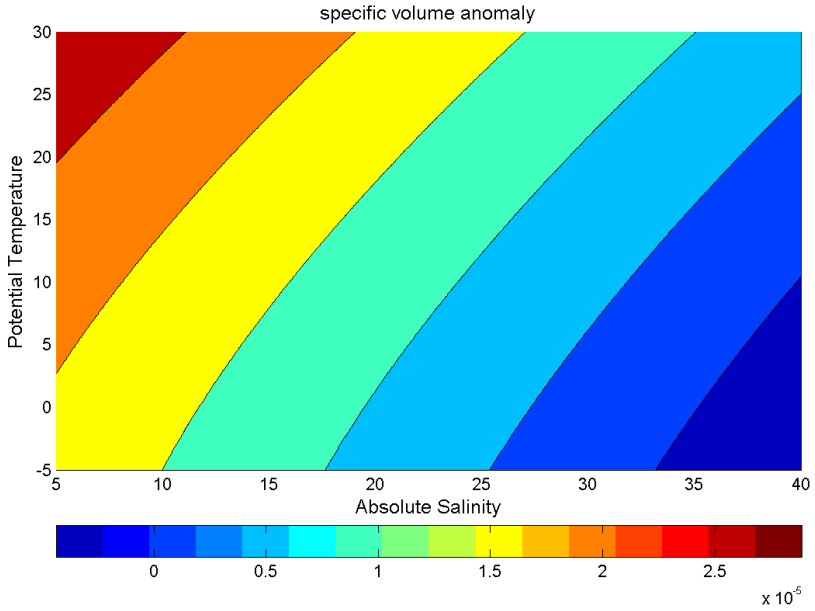

Figure C1: Specific volume anomaly as a function of absolute salinity and constant temperature in units of m^3/kg.

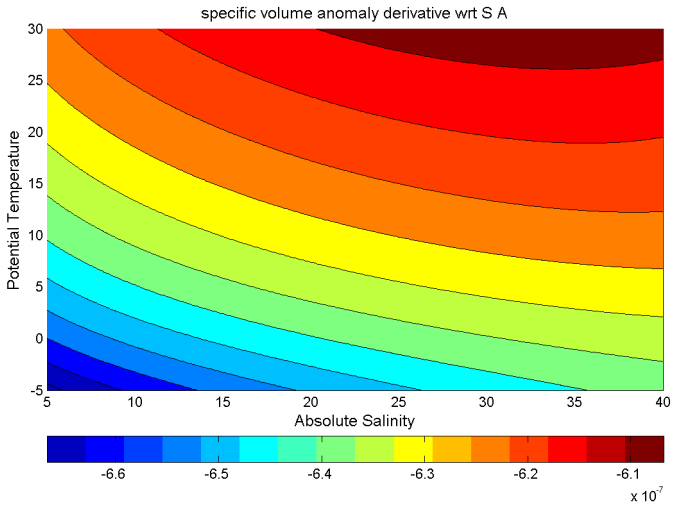

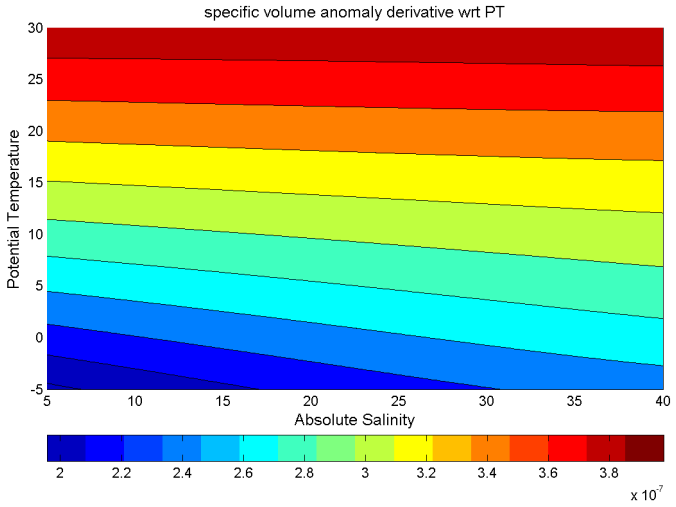

Figure C2: Derivative of specific volume anomaly with respect to absolute salinity (top) and constant temperature (bottom).

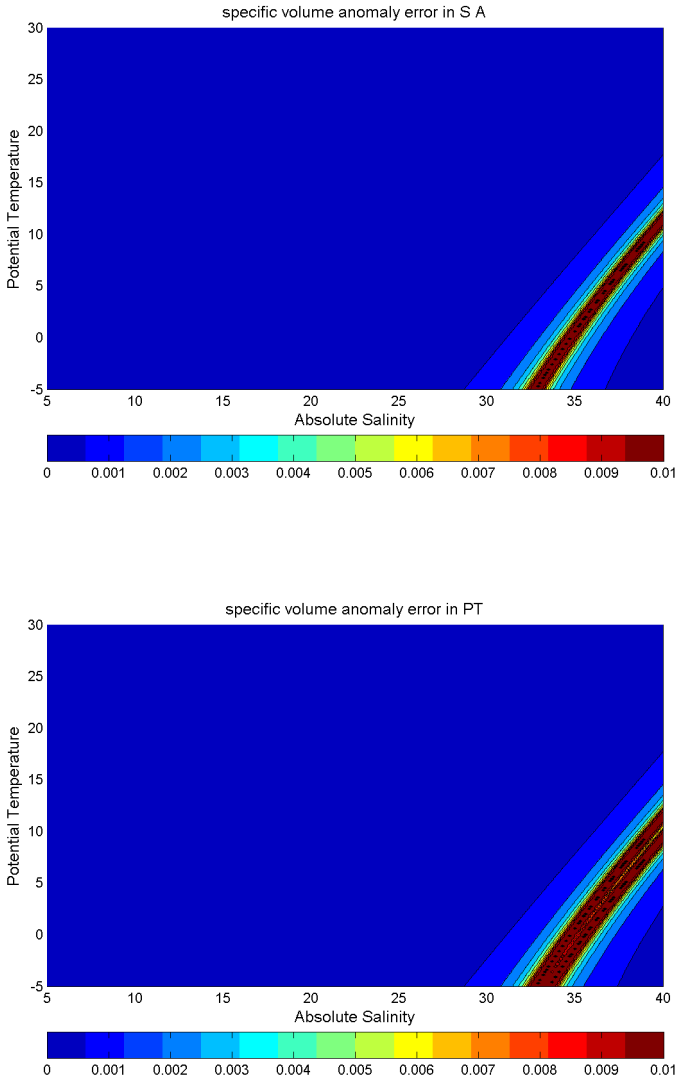

Figure C3: Error in linearized specific volume anomaly for the derivative with respect to absolute salinity (top) and derivative with respect to constant temperature (bottom). The absolute error is first computed, and this is then normalized by the local value of specific volume anomaly.

Gee: G

The vertical integration of specific volume anomaly is accomplished by the matrix G. Assume the ordering of T and S within x is the top of the water column in position 1 and the bottom of the water column in position N. Assume pressures at t the depths of the T,S, geopotential and specific volume anomalies are given by the vector p^T. Thus the vertical integral can be expressed in a summation that computes a trapezoidal integration:

$$\phi_i = \sum_{j=N}^{i+1} \frac{(\delta_{j-1}+\delta_j)}{2}\left(p_j - p_{j-1}\right) \tag{C5}$$

Thus ϕ_i is given by:

$$\begin{aligned}
&\phi_i{}^T \\
&= \left[0,0,0,\cdots,\delta_i \frac{p_{i+1}-p_i}{2}, \delta_{i+1} \frac{(p_{i+2}-p_{i+1})+(p_{i+1}-p_i)}{2}, \ldots, \delta_k \frac{(p_{k+1}-p_k)+(p_k-p_{k-1})}{2}, \ldots, \delta_N \frac{p_N - p_{N-1}}{2}\right] \\
&= \left[0,0,0,\cdots,\delta_i \frac{p_{i+1}-p_i}{2}, \delta_{i+1} \frac{p_{i+2}-p_i}{2}, \ldots, \delta_k \frac{p_{k+1}-p_{k-1}}{2}, \ldots, \delta_N \frac{p_N - p_{N-1}}{2}\right]
\end{aligned} \tag{C6}$$

The case of ϕ_i for $i = N$, g_i is a null vector since the geopotential anomaly at the reference level is zero. This is a simplifying assumption as an initial step. It assumes the model background solution below the depth of the ISOP layer 2 is correct.

Example:

An example of the vertical covariance structure is provided during January at 275°E, 24°N. The vertical structure of the mean temperature and salinity are shown in Figure C4 (solid lines) along with 1 standard deviation (dashed lines). This mean information is based on all historical in situ data taken during January. Each month has an equivalently constructed set of information on the mean and variances information. This location is just northeast of Cuba in the Gulf of Mexico. The salinity shows the characteristic subsurface maximum at 200m depth. The mean is subtracted from the historical in situ data, and the cross correlation between T and S at all depths is constructed. This provides the B matrix at every latitude and longitude point. The B matrix is decomposed through an eigenvalue decomposition to produces $B = \Gamma\Lambda\Gamma^T$ where Γ is the matrix of eigenvectors and Λ is a diagonal matrix of eigenvalues. Only the most significant eigenvectors are saved and stored. This significantly reduces the data requirements. The T and S are stored at 47 standard depths. Thus, to fully store B would require 47x47 values at every latitude and longitude. Only the most significant eigenvectors are retained up to a maximum of 6. This reduces the storage requirements by a factor of 8.

This does not fundamentally change the derivation of the cross covariance matrix between T,S and ϕ in (4). It does however change how the information is formulated and stored. For example, the term in (4)

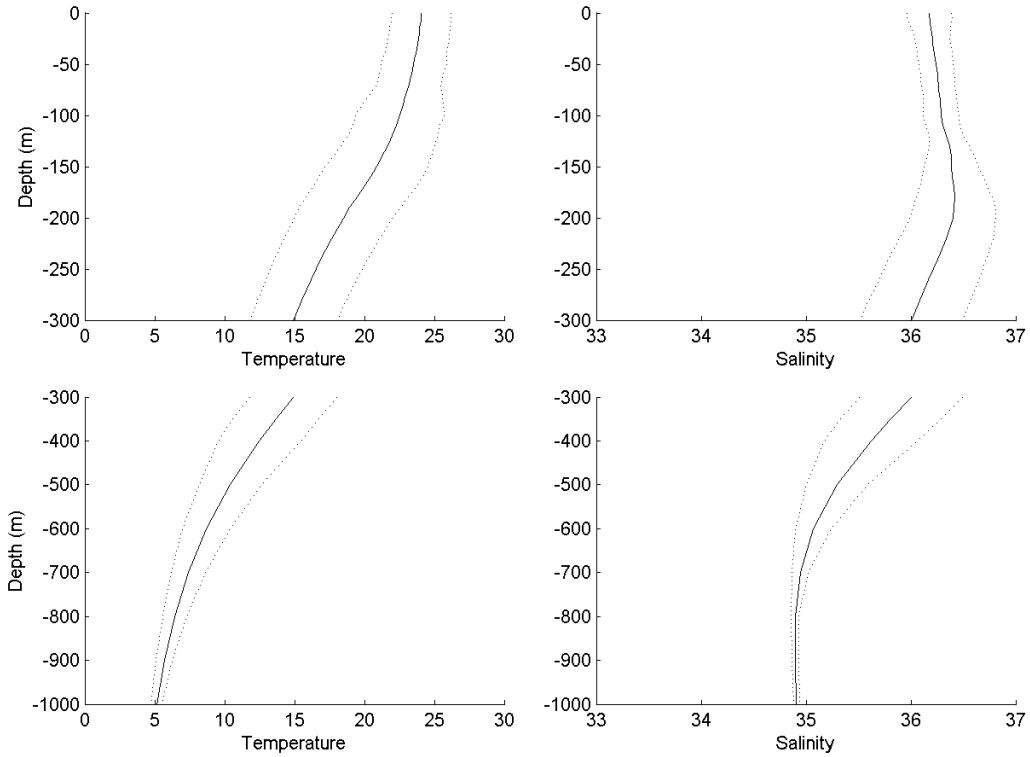

Figure C4. Long term mean during January of temperature and salinity at 275°E, 24°N. The vertical scale is separated into two portions to better show the upper water column.

$$G\alpha UBU^T\alpha^T G^T = G\alpha U\Gamma\Lambda\Gamma^T U^T\alpha^T G^T \tag{C7}$$

Is stored as just the vertical pressure integration and specific volume anomaly operating on the T and S eigenvectors:

$$G\alpha\Gamma \tag{C8}$$

Which is possible since the standard deviation matrix U is diagonal. Thus the cross correlation matrix between T, S and ϕ can be reconstructed based on stored eigenvectors and eigenvalues. An example of the cross correlation matrix at 275°E, 24°N is shown in Figure C5.

The matrix provides the relations between any of the 3 variables at any depth. Thus, given one variable at a particular depth, it is straight forward to determine the correlation to any other variable at any other depth.

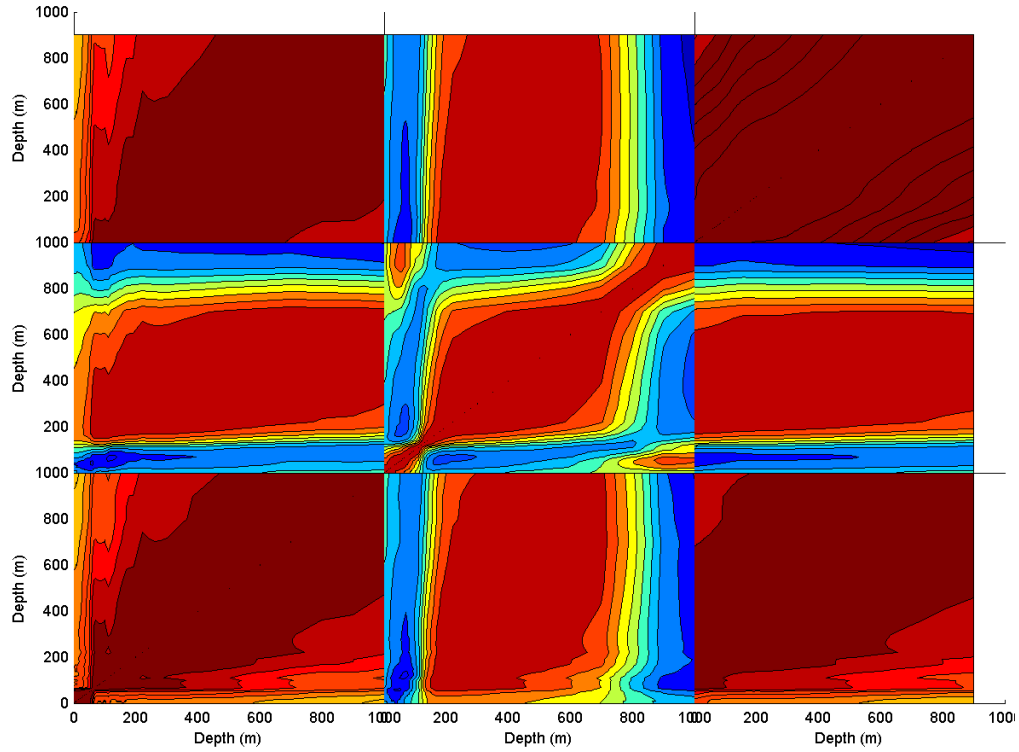

Figure C5. Cross correlation of T, S and φ at 275°E, 24°N for January. This matrix is computed from the eigenvector and eigenvalue information stored in data files. Each month of the year is a separate file, and the eigen information is stored on a 0.5° grid covering the globe.

The cross covariance matrix can also be reconstructed given the standard deviation matrix U that is stored in the same data files as the eigenmode information. An example of the cross covariance matrix is provided below for 275°E, 24°N in Figure C6.

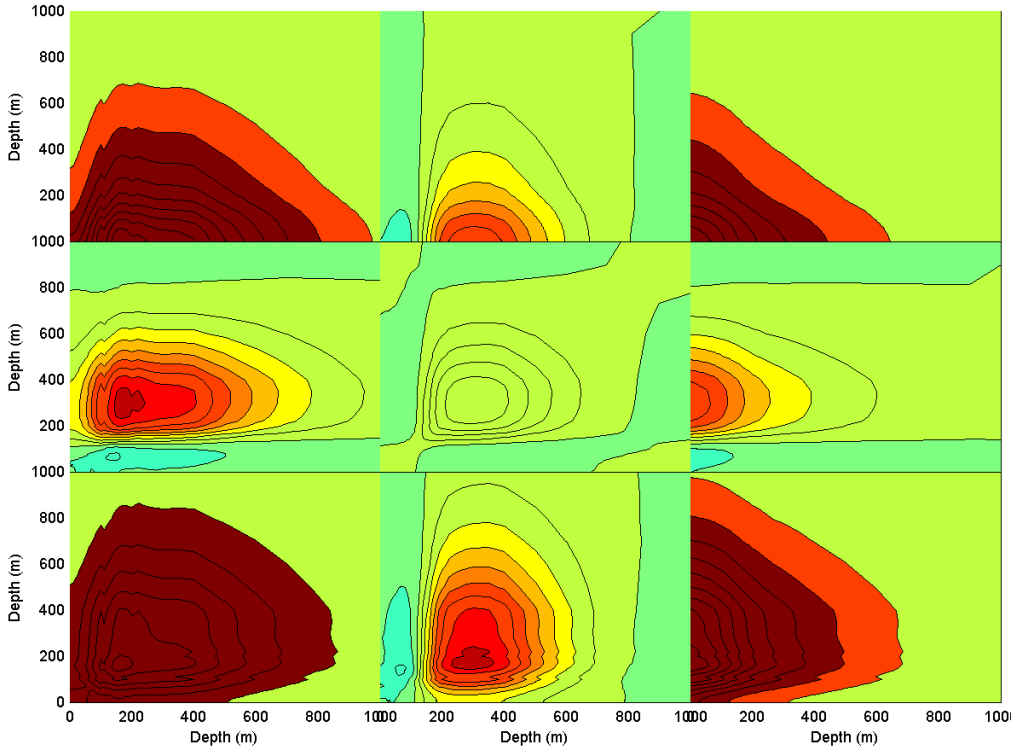

Figure C6. Cross covariance of T, S and φ at 275°E, 24°N for January. This matrix is computed from the eigenvector and eigenvalue information stored in data files. Each month of the year is a separate file, and the eigen information is stored on a 0.5° grid covering the globe.

Appendix D: Four-Dimensional Correlation Interpolation

The correlation at a horizontal position and between two vertical positions is: $C(x, y, z, z')$

The function is 4 dimensional. There are 8 discretized points that surround each of (x, y, z) and (x, y, z'). Let fx, fy, fz and fz' be the fraction distances between the discretized points in the x, y and z directions. Let the subscripts of C_{ijkl} be either 0 or 1 indicating the discretized point just less than or just greater than the interpolation point in each of the directions x, y, z and z'. A functional form of the interpolation is specified as:

$$C(fx, fy, fz, fz') = a + bfx + cfy + dfz + efz' + ffxfy + gfxfz + hfxfz' + ifyfz + jfyfz' + kfzfz' + lfxfyfz + mfxfyfz' + nfyfzfz' + ofxfyfzfz' \quad \text{(D1)}$$

The coefficients $a - o$ should be chosen so that the interpolated value is equal to C_{ijkl}. For example, for $ijkl = 1010$, which indicates the x grid point to the just greater than the interpolation position, the y grid point just less than the interpolation position, and similarly for z and z'. For this point, fx, fy, fz and fz' are coincidentally 1, 0, 1, 0. We want the interpolated value $C(fx, fy, fz, fz')$ to be equal to C_{1010}, that is $C(1,0,1,0) = a + b + dfz + gfxfz = C_{1010}$. Writing this for all C_{ijkl} provides 16 equations for the 16 unknowns $a - o$.

Solving the analytic problem for the unknowns in terms of C_{ijkl} gives us a quad-linear interpolation (like bi-linear or tri-linear, but now 4 dimensions). For example, consider the 2D interpolation problem

$$C(fx, fy) = a + bfx + cfy + dfxfy \quad \text{(D2)}$$
$$C_{00} = a \quad \text{(D3)}$$
$$C_{10} = a + b \quad \text{(D4)}$$
$$C_{01} = a + c \quad \text{(D5)}$$
$$C_{11} = a + b + c + d \quad \text{(D6)}$$

And the solution for the unknowns is

$$a = C_{00} \quad \text{(D7)}$$
$$b = C_{10} - C_{00} \quad \text{(D8)}$$
$$c = C_{01} - C_{00} \quad \text{(D9)}$$
$$d = C_{11} - C_{01} - C_{10} + C_{00} \quad \text{(D10)}$$

Substituting the coefficient solution back into (2) and rearranging,

$$C(fx, fy) = C_{00}(1 - fx - fy + fxfy) + C_{10}(fx - fxfy) + C_{01}(fy - fxy) + C_{11}(fxfy) \quad \text{(D11)}$$

How does this compare to the case of interpolating each dimension successively? General interpolation in a dimension d is:

$$C(fd) = C_0(1 - fd) + C_1(fd)$$

Applying to x,

$$C_{x0} = C_{00}(1-fx) + C_{10}(fx)$$
$$C_{x1} = C_{01}(1-fx) + C_{11}(fx)$$

Then interpolating C_{x0} and C_{x1} in y,

$$C_{xy} = C_{x0}(1-fy) + C_{x1}(fy) = \big(C_{00}(1-fx) + C_{10}(fx)\big)(1-fy) + \big(C_{01}(1-fx) + C_{11}(fx)\big)fy$$
$$= C_{00}(1-fx-fy-fxfy) + C_{10}(fx-fxfy) + C_{01}(fy-fxfy) + C_{11}(fxfy)$$

Now the exercise is to apply this same derivation to the 4 dimensional case. Because this done in four dimensions get rather long, we used Mathematica (Wolfram 2012). Below is an export of a Mathematica notebook:

Define the interpolated correlation as this rule in the 2D case:

```
M[fx_,fy_]={1,fx,fy,fx*fy}
{1,fx,fy,fx fy}
```

where the fx and fy are the fractional distances between the grid points in the x and y directions. Put this in a matrix so that we can solve it:

```
MM={M[0,0],M[1,0],M[0,1],M[1,1]}
{{1,0,0,0},{1,1,0,0},{1,0,1,0},{1,1,1,1}}
```

The known correlations at the corners of the grid box are:

```
ICorr={Cor0,0,Cor1,0,Cor0,1,Cor1,1}
{Cor0,0,Cor1,0,Cor0,1,Cor1,1}
```

The coefficient we need are:

```
X:={a,b,c,d}
```

The equation to solve is:

```
MM.X==ICorr
{a,a+b,a+c,a+b+c+d}=={Cor0,0,Cor1,0,Cor0,1,Cor1,1}
```

The solution that we already know is:

```
LinearSolve[MM,ICorr]
{Cor0,0,-Cor0,0+Cor1,0,-Cor0,0+Cor0,1,Cor0,0-Cor0,1-Cor1,0+Cor1,1}
```

The solution is then

```
X:=LinearSolve[MM,ICorr]
SCor=Collect[X.M[fx,fy],{Cor0,0,Cor1,0,Cor1,0,Cor0,1,Cor1,1}]
(1-fx-fy+fx fy) Cor0,0+(fy-fx fy) Cor0,1+(fx-fx fy) Cor1,0+fx fy
Cor1,1
```

The other method is to interpolate each dimension independently. The one dimensional interpolation is:

```
I1D[x0_,x1_,fx_]=x0*(1-fx)+x1*fx
(1-fx) x0+fx x1
```

Try it out

```
Corx,0=I1D[Cor0,0,Cor1,0,fx]
(1-fx) Cor0,0+fx Cor1,0
Corx,1=I1D[Cor0,1,Cor1,1,fx]
(1-fx) Cor0,1+fx Cor1,1
Corx,y=Collect[I1D[Corx,0,Corx,1,fy],{Cor0,0,Cor1,0,Cor0,1,Cor1,1}]
(1-fx) (1-fy) Cor0,0+(1-fx) fy Cor0,1+fx (1-fy) Cor1,0+fx fy Cor1,1
```

Note that this is the same as SCor above. Test that:

```
Expand[SCor]-Expand[Corx,y]
0
```

Now for the four dimensional case, the rule is (note Gregg fogot the x*z*zp term):

```
M[x_,y_,z_,zp_]:={1,x,y,z,zp,x*y,x*z,x*zp,y*z,y*zp,z*zp,x*y*z,x*y*zp,y
*z*zp,x*z*zp,x*y*z*zp}
```

With the correct number of terms, the coefficients now go to p.

```
M[1,0,1,0].{a,b,c,d,e,f,g,h,i,j,k,l,m,n,o,p}
a+b+d+g
```

So, we can get the values at every point. Here is an example :

```
M[0,1,0,1]
{1,0,1,0,1,0,0,0,0,1,0,0,0,0,0,0}
```

Make the matrix so that we can solve it:

```
MM={M[0,0,0,0],M[1,0,0,0],M[0,1,0,0],M[1,1,0,0],
  M[0,0,1,0],M[1,0,1,0],M[0,1,1,0],M[1,1,1,0],
  M[0,0,0,1],M[1,0,0,1],M[0,1,0,1],M[1,1,0,1],
  M[0,0,1,1],M[1,0,1,1],M[0,1,1,1],M[1,1,1,1]}

{{1,0,0,0,0,0,0,0,0,0,0,0,0,0,0,0},{1,1,0,0,0,0,0,0,0,0,0,0,0,0,0,0},{
1,0,1,0,0,0,0,0,0,0,0,0,0,0,0,0},{1,1,1,0,0,1,0,0,0,0,0,0,0,0,0,0},{1,
0,0,1,0,0,0,0,0,0,0,0,0,0,0,0,0},{1,1,0,1,0,0,1,0,0,0,0,0,0,0,0,0},{1,0,
1,1,0,0,0,0,1,0,0,0,0,0,0,0},{1,1,1,1,0,1,1,0,1,0,0,1,0,0,0,0},{1,0,0,
0,1,0,0,0,0,0,0,0,0,0,0,0},{1,1,0,0,1,0,0,1,0,0,0,0,0,0,0,0},{1,0,1,0,
1,0,0,0,0,1,0,0,0,0,0,0},{1,1,1,0,1,1,0,1,0,1,0,0,1,0,0,0},{1,0,0,1,1,
0,0,0,0,0,1,0,0,0,0,0},{1,1,0,1,1,0,1,1,0,0,1,0,0,0,1,0},{1,0,1,1,1,0,
0,0,1,1,1,0,0,1,0,0},{1,1,1,1,1,1,1,1,1,1,1,1,1,1,1,1}}
```

The knowns are:

```
A={CC0,0,0,0,CC1,0,0,0,CC0,1,0,0,CC1,1,0,0,
  CC0,0,1,0,CC1,0,1,0,CC0,1,1,0,CC1,1,1,0,
  CC0,0,0,1,CC1,0,0,1,CC0,1,0,1,CC1,1,0,1,
  CC0,0,1,1,CC1,0,1,1,CC0,1,1,1,CC1,1,1,1}

{CC0,0,0,0,CC1,0,0,0,CC0,1,0,0,CC1,1,0,0,CC0,0,1,0,CC1,0,1,0,CC0,1,1,0
,CC1,1,1,0,CC0,0,0,1,CC1,0,0,1,CC0,1,0,1,CC1,1,0,1,CC0,0,1,1,CC1,0,1,1
,CC0,1,1,1,CC1,1,1,1}
```

The solution for the four dimensional case is:

```
LinearSolve[MM,A]
{CC0,0,0,0,-CC0,0,0,0+CC1,0,0,0,-CC0,0,0,0+CC0,1,0,0,-
CC0,0,0,0+CC0,0,1,0,-CC0,0,0,0+CC0,0,0,1,CC0,0,0,0-CC0,1,0,0-
CC1,0,0,0+CC1,1,0,0,CC0,0,0,0-CC0,0,1,0-CC1,0,0,0+CC1,0,1,0,CC0,0,0,0-
CC0,0,0,1-CC1,0,0,0+CC1,0,0,1,CC0,0,0,0-CC0,0,1,0-
CC0,1,0,0+CC0,1,1,0,CC0,0,0,0-CC0,0,0,1-CC0,1,0,0+CC0,1,0,1,CC0,0,0,0-
CC0,0,0,1-CC0,0,1,0+CC0,0,1,1,-CC0,0,0,0+CC0,0,1,0+CC0,1,0,0-
CC0,1,1,0+CC1,0,0,0-CC1,0,1,0-CC1,1,0,0+CC1,1,1,0,-
```

```
CC0,0,0,0+CC0,0,0,1+CC0,1,0,0-CC0,1,0,1+CC1,0,0,0-CC1,0,0,1-
CC1,1,0,0+CC1,1,0,1,-CC0,0,0,0+CC0,0,0,1+CC0,0,1,0-
CC0,0,1,1+CC0,1,0,0-CC0,1,0,1-CC0,1,1,0+CC0,1,1,1,-
CC0,0,0,0+CC0,0,0,1+CC0,0,1,0-CC0,0,1,1+CC1,0,0,0-CC1,0,0,1-
CC1,0,1,0+CC1,0,1,1,CC0,0,0,0-CC0,0,0,1-CC0,0,1,0+CC0,0,1,1-
CC0,1,0,0+CC0,1,0,1+CC0,1,1,0-CC0,1,1,1-CC1,0,0,0+CC1,0,0,1+CC1,0,1,0-
CC1,0,1,1+CC1,1,0,0-CC1,1,0,1-CC1,1,1,0+CC1,1,1,1}
```

The solution is then

```
 X:=LinearSolve[MM,A]
 X
 {CC0,0,0,0,-CC0,0,0,0+CC1,0,0,0,-CC0,0,0,0+CC0,1,0,0,-
CC0,0,0,0+CC0,0,1,0,-CC0,0,0,0+CC0,0,0,1,CC0,0,0,0-CC0,1,0,0-
CC1,0,0,0+CC1,1,0,0,CC0,0,0,0-CC0,0,1,0-CC1,0,0,0+CC1,0,1,0,CC0,0,0,0-
CC0,0,0,1-CC1,0,0,0+CC1,0,0,1,CC0,0,0,0-CC0,0,1,0-
CC0,1,0,0+CC0,1,1,0,CC0,0,0,0-CC0,0,0,1-CC0,1,0,0+CC0,1,0,1,CC0,0,0,0-
CC0,0,0,1-CC0,0,1,0+CC0,0,1,1,-CC0,0,0,0+CC0,0,1,0+CC0,1,0,0-
CC0,1,1,0+CC1,0,0,0-CC1,0,1,0-CC1,1,0,0+CC1,1,1,0,-
CC0,0,0,0+CC0,0,0,1+CC0,1,0,0-CC0,1,0,1+CC1,0,0,0-CC1,0,0,1-
CC1,1,0,0+CC1,1,0,1,-CC0,0,0,0+CC0,0,0,1+CC0,0,1,0-
CC0,0,1,1+CC0,1,0,0-CC0,1,0,1-CC0,1,1,0+CC0,1,1,1,-
CC0,0,0,0+CC0,0,0,1+CC0,0,1,0-CC0,0,1,1+CC1,0,0,0-CC1,0,0,1-
CC1,0,1,0+CC1,0,1,1,CC0,0,0,0-CC0,0,0,1-CC0,0,1,0+CC0,0,1,1-
CC0,1,0,0+CC0,1,0,1+CC0,1,1,0-CC0,1,1,1-CC1,0,0,0+CC1,0,0,1+CC1,0,1,0-
CC1,0,1,1+CC1,1,0,0-CC1,1,0,1-CC1,1,1,0+CC1,1,1,1}
 SCor=Collect[X.M[fx,fy,fz,fzp],A]
 (1-fx-fy+fx fy-fz+fx fz+fy fz-fx fy fz-fzp+fx fzp+fy fzp-fx fy fzp+fz
fzp-fx fz fzp-fy fz fzp+fx fy fz fzp) CC0,0,0,0+(fzp-fx fzp-fy fzp+fx
fy fzp-fz fzp+fx fz fzp+fy fz fzp-fx fy fz fzp) CC0,0,0,1+(fz-fx fz-fy
fz+fx fy fz-fz fzp+fx fz fzp+fy fz fzp-fx fy fz fzp) CC0,0,1,0+(fz
fzp-fx fz fzp-fy fz fzp+fx fy fz fzp) CC0,0,1,1+(fy-fx fy-fy fz+fx fy
fz-fy fzp+fx fy fzp+fy fz fzp-fx fy fz fzp) CC0,1,0,0+(fy fzp-fx fy
fzp-fy fz fzp+fx fy fz fzp) CC0,1,0,1+(fy fz-fx fy fz-fy fz fzp+fx fy
fz fzp) CC0,1,1,0+(fy fz fzp-fx fy fz fzp) CC0,1,1,1+(fx-fx fy-fx
fz+fx fy fz-fx fzp+fx fy fzp+fx fz fzp-fx fy fz fzp) CC1,0,0,0+(fx
fzp-fx fy fzp-fx fz fzp+fx fy fz fzp) CC1,0,0,1+(fx fz-fx fy fz-fx fz
fzp+fx fy fz fzp) CC1,0,1,0+(fx fz fzp-fx fy fz fzp) CC1,0,1,1+(fx fy-
fx fy fz-fx fy fzp+fx fy fz fzp) CC1,1,0,0+(fx fy fzp-fx fy fz fzp)
CC1,1,0,1+(fx fy fz-fx fy fz fzp) CC1,1,1,0+fx fy fz fzp CC1,1,1,1
```

Now the other interpolate in 1D cases again.

```
 I1D[x0_,x1_,fx_]=x0*(1-fx)+x1*fx
 (1-fx) x0+fx x1
 Cor0,0,z,0:=I1D[Cor0,0,0,0,Cor0,0,1,0,fz]
 Cor0,0,z,1:=I1D[Cor0,0,0,1,Cor0,0,1,1,fz]
 Cor0,0,z,zp:=I1D[Cor0,0,z,0,Cor0,0,z,1,fzp]
```

First fzp

```
 Cor0,1,z,0:=I1D[Cor0,1,0,0,Cor0,1,1,0,fz]
 Cor0,1,z,1:=I1D[Cor0,1,0,1,Cor0,1,1,1,fz]
 Cor0,1,z,zp:=I1D[Cor0,1,z,0,Cor0,1,z,1,fzp]
```

second fzp

```
Cor0,y,z,zp:=I1D[Cor0,0,z,zp,Cor0,1,z,zp,fy]
```

first fy

```
Cor1,0,z,0:=I1D[Cor1,0,0,0,Cor1,0,1,0,fz]
Cor1,0,z,1:=I1D[Cor1,0,0,1,Cor1,0,1,1,fz]
Cor1,0,z,zp:=I1D[Cor1,0,z,0,Cor1,0,z,1,fzp]
```

fist fzp for second 10

```
Cor1,1,z,0:=I1D[Cor1,1,0,0,Cor1,1,1,0,fz]
Cor1,1,z,1:=I1D[Cor1,1,0,1,Cor1,1,1,1,fz]
Cor1,1,z,zp:=I1D[Cor1,1,z,0,Cor1,1,z,1,fzp]
```

second fzp for second 11

```
Cor1,y,z,zp:=I1D[Cor1,0,z,zp,Cor1,1,z,zp,fy]
```

The whole shebang

```
 Corx,y,z,zp:=I1D[Cor0,y,z,zp,Cor1,y,z,zp,fx]
```

Ok, did this work? Oh, I have to conver the CC to Cor or visa versa

```
 Corx,y,z,zp=I1D[Cor0,y,z,zp,Cor1,y,z,zp,fx]/.{Cor->CC}
 (1-fx) ((1-fy) ((1-fzp) ((1-fz) CC0,0,0,0+fz CC0,0,1,0)+fzp ((1-fz)
CC0,0,0,1+fz CC0,0,1,1))+fy ((1-fzp) ((1-fz) CC0,1,0,0+fz
CC0,1,1,0)+fzp ((1-fz) CC0,1,0,1+fz CC0,1,1,1)))+fx ((1-fy) ((1-fzp)
((1-fz) CC1,0,0,0+fz CC1,0,1,0)+fzp ((1-fz) CC1,0,0,1+fz
CC1,0,1,1))+fy ((1-fzp) ((1-fz) CC1,1,0,0+fz CC1,1,1,0)+fzp ((1-fz)
CC1,1,0,1+fz CC1,1,1,1)))
 Expand[Corx,y,z,zp]-Expand[SCor]
 0
Both interpolation methods are equivalent.
```

Practical matters

Change the subscripts to arguments and change 0 and 1 arguments to 1 and 2. Output in FARTRAN:

```
 SS:=Corx,y,z,zp/.{CCx_,y_,z_,zp_->vc[x+1,y+1,z+1,zp+1]}
 FortranForm[SS]
         (1 - fx)*((1 - fy)*((1 - fzp)*
     -         ((1 - fz)*vc(1,1,1,1) + fz*vc(1,1,2,1)) +
     -        fzp*((1 - fz)*vc(1,1,1,2) + fz*vc(1,1,2,2))) +
     -      fy*((1 - fzp)*((1 - fz)*vc(1,2,1,1) + fz*vc(1,2,2,1)) +
     -         fzp*((1 - fz)*vc(1,2,1,2) + fz*vc(1,2,2,2)))) +
     -   fx*((1 - fy)*((1 - fzp)*
     -         ((1 - fz)*vc(2,1,1,1) + fz*vc(2,1,2,1)) +
     -        fzp*((1 - fz)*vc(2,1,1,2) + fz*vc(2,1,2,2))) +
     -      fy*((1 - fzp)*((1 - fz)*vc(2,2,1,1) + fz*vc(2,2,2,1)) +
     -         fzp*((1 - fz)*vc(2,2,1,2) + fz*vc(2,2,2,2))))
```

Now make a rule to convert indexes to a 1D array. In FORTRAN the first index moves the fastest!

```
 vc[x_,y_,z_,zp_]:=vcorr[8*(zp-1)+4*(z-1)+2*(y-1)+x]
```

Test it

```
 vc[1,1,1,1]
 vcorr[1]
 vc[1,1,1,2]
 vcorr[9]
 vc[2,1,1,1]
 vcorr[2]
 vc[2,2,2,2]
 vcorr[16]
```

This appears to be working.

```
 FortranForm[SS]
         (1 - fx)*((1 - fy)*((1 - fzp)*
     -         ((1 - fz)*vcorr(1) + fz*vcorr(5)) +
     -        fzp*((1 - fz)*vcorr(9) + fz*vcorr(13))) +
     -      fy*((1 - fzp)*((1 - fz)*vcorr(3) + fz*vcorr(7)) +
     -         fzp*((1 - fz)*vcorr(11) + fz*vcorr(15)))) +
     -   fx*((1 - fy)*((1 - fzp)*((1 - fz)*vcorr(2) + fz*vcorr(6)) +
```

```
     -        fzp*((1 - fz)*vcorr(10) + fz*vcorr(14))) +
     -     fy*((1 - fzp)*((1 - fz)*vcorr(4) + fz*vcorr(8)) +
     -        fzp*((1 - fz)*vcorr(12) + fz*vcorr(16))))

 HornerForm[SS]
 (1+fz (-1+fzp)-fzp+fy (-1+fz (1-fzp)+fzp)+fx (-1+fz (1-fzp)+fy (1+fz
(-1+fzp)-fzp)+fzp)) vcorr[1]+fzp vcorr[9]+fz (vcorr[5]+fzp (-vcorr[5]-
vcorr[9]+vcorr[13]))+fy (vcorr[3]+fzp (-vcorr[3]-
vcorr[9]+vcorr[11])+fz (-vcorr[3]-vcorr[5]+vcorr[7]+fzp
(vcorr[3]+vcorr[5]-vcorr[7]+vcorr[9]-vcorr[11]-
vcorr[13]+vcorr[15])))+fx (vcorr[2]+fzp (-vcorr[2]-
vcorr[9]+vcorr[10])+fz (-vcorr[2]-vcorr[5]+vcorr[6]+fzp
(vcorr[2]+vcorr[5]-vcorr[6]+vcorr[9]-vcorr[10]-
vcorr[13]+vcorr[14]))+fy (-vcorr[2]-vcorr[3]+vcorr[4]+fzp
(vcorr[2]+vcorr[3]-vcorr[4]+vcorr[9]-vcorr[10]-vcorr[11]+vcorr[12])+fz
(vcorr[2]+vcorr[3]-vcorr[4]+vcorr[5]-vcorr[6]-vcorr[7]+vcorr[8]+fzp (-
vcorr[2]-vcorr[3]+vcorr[4]-vcorr[5]+vcorr[6]+vcorr[7]-vcorr[8]-
vcorr[9]+vcorr[10]+vcorr[11]-vcorr[12]+vcorr[13]-vcorr[14]-
vcorr[15]+vcorr[16])))))
```

Appendix E: Deriving Analysis Error Variance

According to Daley and Barker (2000,2001), the analysis error covariance is given by (see Daley and Barker (2000) equation 10.1 on page 89)

$$\mathbf{B}_{anal} = \mathbf{B} - \mathbf{B}\mathbf{H}^T \left(\mathbf{H}\mathbf{B}\mathbf{H}^T - \mathbf{R} \right)^{-1} \mathbf{H}\mathbf{B}. \tag{E1}$$

As described in section 2.1, equation 7, we use again the notation

$$\underbrace{\mathbf{B}}_{n\times n}\underbrace{\mathbf{H}^T}_{n\times k} = \underbrace{\mathbf{B}\big|_{obs}^{grd}}_{n\times k} \quad \text{and} \quad \underbrace{\mathbf{H}}_{k\times n}\underbrace{\mathbf{B}}_{n\times n}\underbrace{\mathbf{H}^T}_{n\times k} = \underbrace{\mathbf{B}\big|_{obs}^{obs}}_{k\times k} \tag{E2) and (E3}$$

To keep track of the matrix sizes, we use n as the number of grid points and k as the number of observations. But, now we also need

$$\underbrace{\mathbf{H}}_{k\times n}\underbrace{\mathbf{B}}_{n\times n} = \underbrace{\mathbf{B}\big|_{grd}^{obs}}_{k\times n}. \tag{E4}$$

Equation (E1) then becomes

$$\mathbf{B}_{anal} = \mathbf{B}_{grd} - \mathbf{B}\big|_{obs}^{grd} \left(\mathbf{B}\big|_{obs}^{obs} - \mathbf{R} \right)^{-1} \mathbf{B}\big|_{grd}^{obs}, \tag{E5}$$

where $\mathbf{B}_{grd}$ is the background error on the analysis grid. Now, in NCODA, there is a series of functions the perform the localization assumptions through the correlations. These functions perform correlations from one point to another, such as from the observation locations to the grid locations

$$\underbrace{C\big|_{obs}^{grd}}_{nxk} \quad \text{and} \quad \underbrace{C\big|_{grd}^{obs}}_{kxn} \tag{E6) and (E7}$$

depending on the order of operations. In addition, the functions correlate between to observation locations

$$\underbrace{C\big|_{obs}^{obs}}_{kxk}. \tag{E8}$$

And also, diagonalize the background variances, at grid locations and observation locations

$$\mathbf{V}_{grd} = \mathrm{diag}\left(\mathbf{B}_{grd} \right) \text{ and } \mathbf{V}_{obs} = \mathrm{diag}\left(\mathbf{B}_{obs} \right). \tag{E9) and (E10}$$

Since variance is diagonal, the correlation is used to construct covariance

$$\mathbf{B}\big|_{obs}^{grd} = \mathbf{V}_{grd}^{1/2} C\big|_{obs}^{grd} \mathbf{V}_{obs}^{1/2} \text{ and } \mathbf{B}\big|_{obs}^{obs} = \mathbf{V}_{obs}^{1/2} C\big|_{obs}^{obs} \mathbf{V}_{obs}^{1/2} \tag{E11) and (E12}$$

and

$$\mathbf{B}\big|_{grd}^{obs} = \mathbf{V}_{obs}^{1/2} C\big|_{grd}^{obs} \mathbf{V}_{grd}^{1/2}. \tag{E13}$$

Now, equation E5 becomes

$$\mathbf{B}_{anal} = \mathbf{B}_{grd} - \mathbf{V}_{grd}^{1/2} C\big|_{obs}^{grd} \mathbf{V}_{obs}^{1/2} \left(\mathbf{V}_{obs}^{1/2} C\big|_{obs}^{obs} \mathbf{V}_{obs}^{1/2} - \mathbf{R} \right)^{-1} \mathbf{V}_{obs}^{1/2} C\big|_{grd}^{obs} \mathbf{V}_{grd}^{1/2}. \tag{E14}$$

Now, we need to apply the fact that $\left(AB\right)^{-1} - B^{-1}A^{-1}$ such that 14 becomes

$$\mathbf{B}_{anal} = \mathbf{B}_{grd} - \mathbf{V}_{grd}^{1/2} C\big|_{obs}^{grd} \left(\mathbf{V}_{obs}^{1/2} C\big|_{obs}^{obs} \mathbf{V}_{obs}^{1/2} \mathbf{V}_{obs}^{-1/2} - \mathbf{R}\mathbf{V}_{obs}^{-1/2} \right)^{-1} \mathbf{V}_{obs}^{1/2} C\big|_{grd}^{obs} \mathbf{V}_{grd}^{1/2}$$

or

$$\mathbf{B}_{anal} = \mathbf{B}_{grd} - \mathbf{V}_{grd}^{1/2} C\big|_{obs}^{grd} \left(\mathbf{V}_{obs}^{1/2} C\big|_{obs}^{obs} - \mathbf{R}\mathbf{V}_{obs}^{-1/2} \right)^{-1} \mathbf{V}_{obs}^{1/2} C\big|_{grd}^{obs} \mathbf{V}_{grd}^{1/2}$$

and again

$$\mathbf{B}_{anal} = \mathbf{B}_{grd} - \mathbf{V}_{grd}^{1/2} C\big|_{obs}^{grd} \left(C\big|_{obs}^{obs} - \mathbf{V}_{obs}^{-1/2} \mathbf{R} \mathbf{V}_{obs}^{-1/2} \right)^{-1} C\big|_{grd}^{obs} \mathbf{V}_{grd}^{1/2}$$

or

$$\mathbf{B}_{anal} = \mathbf{B}_{grd} - \mathbf{V}_{grd}^{1/2} C\big|_{obs}^{grd} \left(C\big|_{obs}^{obs} - \mathbf{V}_{obs}^{-1}\mathbf{R} \right)^{-1} C\big|_{grd}^{obs} \mathbf{V}_{grd}^{1/2} \tag{E15}$$

But, I know that our analysis error is diagonal. There is no cross-analysis error. Since $\mathbf{V}_{grd}$ is diagonal and the observations are assumed to be uncorrelated $\mathbf{R}$ is diagonal, we have a diagonalize this matrix

$$\mathrm{diag}\left[\mathbf{B}_{anal}\right] = \mathbf{V}_{grd} \text{-} \mathbf{V}_{grd}^{1/2} C\big|_{obs}^{grd} \left(C\big|_{obs}^{obs} - \mathbf{V}_{obs}^{-1}\mathbf{R} \right)^{-1} C\big|_{grd}^{obs} \mathbf{V}_{grd}^{1/2} . \tag{E16}$$

Here we separate the analysis error into factors, since everything is diagonal

$$\mathbf{V}_{grd}\mathbf{V}^{(anal)} = \mathbf{V}_{grd} \left[\mathbf{I} - C\big|_{obs}^{grd} \left(C\big|_{obs}^{obs} - \mathbf{V}_{obs}^{-1}\mathbf{R} \right)^{-1} C\big|_{grd}^{obs} \right] \tag{E17}$$

This equation E17 is the same as equation 22 in the section 2.3, but multiplied by $\mathbf{V}_{grd}$.

Appendix F: Estimating Forecast Error Conversion Constant k

We want to find k to minimize the weighted difference between the diagonal ISOP variance and background variance:

$$\begin{aligned} J(k) &= w\left(k^2\mathbf{V}_{ISOP}^{ts} - \mathbf{V}_{bkg}^{ts}\right)^2 \\ &= \sum_{i=1}^{nz}\left[w_{t,i}\left(k^2V_{ISOP,i}^{t} - V_{bkg,i}^{t}\right)^2 + w_{s,i}\left(k^2V_{ISOP,i}^{s} - V_{bkg,i}^{s}\right)^2\right] \end{aligned} \tag{F1}$$

Where $V_{ISOP,i}^{t}$ and $V_{ISOP,i}^{s}$ are ISOP and $V_{b\lg,i}^{t}$ and $V_{bkg,i}^{s}$ are the variances at depth i of temperature and salinity, respectively. The value of n_z is the number of depths. The weights $w_{t,i}$ and $w_{s,i}$ are tunable weights, for temperature and salnity, described below. The derivative with respect to k^2 is then

$$\frac{\partial J(k)}{\partial\left(k^2\right)} = \sum_{i=1}^{Nd}\left[2w_{t,i}\left(k^2V_{ISOP,i}^{t} - V_{bkg}^{t}\right)V_{ISOP,i}^{t} + 2w_{s,i}\left(k^2V_{ISOP,i}^{s} - V_{bkg,i}^{s}\right)V_{ISOP,i}^{s}\right] \tag{F2}$$

Setting the derivative to zero, and solving for k^2,

$$k^2 = \frac{\sum_{i=1}^{nz}\left[w_{t,i}V_{bkg,i}^{t}V_{ISOP,i}^{t} + w_{s,i}V_{bkg,i}^{s}V_{ISOP,i}^{s}\right]}{\sum_{i=1}^{nz}\left[w_{t,i}V_{ISOP,i}^{t}V_{ISOP,i}^{t} + w_{s,i}V_{ISOP,i}^{s}V_{ISOP,i}^{s}\right]} \tag{F3}$$

If the weights are 1, this is straight forward. We could set the weights to the reciprocal of the variance of temperature and salinity at each depth. That is, $w_{t,i} = 1/V_{ISOP,i}^{t}$ and $w_{s,i} = 1/V_{ISOP,i}^{s}$. This would weight depths of low variability more. The profiles do not need to match as well at depths of high variability. It also adjusts the relative balance between temperature and salinity due to the different units. In this case,

$$k^2 = \frac{\sum_{i=1}^{nz}\left[V_{bkg,i}^{t} + V_{bkg,i}^{s}\right]}{\sum_{i=1}^{Nd}\left[V_{ISOP,i}^{t} + V_{ISOP,i}^{s}\right]} \tag{D4}$$

In this case, k^2 is the ratio of the total variance over the water column of NCODA and ISOP. Because ISOP is computed from data over the upper 1000m, and the ISOP-X data uses an extension of the deepest value downwards, this should be computed only over the upper 1000m or only over the valid water column if the water depth is less than 1000m.

Note this solves for k^2 based on variances. NCODA and ISOP have standard deviations stored. Once k^2 is computed, the standard deviations are multiplied by k as in equations (29) and (30) in the main text.

Appendix G: The Generalized 3DVAR Equation

Future upgrades may adopt a more generalized normalization shown in equation (36) in the main text. In this appendix, we start with equation (1) from the main text:

$$x_a - x_b = \mathbf{B}\mathbf{H}^T \left(\mathbf{H}\mathbf{B}\mathbf{H}^T + \mathbf{R}\right)^{-1}\left(y - \mathbf{H}x_b\right) \tag{G1}$$

Pull the $\mathbf{R}$ out by taking the square root of the diagonal observation error matrix

$$x_a - x_b = \mathbf{B}\mathbf{H}^T \left(\mathbf{H}\mathbf{B}\mathbf{H}^T + \mathbf{R}^{1/2}\mathbf{R}^{1/2}\right)^{-1}\left(y - \mathbf{H}x_b\right)$$

and then manipulate, step by step, pulling $\mathbf{R}^{1/2}$, out of the brackets

$$x_a - x_b = \mathbf{B}\mathbf{H}^T\mathbf{R}^{-1/2}\mathbf{R}^{1/2} \left(\mathbf{H}\mathbf{B}\mathbf{H}^T + \mathbf{R}^{1/2}\mathbf{R}^{1/2}\right)^{-1}\left(y - \mathbf{H}x_b\right)$$

$$x_a - x_b = \mathbf{B}\mathbf{H}^T\mathbf{R}^{-1/2} \left(\mathbf{H}\mathbf{B}\mathbf{H}^T\mathbf{R}^{-1/2} + \mathbf{R}^{1/2}\right)^{-1}\left(y - \mathbf{H}x_b\right)$$

$$x_a - x_b = \mathbf{B}\mathbf{H}^T\mathbf{R}^{-1/2} \left(\mathbf{H}\mathbf{B}\mathbf{H}^T\mathbf{R}^{-1/2} + \mathbf{R}^{1/2}\right)^{-1}\mathbf{R}^{1/2}\mathbf{R}^{-1/2}\left(y - \mathbf{H}x_b\right)$$

$$x_a - x_b = \mathbf{B}\mathbf{H}^T\mathbf{R}^{-1/2} \left(\mathbf{R}^{-1/2}\mathbf{H}\mathbf{B}\mathbf{H}^T\mathbf{R}^{-1/2} + \mathbf{I}\right)^{-1}\mathbf{R}^{-1/2}\left(y - \mathbf{H}x_b\right)$$

Using equation (31), $\widehat{\delta\mathbf{d}} = \mathbf{R}^{-1/2}\left(y - \mathbf{H}x_b\right)$, and we get

$$x_a - x_b = \mathbf{B}\mathbf{H}^T\mathbf{R}^{-1/2} \left(\mathbf{R}^{-1/2}\mathbf{H}\mathbf{B}\mathbf{H}^T\mathbf{R}^{-1/2} + \mathbf{I}\right)^{-1}\widehat{\delta\mathbf{d}} \tag{G2}$$

Expand as $\mathbf{B} = \mathbf{D}\mathbf{C}\mathbf{D}$, where $\mathbf{D} = \sqrt{diag\left(\mathbf{B}\right)}$ and $\mathbf{C}$ is the background correlation matrix to get

$$x_a - x_b = \mathbf{D}\mathbf{C}\mathbf{D}\mathbf{H}^T\mathbf{R}^{-1/2} \left(\mathbf{R}^{-1/2}\mathbf{H}\mathbf{D}\mathbf{C}\mathbf{D}\mathbf{H}^T\mathbf{R}^{-1/2} + \mathbf{I}\right)^{-1}\widehat{\delta\mathbf{d}} \tag{G3}$$

Now define $\hat{\mathbf{H}} = \mathbf{R}^{-1/2}\mathbf{H}\mathbf{D}$ and $\hat{\mathbf{H}}^T = \mathbf{D}\mathbf{H}^T\mathbf{R}^{-1/2}$ so that we get

$$x_a - x_b = \mathbf{D}\mathbf{C}\hat{\mathbf{H}}^T \left(\hat{\mathbf{H}}\mathbf{C}\hat{\mathbf{H}}^T + \mathbf{I}\right)^{-1}\widehat{\delta\mathbf{d}} \tag{G4}$$

Note that $\hat{\mathbf{H}}\hat{\mathbf{H}}^T \neq \mathbf{I}$. Multiply both sides by $\mathbf{D}^{-1}$ and define $\widehat{\delta\mathbf{x}} = \mathbf{D}^{-1}\left(x_a - x_b\right)$ to get

$$\widehat{\delta\mathbf{x}} = \mathbf{D}\mathbf{C}\hat{\mathbf{H}}^T \left(\hat{\mathbf{H}}\mathbf{C}\hat{\mathbf{H}}^T + \mathbf{I}\right)^{-1}\widehat{\delta\mathbf{d}} \tag{G5}$$

which is equation (36) in the main text.

REFERENCES

Allard, R., Rogers, E., Martin, P., Jensen, T., Chu, P., Campbell, T., . . . Gravois, U. (2014). The US Navy Coupled Ocean-Wave Prediction System. *Oceanography, 27*(3), 92-103. doi: 10.5670/oceanog.2014.71

Allard, R. A., T. A. Smith, T. G. Jensen, P. Y. Chu, E. Rogers, T. J. Campbell, U. M. Gravois, S. N. Carroll, K. Watson. (2012). Validation Test Report for theCoupled Ocean/AtmosphereMesoscale Prediction System(COAMPS) Version 5.0:Ocean/Wave Component Validation. *NRL Memorandum Report, NRL/MR/7320--12-9423*.

Balgovind, R., Dalcher, A., Ghil, M., & Kalnay, E. (1983). A STOCHASTIC-DYNAMIC MODEL FOR THE SPATIAL STRUCTURE OF FORECAST ERROR STATISTICS. *Monthly Weather Review, 111*(4), 701-722. doi: 10.1175/1520-0493(1983)111<0701:Asdmft>2.0.Co;2

Barron, C. N., Smedstad, L. F., Dastugue J. M., and Smedstad, O. M. (2007). Evaluation of ocean models using observed and simulated drifter trajectories: Impact of sea surface height on synthetic profiles for data assimilation. *Journal of Geophysical Research-Oceans, 112*(C07019). doi: doi:10.1029/2006JC002982

Barron, C. N., Kara, A. B., Martin, P. J., Rhodes, R. C., & Smedstad, L. F. (2006). Formulation, implementation and examination of vertical coordinate choices in the Global Navy Coastal Ocean Model (NCOM). *Ocean Modelling, 11*(3-4), 347-375. doi: 10.1016/j.ocemod.2005.01.004

Berta, M., Griffa, A., Magaldi, M. G., Ozgokmen, T. M., Poje, A. C., Haza, A. C., & Olascoaga, M. J. (2015). Improved Surface Velocity and Trajectory Estimates in the Gulf of Mexico from Blended Satellite Altimetry and Drifter Data. *Journal of Atmospheric and Oceanic Technology, 32*(10), 1880-1901. doi: 10.1175/jtech-d-14-00226.1

Bleck, R. (2002). An oceanic general circulation model framed in hybrid isopycnic-Cartesian coordinates. *Ocean Modelling, 4*(1), 55-88. doi: 10.1016/s1463-5003(01)00012-9

Carrier, M. J., Ngodock, H., Smith, S., Jacobs, G., Muscarella, P., Ozgokmen, T., . . . Lipphardt, B. (2014). Impact of Assimilating Ocean Velocity Observations Inferred from Lagrangian Drifter Data Using the NCOM-4DVAR. *Monthly Weather Review, 142*(4), 1509-1524. doi: 10.1175/mwr-d-13-00236.1

Carrier, M. J., Ngodock, H. E., Muscarella, P., & Smith, S. (2016). Impact of Assimilating Surface Velocity Observations on the Model Sea Surface Height Using the NCOM-4DVAR*. *Monthly Weather Review, 144*(3), 1051-1068. doi: 10.1175/mwr-d-14-00285.1

Centurioni, L. R., Turton, J., Lumpkin, R., Braasch, L., Brassington, G., Chao, Y., . . . Zhang, D. X. (2019). Global in situ Observations of Essential Climate and Ocean Variables at the Air-Sea Interface. *Frontiers in Marine Science, 6*, 23. doi: 10.3389/fmars.2019.00419

Cummings, J. A. (2005). Operational multivariate ocean data assimilation. *Quarterly Journal of the Royal Meteorological Society, 131*(613), 3583-3604. doi: 10.1256/qj.05.105

Cummings, J. A. a. S., O. M. (2013). Variational Data Assimilation for the Global Ocean. *S.K. Park and L. Xu (eds.), Data Assimilation for Atmospheric, Oceanic and Hydrologic Applications (Vol. II),, 2*. doi: 10.1007/978-3-642-35088-7 13

D'Addezio, J. M., Smith, S., Jacobs, G. A., Helber, R. W., Rowley, C., Souopgui, I., & Carrier, M. J. (2019). Quantifying wavelengths constrained by simulated SWOT observations in a submesoscale resolving ocean analysis/forecasting system. *Ocean Modelling, 135*, 40-55. doi: 10.1016/j.ocemod.2019.02.001

Daley, R. (1991). *Atmospheric Data Analysis*. New York, NY: Cambridge University Press.

Daley, R. a. E. B. (2000). NAVDAS Source Book 2000. *NRL Publication, 7530--00*(418), 157.

Elipot, S., Lumpkin, R., Perez, R. C., Lilly, J. M., Early, J. J., & Sykulski, A. M. (2016). A global surface drifter data set at hourly resolution. *Journal of Geophysical Research-Oceans, 121*(5), 2937-2966. doi: 10.1002/2016jc011716

Gates, D. C., Margolina, T., Collins, C. A., & Rago, T. A. (2018). Observation and prediction of flotsam trajectories in the California Current System based on surface drift of RAFOS floats. *Deep-Sea Research Part Ii-Topical Studies in Oceanography, 151*, 102-114. doi: 10.1016/j.dsr2.2018.04.003

Goodfellow, I., Bengio, Yochua, and Courville, Aaron. (2016). *Deep learning*. Cambridge, Massachusetts: The MIT Press.

Gray, A. R., & Riser, S. C. (2014). A Global Analysis of Sverdrup Balance Using Absolute Geostrophic Velocities from Argo. *Journal of Physical Oceanography, 44*(4), 1213-1229. doi: 10.1175/jpo-d-12-0206.1

Helber, R. W., T. L. Townsend, C. N. Barron, J. M. Dastugue, and M. R. Carnes. (2013). Validation Test Report for the Improved Synthetic Ocean Profile (ISOP) System, Part 1: Synthetic Profile Methods and Algorithm. *NRL Report NRL/MR/7320, 13-9364*.

Helber, R. W., Scott R. Smith, Gregg A. Jacobs, Charlie N. Barron, Matthew J. Carrier, Clark D. Rowley, Hans E. Ngodock, Max Yaremchuk, Ivo Pasmans, Brent P. Bartels, Chris J. DeHaan. (2022). Ocean Drifter Velocity Data Assimilation, Part 1: Formulation and Diagnostic Results. *Ocean Modelling*.

Hoteit, I., Cornuelle, B., Kim, S. Y., Forget, G., Kohl, A., & Terrill, E. (2009). Assessing 4D-VAR for dynamical mapping of coastal high-frequency radar in San Diego. *Dynamics of Atmospheres and Oceans, 48*(1-3), 175-197. doi: 10.1016/j.dynatmoce.2008.11.005

Isern-Fontanet, J., Ballabrera-Poy, J., Turiel, A., & Garcia-Ladona, E. (2017). Remote sensing of ocean surface currents: a review of what is being observed and what is being assimilated. *Nonlinear Processes in Geophysics, 24*(4), 613-643. doi: 10.5194/npg-24-613-2017

Jacobs, G., Joseph D'Addezio, Josie Fabre, Brent Bartels, Pete Spence, Lea Locke-4 Wynn. (2022). Ocean Confidence, Validation Test Report (O. S. D. Ocean Dynamics and Prediction Branch, Trans.) *Memorandum Report*. Stennis Space Center, MS: Naval Research Laboratory.

Jacobs, G., D'Addezio, J. M., Ngodock, H., & Souopgui, I. (2021a). Observation and model resolution implications to ocean prediction. *Ocean Modelling, 159*, 13. doi: 10.1016/j.ocemod.2021.101760

Jacobs, G. A., J. M. D'Addezio, B. Bartels, P. L. Spence. (2021b). Constrained scales in ocean forecasting. *Advances in Space Research, 68*, 746-761.

Jacobs, G. A., Bartels, B. P., Bogucki, D. J., Beron-Vera, F. J., Chen, S. S., Coelho, E. F., . . . Wei, M. Z. (2014a). Data assimilation considerations for improved ocean predictability during the Gulf of Mexico Grand Lagrangian Deployment (GLAD). *Ocean Modelling, 83*, 98-117. doi: 10.1016/j.ocemod.2014.09.003

Jacobs, G. A., Richman, J. G., Doyle, J. D., Spence, P. L., Bartels, B. P., Barron, C. N., . . . Bub, F. L. (2014a). Simulating conditional deterministic predictability within ocean frontogenesis. *Ocean Modelling, 78*, 1-16. doi: 10.1016/j.ocemod.2014.02.004

Kalnay, E. (2003). *Atmospheric Modeling, Data Assimilation and Predictability*. United Kingdom: Cambridge Universiy Press.

Kurapov, A. L., Allen, J. S., Egbert, G. D., Miller, R. N., Kosro, P. M., Levine, M., & Boyd, T. (2005). Distant effect of assimilation of moored currents into a model of coastal wind-driven circulation off Oregon. *Journal of Geophysical Research-Oceans, 110*(C2), 20. doi: 10.1029/2003jc002195

Liu, Y. a. R. H. W. (2011). Evaluation of trajectory modeling in different dynamic regions using normalized cumulative Lagrangian separation. *J. of Geophysical Res, 116*(C09013). doi: doi:10.1029/2010JC006837

Lumpkin, R., Ozgokmen, T., Centurioni, L., & Annual, R. (2017). Advances in the Application of Surface Drifters *Annual Review of Marine Science, Vol 9* (Vol. 9, pp. 59-81). Palo Alto: Annual Reviews.

Metzger, E. J. (2014). US Navy Operational Global Ocean and Arctic Ice Prediction Systems. *Oceanography, 27*(3), 32-43. doi: http://dx.doi.org/10.5670/oceanog.2014.66

Metzger, E. J., & Hurlburt, H. E. (2001). The nondeterministic nature of Kuroshio penetration and eddy shedding in the South China Sea. *Journal of Physical Oceanography, 31*(7), 1712-1732. doi: 10.1175/1520-0485(2001)031<1712:Tnnokp>2.0.Co;2

Molemaker, M. J., McWilliams, J. C., & Capet, X. (2010). Balanced and unbalanced routes to dissipation in an equilibrated Eady flow. *Journal of Fluid Mechanics, 654*, 35-63. doi: 10.1017/s0022112009993272

Morin, D. (2016). *Probability For the Enthusiastic Beginner*: Harvard University.

Muscarella, P., Carrier, M. J., Ngodock, H., Smith, S., Lipphardt, B. L., Kirwan, A. D., & Huntley, H. S. (2015). Do Assimilated Drifter Velocities Improve Lagrangian Predictability in an Operational Ocean Model? *Monthly Weather Review, 143*(5), 1822-1832. doi: 10.1175/mwr-d-14-00164.1

Ngodock, H., P. Muscarella, M. Carrier, I. Souopgui and S. Smith. (2015). Assimilation of HF Radar Observations in the Chesapeake-Delaware Bay Region Using the Navy Coastal Ocean Model (NCOM) and the Four-Dimensional Variational (4DVAR) Method *Coastal Ocean Observing Systems*.

Oke, P. R., Allen, J. S., Miller, R. N., Egbert, G. D., & Kosro, P. M. (2002). Assimilation of surface velocity data into a primitive equation coastal ocean model. *Journal of Geophysical Research-Oceans, 107*(C9), 25. doi: 10.1029/2000jc000511

Paduan, J. D., & Washburn, L. (2013). High-Frequency Radar Observations of Ocean Surface Currents. In C. A. Carlson & S. J. Giovannoni (Eds.), *Annual Review of Marine Science, Vol 5* (Vol. 5, pp. 115-136). Palo Alto: Annual Reviews.

Rogers, S. a. M. G. (2017). *A First Course in Machine Learning*: CRC Press, Taylor & Francis Group.

Rowley, C. a. M., Andrea. (2014). Regional and Coastal Prediction with the Relocatable Ocean Nowcast/Forecast System. *Oceanography, 27*(3), 44-55. doi: doi:10.5670/oceanog.2014.67

Rudnick, D. L. (2016). Ocean Research Enabled by Underwater Gliders. In C. A. Carlson & S. J. Giovannoni (Eds.), *Annual Review of Marine Science, Vol 8* (Vol. 8, pp. 519-+). Palo Alto: Annual Reviews.

Smith, S., .J. A. Cummings, P. Spence, S. N. Carroll, C. Rowley, O. M. Smedstad, P. Chu, B. Lunde, J. Shriver and R. Helber, 2012:. (2012). Validation Test Report for the Navy Coupled Ocean Data Assimilation 3D Variational Analysis (NCODA-VAR) System, Version 3.43. *NRL Report NRL/MR/7320, 12*(9363).

Smith, S., R.,Robert W. Helber, Gregg A. Jacobs, Charlie N. Barron, Matt Carrier, Clark Rowley, Hans Ngodock, Ivo Pasmans, Brent Bartels, Chris DeHaan, and Max Yaremchuk. (2022). Ocean Drifter Velocity Data Assimilation Part 2: Forecast Validation. *Ocean Modelling*.

Sun, L. Y., & Penny, S. G. (2019). Lagrangian Data Assimilation of Surface Drifters in a Double-Gyre Ocean Model Using the Local Ensemble Transform Kalman Filter. *Monthly Weather Review, 147*(12), 4533-4551. doi: 10.1175/mwr-d-18-0406.1

Thiebaux, H. J. (1985). ON APPROXIMATIONS TO GEOPOTENTIAL AND WIND-FIELD CORRELATION STRUCTURES. *Tellus Series a-Dynamic Meteorology and Oceanography, 37*(2), 126-131. doi: 10.1111/j.1600-0870.1985.tb00275.x

van Sebille, E., P. J. van Leeuwen, A. Biastoch, C. N. Barron, and W. P. M. de Ruijter. (2009). Lagrangian validation of numerical drifter trajectories using drifting buoys: Application to the Agulhas system. *Ocean Modelling, 29*, 269-276.

Wilkin, J. L., Arango, H. G., Haidvogel, D. B., Lichtenwalner, C. S., Glenn, S. M., & Hedstrom, K. S. (2005). A regional ocean modeling system for the Long-term Ecosystem Observatory. *Journal of Geophysical Research-Oceans, 110*(C6), 13. doi: 10.1029/2003jc002218

Wolfram. (2012). Mathematica: Wolfram Research, Inc.

Wunsch, C. (1997). The vertical partition of oceanic horizontal kinetic energy. *Journal of Physical Oceanography, 27*(8), 1770-1794. doi: 10.1175/1520-0485(1997)027<1770:Tvpooh>2.0.Co;2

Wunsch, C., Heimbach, P., Ponte, R. M., Fukumori, I., & Members, E.-G. C. (2009). THE GLOBAL GENERAL CIRCULATION OF THE OCEAN ESTIMATED BY THE ECCO-CONSORTIUM. *Oceanography, 22*(2), 88-103. doi: 10.5670/oceanog.2009.41

Yaremchuk, M. a. P. M. (2016). Implementation of a Balance Operator in NCOM. *NRL Memorandum Report, 16*(9649), 19.

Zhao, M. N., Ponte, R. M., Wang, O., & Lumpkin, R. (2021). Using Drifter Velocity Measurements to Assess and Constrain Coarse-Resolution Ocean Models. *Journal of Atmospheric and Oceanic Technology, 38*(4), 909-919. doi: 10.1175/jtech-d-20-0159.1